

**From non-contact to contact –  
high-precision atomic force microscopy  
with atomically-characterized tips**



Dissertation zur Erlangung des Doktorgrades der  
Naturwissenschaften (Dr. rer. nat.) der Fakultät für Physik  
der Universität Regensburg

vorgelegt von

Alexander Liebig

aus Eggenfelden

im Jahr 2021

Promotionsgesuch eingereicht am: 14. April 2021

Die Arbeit wurde angeleitet von: Prof. Dr. Franz J. Gießibl

Prüfungsausschuss: Vorsitzender: Prof. Dr. Klaus Richter  
Erstgutachter: Prof. Dr. Franz J. Gießibl  
Zweitgutachter: Prof. Dr. Dominique Bougeard  
weiterer Prüfer: PD Dr. Jonathan Eroms

Das Promotionskolloquium fand am 14. Juli 2021 statt.

# Contents

<b>1. Introduction</b>	<b>1</b>
<b>2. Principles of scanning tunneling and atomic force microscopy</b>	<b>5</b>
2.1. Scanning tunneling microscopy . . . . .	5
2.2. Atomic force microscopy . . . . .	7
2.2.1. Frequency modulation atomic force microscopy . . . . .	8
2.2.2. Forces detected in low-temperature atomic force microscopy . . . . .	9
2.2.3. Imaging and spectroscopy modes in simultaneous STM and AFM experiments . . . . .	12
<b>3. Experimental setup and measurement techniques</b>	<b>15</b>
3.1. Low-temperature STM/AFM setup . . . . .	15
3.2. qPlus sensor . . . . .	17
3.3. Tip preparation and characterization . . . . .	20
3.3.1. CO/Cu(111) sample preparation . . . . .	20
3.3.2. Tip preparation . . . . .	23
3.3.3. Tip characterization with the COFI method . . . . .	26
<b>4. High-precision AFM measurements on CaF<sub>2</sub>(111) with an atomically-characterized metal tip</b>	<b>29</b>
4.1. CaF <sub>2</sub> (111) surface . . . . .	31
4.1.1. Surface structure . . . . .	31
4.1.2. Decay length of the electric field outside an ionic crystal . . . . .	32
4.2. Electrostatic point charge calculation . . . . .	34
4.3. Experimental results . . . . .	37
4.3.1. Comparison to the electrostatic calculation . . . . .	39
4.3.2. Atomic resolution with femtonewton force contrast . . . . .	43
4.3.3. Improving the tip model by utilizing the COFI data . . . . .	48
4.3.4. Influence of tip polarizability and sample relaxations . . . . .	52
4.4. Discussion . . . . .	56

<b>5. Quantifying the evolution of atomic interaction of a CO-terminated tip with a complex ionic crystal surface</b>	<b>57</b>
5.1. Evolution of atomic contrast in experimental constant-height images .	59
5.2. Probe particle model simulations . . . . .	62
5.2.1. Determining Pauli repulsion via the overlap of the electron densities of tip and sample . . . . .	64
5.2.2. Probe particle model simulations using Lennard-Jones potentials to describe Pauli repulsion . . . . .	70
5.3. Electrostatic imaging regime . . . . .	72
5.4. Discussion . . . . .	76
<b>6. <i>In-situ</i> characterization of O-terminated Cu tips based on the COFI method</b>	<b>79</b>
6.1. Oxygen tip functionalization on the Cu(110)-(2×1)O surface . . . . .	80
6.2. COFI characterization of O-terminated Cu tips . . . . .	84
6.2.1. Comparison to COFI data of CO-terminated tips . . . . .	88
6.2.2. Comparison to tip fingerprinting . . . . .	90
6.3. Geometric structure of CuO <sub>x</sub> tip apices with multiple oxygen atoms .	94
6.4. Discussion . . . . .	99
<b>7. Summary and outlook</b>	<b>101</b>
<b>A. Appendix</b>	<b>107</b>
<b>List of Publications</b>	<b>123</b>
<b>Bibliography</b>	<b>125</b>
<b>Acknowledgments</b>	<b>145</b>

# 1. Introduction

Nanoscience is the study of phenomena that occur in systems with nanometer dimensions [1]. It has evolved into a well-established discipline in modern research and industry with applications from biology [2, 3] to quantum computing [4]. For example, Nanoscience has been used in medicine with nanoparticles for cancer therapy [2] or mRNA-based vaccines, currently proving crucial in the fight against a global pandemic [3]. Furthermore, basic research in Nanoscience aims at stabilizing and controlling surface spins at the single-atom level for potential data storage applications [5–8]. Importantly, at nanometer length scales quantum-mechanical and atomic-scale effects become increasingly dominant [1]. Both van der Waals and electrostatic interactions are much more significant than they are at larger length scales. A central goal in Nanoscience is therefore to establish methods and concepts to understand and guide interaction at this length scale, which requires understanding the forces that are at play. The most natural probe for this is the atomic force microscope (AFM) [9], specifically when operated in the frequency modulation atomic force microscopy (FM-AFM) mode [10], which allows for imaging surfaces with atomic resolution, detection of nanoscale interactions and even manipulation of surfaces at the atomic-scale [11].

In the first reports about atomic resolution in FM-AFM experiments [12, 13], attractive tip-sample forces on the order of 1 nN were observed in the so-called non-contact regime. These strong tip-sample forces were necessary for atomic resolution imaging. However, nanonewton forces can lead to lateral and vertical relaxations in both tip and sample [14–23], as they have been recognized already in previous scanning tunneling microscopy (STM) experiments [24]. For illustration, atomic bonds in solids with electronvolt bond energies [25] have bond stiffnesses on the order of 100 N/m. Hence, a force of 1 nN stretches the bonds of surface atoms by distances on the order of 10 pm. In this context, true non-perturbative imaging requires very weak tip-sample interaction. This means we will not only be leaving the atomic positions undisturbed, but have the possibility to investigate single spin systems [26, 27] and sensitive electronic ground states [28] without perturbing them. The precise measurement of weak tip-sample interactions poses the challenge of acquiring data with less

signal, or in other words piconewton and sub-piconewton force contrasts in a deep non-contact regime. But any microscope is only as good as its objective lens and in the case of the AFM, the equivalent to the lens are sensor and tip apex [29].

A key requirement for the high-precision measurement of sub-piconewton force contrasts is therefore the ability to control the AFM tip apex at the atomic scale. Ultimately, this means being able to experimentally characterize the AFM tip apex with atomic resolution and to maintain this tip condition during the measurement. Over the last decade, much effort has been put into the development of techniques to atomically-characterize the AFM tip apex such as the carbon monoxide front atom identification (COFI) method [30–32]. In COFI, a single carbon monoxide (CO) molecule adsorbed on a copper surface can be probed to image the chemical and structural composition of an AFM tip apex with atomic resolution. Moreover, CO has also been shown to be an excellent tip apex. This was demonstrated by Gross *et al.* who used it to resolve the internal structure of a flat organic molecule [33]. The drastic increase in resolution was enabled by functionalizing a metal tip apex with a CO molecule. This tip functionalization effectively passivates the tip apex, i.e. it reduces its chemical reactivity, which allows for stably approaching the tip from the non-contact regime to the contact regime, where repulsive forces start to dominate the overall tip-sample interaction [33, 34]. Although the spatial resolution in an AFM experiment can be enhanced by CO tip functionalization, the small lateral stiffness of the tip apex frequently hinders a quantitative interpretation of data [18]. Lateral forces can cause a lateral deflection of the CO molecule, which can yield artifacts in the images such as an elongated appearance of intramolecular features [18]. Moreover, previous studies regarding the electrostatic interaction have reported apparently conflicting results, indicating that the electrostatic interaction with an atomic lattice is mediated in some cases via the CO molecule [35], as opposed to the background metal tip in other cases [36].

In this thesis, high-precision AFM measurements with atomically-characterized metal and two types of functionalized tips, namely CO-terminated and O-terminated metal tips, are presented. The atomic interaction mechanisms that are relevant for the AFM contrast in the measurements with each tip apex termination are analyzed in detail as a function of tip-sample distance. While a metal tip allows for data acquisition solely in the non-contact regime where force contrasts as low as 350 fN are observed, tip functionalization enables the conduction of experiments also in the contact regime.

The remaining chapters of this work are outlined as follows. In chapter 2, the

---

fundamental principles underlying STM and AFM are presented. Specifically, the FM-AFM mode of operation [10], which is used throughout this work, is described in detail. Additionally, the imaging and spectroscopy modes that have been used in the simultaneous STM and AFM experiments discussed within this thesis are presented.

Chapter 3 introduces the experimental setup and measurement techniques used in this work. First, the microscope setup that was used to conduct the measurements presented within this thesis is described. Second, the qPlus sensor [37], which allows simultaneous STM and AFM measurements, is presented. Afterwards, the techniques for tip preparation and characterization with the COFI method are described in detail.

In chapter 4, high-precision AFM measurements on the  $\text{CaF}_2(111)$  surface with an atomically-characterized metal tip are discussed. At first, the distance dependence of the electric field outside an ionic crystal is derived and a model to calculate the AFM contrast based on the electrostatic interaction between point charges is developed. This is followed by a comparison between the calculation and experimental data recorded with the single-atom metal tip, which indicates that the AFM contrast is entirely described by the electrostatic tip-sample interaction. Afterwards, the implication of measurement noise on experimental AFM data with femtonewton force contrasts is analyzed. At last, the theoretical description of the tip apex is refined based on the experimental COFI characterization of second layer tip atoms.

Chapter 5 presents a quantitative analysis of the atomic interaction of a CO-terminated tip with the  $\text{CaF}_2(111)$  surface as a function of tip-sample distance. The experimental AFM images show strong variations with distance. Thus, to understand the rich contrast features they are compared to a mechanical model, which is used to simulate AFM images with CO-functionalized tips. The images are reproduced by the model at all tip-sample distances, which enables the decomposition of the dominant physical mechanisms in the interaction of the CO-terminated tip with the  $\text{CaF}_2(111)$  surface. It is found that the electrostatic contribution originates in the force acting on the CO molecule at the tip apex, which is in agreement to the findings in Ref. [35]. Finally, this electrostatic interaction is analyzed in more detail by comparing the experimental data to the electrostatic calculation introduced in chapter 4, modified for the CO-terminated tip.

Chapter 6 discusses the experimental characterization of oxygen-terminated copper (CuOx) tips at the atomic scale. As mentioned above, the low lateral stiffness of a CO-terminated tip apex often complicates a quantitative analysis of the experimental data. Recently, Mönig *et al.* have shown that CuOx tips show comparable spatial resolution capabilities to CO-terminated tips, but have a much higher lateral tip apex stiffness [38]. Similar to CO-terminated tips CuOx are chemically inert,

which enables experiments in the contact regime. In existing literature, a successful tip functionalization with oxygen is indirectly characterized by theoretical and experimental analysis of STM and AFM images of oxidized copper surfaces serving as a tip fingerprint. In chapter 6, the COFI method is established as way to atomically-characterize the apex of CuOx tips *in-situ*. First, the preparation of a CuOx tip apex is explained and COFI and force spectroscopy data of CuOx tips are presented. Then, the data recorded with CuOx tips is compared to data recorded with CO-terminated tips indicating quantitatively comparable interaction mechanisms for both tip terminations. Afterwards, tip fingerprinting experiments are conducted with different CuOx tips on a partially oxidized Cu(110) surface for comparison to existing literature. At last, the geometric structure of a CuOx tip with two oxygen atoms at the tip apex is characterized based on the COFI method.

Finally, chapter 7 concludes with a summary of all the results presented within this thesis.

# 2. Principles of scanning tunneling and atomic force microscopy

All experiments in this thesis were performed with a combined scanning tunneling and atomic force microscope that utilizes the qPlus sensor for simultaneous STM and AFM measurements [37]. This chapter contains a description of the fundamental principles of STM (section 2.1) and AFM (section 2.2).

## 2.1. Scanning tunneling microscopy

The scanning tunneling microscope (STM)<sup>1</sup> was presented by Binnig *et al.* [39] in 1982 and paved the way for experiments with atomic resolution on conducting surfaces. One of the first major achievements of STM was the real-space imaging of the adatoms of the Si(111)- $7 \times 7$  reconstruction, which had been an unresolved issue in surface science until then [40]. A detailed description of both the physical aspects and the technical details of STM can be found in the book of Chen [41]. This section summarizes the main concepts relevant in context of the present work based on Ref. [41]. In essence, an STM consists of a sharp metal tip that is positioned with picometer precision above a conductive sample surface using a piezoelectric tube, which can move the tip laterally in the  $xy$  plane and vertically ( $z$  direction). If the tip-sample distance is reduced to several angstroms ( $1 \text{ \AA} = 100 \times 10^{-12} \text{ m} = 100 \text{ pm}$ ) and a bias voltage  $V_b$  is applied between tip and sample, a current can be detected although there is no physical contact between the two electrodes [41]. This current originates from the quantum mechanical tunneling of electrons through the vacuum gap between tip and sample [42], which can be described by a simple one-dimensional model. The vacuum gap is represented by a rectangular potential barrier of width  $z$ , where  $z$  is defined as the tip-sample distance [41]. The effective barrier height is given as  $\Phi = (\Phi_t + \Phi_s)/2$ , where  $\Phi_t$  and  $\Phi_s$  are the work functions of tip and sample, respectively [42]. Solving the Schrödinger equation for this model and assuming

---

<sup>1</sup>Throughout this work, STM is used as an abbreviation for both the technique scanning tunneling microscopy as well as the instrument scanning tunneling microscope.

$eV_b \ll \Phi$ , the tunneling current is obtained as

$$I(z) = I(0) \exp(-2\kappa z), \quad (2.1)$$

where  $\kappa = \sqrt{2m_e\Phi/\hbar^2}$ ,  $m_e$  is the free electron mass and  $\hbar$  is the reduced Planck's constant [41]. This exponential distance dependence is the reason for the high spatial resolution achieved with an STM. Typical metal work functions are on the order of  $\Phi \approx 5.0 \text{ eV}$ , resulting in a decay constant of  $\kappa \approx 11 \text{ nm}^{-1}$  [41, 43]. Hence, if the tip-sample distance is decreased by  $1 \text{ \AA}$ , the tunneling current increases by approximately one order of magnitude.

To additionally take into account influences of the applied bias voltage and the electronic states in tip and sample, the tunneling current can be expressed in the *Bardeen theory* [44] as an integral over all energies  $\epsilon$ ,

$$I(V_b) = \frac{4\pi e}{\hbar} \int_{-\infty}^{+\infty} \rho_S(E_F - eV_b + \epsilon) \rho_T(E_F + \epsilon) [f(E_F - eV_b + \epsilon) - f(E_F + \epsilon)] |M|^2 d\epsilon, \quad (2.2)$$

where  $f(E) = [1 + \exp((E - E_F)/k_B T)]^{-1}$  is the Fermi-Dirac distribution function,  $\rho_T$  and  $\rho_S$  are the local densities of states (LDOS) in tip and sample and  $E_F$  is the Fermi energy [41]. The tunneling matrix element  $|M|^2$  is a measure of the overlap of the electron wavefunctions in tip and sample and therefore determines the tunneling probability between the two electrodes [41]. In the limit of low temperatures  $f(E)$  takes the form of a step function and equation (2.2) translates into [41, 44]

$$I(V_b) = \frac{4\pi e}{\hbar} \int_0^{eV_b} \rho_S(E_F - eV_b + \epsilon) \rho_T(E_F + \epsilon) |M|^2 d\epsilon. \quad (2.3)$$

Equation (2.3) illustrates the difficulty in interpreting STM images, as the tunneling current depends on the LDOS of both tip and sample. Assuming that  $|M|^2$  is constant [44] and that the tip is represented by *s*-type wave functions, which is a reasonable assumption when considering metal tips [41] meaning  $\rho_T$  is constant around  $E_F$ , it follows that the tunneling current depends only on  $\rho_S(E_F - eV_b)$  [41, 45, 46]. This means that the STM probes the LDOS of the sample at the Fermi level rather than the surface topography when using metal tips [41, 47].

Due to its monotonic distance dependence the tunneling current  $I(z)$  can be reliably used as a feedback parameter. When the STM is operated in the *constant-current mode*, the tip-sample distance  $z$  is regulated in order to maintain a constant tunneling current setpoint  $I(z) = I_{\text{set}}$  for a given bias voltage  $V_b$ . In this mode the  $z$  position of the tip is monitored as a function of the lateral tip position above the sample, which

results in a  $z(x, y)$  map. These STM feedback images are often referred to as *STM topography images*, although the STM is sensitive to the sample's LDOS rather than its topography as discussed above. If the feedback loop is switched off, the tip's  $z$  position remains constant, which is therefore referred to as *constant-height mode*. In this mode, the tunneling current is mapped as a function of the lateral tip position above the sample,  $I(x, y)$ . However, if the microscope is mechanically unstable and the sample surface is highly corrugated, this mode poses the danger of unwanted tip-sample collisions during the experiment [41].

## 2.2. Atomic force microscopy

The limitation of the STM is that only conducting materials can be investigated. When the tip is brought close to the surface, atomic forces that act between tip and sample have been observed in STM experiments [41, 48]. The atomic force microscope (AFM)<sup>2</sup> introduced by Binnig *et al.* in 1986 [9] is able to scan also non-conducting materials with high resolution by measuring forces that act between tip and sample. AFM is not restricted to only conducting samples and can be operated in a plethora of environments, ranging from low-temperature and ultra-high vacuum to ambient and liquid environments. Hence, the technique is more versatile than STM and is well-established in surface science and technology. AFM is well-described in various review papers and books [49–54] and the following section briefly introduces the main concepts behind the technique mainly based on the explanations in Ref. [50].

In AFM, the tip itself is mounted on a cantilever with spring constant  $k$ . In the *static mode* of operation the tip-sample forces  $F_{ts}$  are directly proportional to the cantilever deflection  $d$  according to Hooke's law,  $F_{ts} = kd$  [50]. This mode requires soft cantilevers with relatively small  $k$  values (typically  $k < 10$  N/m [50]) to assure that the sample is not damaged during scanning. Throughout this thesis the microscope is operated in the *dynamic mode*, in which the tip is oscillated with an amplitude  $A$  above the surface [50]. The two main dynamic operation modes are amplitude modulation AFM (AM-AFM) [55] and frequency modulation AFM (FM-AFM) [10]. In AM-AFM the sensor is excited with a constant drive amplitude at a fixed frequency close to the cantilever's unperturbed resonance frequency  $f_0$  [50]. Tip-sample interactions result in a deviation of both the amplitude and phase of the cantilever motion that can be used as feedback parameters [50]. The time scales on which the amplitude change responds to the tip-sample force is  $\tau \approx 2Q/f_0$  [10, 56].  $Q = 2\pi E/E_{\text{loss}}$

---

<sup>2</sup>Throughout this work, AFM is used as an abbreviation for both the technique atomic force microscopy as well as the instrument atomic force microscope.

is the quality factor of the force sensor, where  $E = \frac{1}{2}kA^2$  is the energy stored in the oscillator and  $E_{\text{loss}}$  is the energy loss per oscillation cycle [50]. Due to the operation at cryogenic temperatures the force sensors used in this work showed  $Q$  factors up to 900 000 at resonance frequencies on the order of  $f_0 = 50$  kHz, which results in  $\tau = 36$  s. Consequently, the AM-AFM mode is impractical for low-temperature experiments. Furthermore, the observables in FM-AFM, the change in resonance frequency due to conservative tip-sample forces and the energy dissipation due to non-conservative forces, are more directly related to the physical interaction than amplitude and phase in AM-AFM experiments [50, 57]. Hence, in this work the FM-AFM mode is used, which will be described in detail in the following section.

### 2.2.1. Frequency modulation atomic force microscopy

In FM-AFM the cantilever is excited to oscillate at a constant amplitude  $A$  above the surface [10], which can be described by a weakly perturbed harmonic oscillator with an unperturbed resonance frequency

$$f_0 = \frac{1}{2\pi} \sqrt{\frac{k}{m^*}}, \quad (2.4)$$

where  $k$  is the stiffness and  $m^*$  is the effective mass of the cantilever [50]. If a force  $F_{\text{ts}}$  acts on a tip mounted on the cantilever, the resulting motion can be described considering an effective spring constant  $k' = k + k_{\text{ts}}$ . Here,  $k_{\text{ts}} = -\partial F_{\text{ts}}/\partial z$  is the tip-sample force gradient, assumed to be uniform along the cantilevers trajectory. The shift of the resonance frequency, also called *frequency shift*,  $\Delta f = f - f_0$  can then be calculated as [50]

$$\Delta f(z) = \frac{f_0}{2k} k_{\text{ts}}(z), \quad (2.5)$$

where  $z$  is the tip-sample separation. Equation (2.5) shows that the frequency shift is a measure of the tip-sample force gradient  $k_{\text{ts}}(z)$  rather than directly of the tip-sample force. This *gradient approximation* is only valid if  $k_{\text{ts}}(z)$  is constant over the tip-sample distances covered by one oscillation cycle [58]. In real experiments this condition is usually not fulfilled and the cantilever oscillation has to be considered. The frequency shift  $\Delta f$  was derived by Giessibl as [58, 59]

$$\Delta f(z) = \frac{f_0}{2k} \frac{2}{\pi A^2} \int_{-A}^A F_{\text{ts}}(z - q') \frac{q'}{\sqrt{A^2 - q'^2}} dq', \quad (2.6)$$

where  $z$  is the vertical base position of the cantilever and  $q' = A \cos(2\pi f_0 t)$  is the cantilever oscillation. Integrating equation (2.6) by parts results in [58]

$$\Delta f(z) = \frac{f_0}{2k} \frac{2}{\pi A^2} \int_{-A}^A k_{\text{ts}}(z - q') \sqrt{A^2 - q'^2} dq'. \quad (2.7)$$

Consequently, the frequency shift is proportional to the convolution of the tip-sample force gradient  $k_{\text{ts}}$  and a semi-circular weight function  $w(q') = 2/(\pi A^2)\sqrt{A^2 - q'^2}$  of radius  $A$  and integral 1 [58]. Hence, equation (2.5) has to be modified with a weighted force gradient  $\langle k_{\text{ts}}(z) \rangle$  [58]:

$$\Delta f(z) = \frac{f_0}{2k} \langle k_{\text{ts}}(z) \rangle. \quad (2.8)$$

As the frequency shift  $\Delta f(z)$  depends on the tip-sample distance, it can be used as a feedback parameter to adjust the tip-sample distance by keeping a constant frequency shift setpoint  $\Delta f(z) = \Delta f_{\text{set}}$ , analogous to the constant-current mode in STM. This *AFM feedback mode* is more difficult to establish than the STM feedback, as the tip-sample interaction and therefore  $\Delta f(z)$  is not monotonic [50]. Hence, the AFM feedback should be activated only in a tip-sample distance regime where  $\Delta f(z)$  is monotonic, typically only on the attractive branch of the tip-sample interaction potential at larger separations. If the AFM is operated in the *constant-height mode*, no artifacts of a varying tip-sample distance are present, which allows for a direct analysis of the recorded  $\Delta f(x, y)$  maps. The constant-height  $\Delta f$  images are a measure of the tip-sample interaction, as more attractive features generally appear darker than less attractive features [50]. Throughout this work the AFM images have been solely recorded in constant-height mode.

### 2.2.2. Forces detected in low-temperature atomic force microscopy

The frequency shift is determined by the total tip-sample force. The total interaction is composed of *long-range forces* that do not vary on the atomic scale and *short-range forces* from which atomic resolution originates. This section introduces the main tip-sample interactions that are typically observed in AFM experiments in ultra-high vacuum environments, such as they are probed in the experiments presented in this work.

The main long-range force contribution is the van der Waals (vdW) interaction, which originates in correlated fluctuations of atomic dipole moments [50, 60]. The vdW interaction between two isolated atoms at a distance  $z$  is given by

$$V_{\text{vdW}}(z) = -\frac{C_{\text{vdW}}}{z^6}, \quad (2.9)$$

with the London-van der Waals constant  $C_{\text{vdW}}$  that depends on the chemical species of the two interaction partners [60–62]. While the vdW interaction according to eq. (2.9) is in principle of short-range nature, the macroscopic shape of both tip and sample needs to be considered. In the Hamaker approximation, the total vdW interaction is obtained by a pairwise summation over all atomic pairs [63]. Hence, the exact shape of tip and sample determines the shape of the total vdW potential [50]. For example, for a spherical tip with radius  $R$  and a flat sample the total vdW interaction is described by

$$F_{\text{vdW}}(z) = -\frac{\partial V_{\text{vdW}}}{\partial z} = -\frac{A_{\text{H}}R}{z^2}, \quad (2.10)$$

where  $A_{\text{H}}$  is the Hamaker constant that depends on the materials of tip and sample [50, 59, 63]. Consequently, eq. (2.10) describes a long-range attractive tip-sample interaction, which can be significantly reduced if  $R$  is decreased, i.e. if the macroscopic tip shape is sharpened. In this context, section 3.3.2 introduces a method to modify the tip apex shape by repeatedly poking the tip into a clean Cu(111) surface.

A second long-range force contribution is of an electrostatic nature [50]. If tip and sample are electrically connected, they form a capacitance  $C(z)$  with a contact potential difference (CPD)  $V_{\text{CPD}} = (\Phi_{\text{s}} - \Phi_{\text{t}})/e$  defined by the work functions  $\Phi_{\text{t}}$  and  $\Phi_{\text{s}}$  of tip and sample, respectively [64]. If a bias voltage  $V_{\text{b}}$  is applied between tip and sample, the electrostatic tip-sample potential is determined by [65]

$$V_{\text{es}}(z) = \frac{1}{2}C(z)(V_{\text{b}} - V_{\text{CPD}})^2. \quad (2.11)$$

Accordingly, the electrostatic tip-sample force is [65]

$$F_{\text{es}}(z) = -\frac{\partial V_{\text{es}}}{\partial z} = -\frac{1}{2}\frac{\partial C(z)}{\partial z}(V_{\text{b}} - V_{\text{CPD}})^2. \quad (2.12)$$

From eq. (2.12) it follows that the long-range electrostatic tip-sample interaction depends quadratically on the applied bias voltage and is minimized if  $V_{\text{b}} = V_{\text{CPD}}$  [65, 66]. It is important to note that the CPD is defined only for conductive samples, but also on insulators the frequency shift depends quadratically on  $V_{\text{b}}$  [66]. In this case the second conductor is the conductive sample holder and the capacitor is viewed as filled with a dielectric medium, namely the insulating sample [67].

In contrast to long-range forces, short-range tip-sample interactions are responsible for atomic resolution in AFM. The short-range tip-sample interaction can be understood in terms of the interaction of an adsorbate with a surface. When the sample is approached with a chemically-inert tip such as a CO-terminated metal tip [33], the tip initially interacts with the surface atoms via vdW attraction according to

eq. (2.9). If the tip-sample distance is further reduced, Pauli repulsion between the tip and sample needs to be considered [34]. From the Pauli exclusion principle it is known that two electrons cannot be in the same quantum mechanical state [68]. As a consequence, when two chemically-inert atoms approach each other and their wave functions overlap, this leads to a repulsive force that opposes the vdW attraction. Although Pauli repulsion decays exponentially with distance  $z$ , it is frequently modeled by an empirical  $\propto z^{-12}$  term, which results in the Lennard-Jones potential that describes the interplay of Pauli repulsion and van der Waals attraction [69],

$$V_{\text{LJ}}(z) = V_0 \left[ \left( \frac{\sigma}{z} \right)^{12} - 2 \left( \frac{\sigma}{z} \right)^6 \right]. \quad (2.13)$$

Here,  $V_0$  is the bond energy and  $\sigma$  is the equilibrium distance with typical values on the order of  $V_0 \approx 10 \text{ meV}$  and  $\sigma \approx 350 \text{ pm}$  [21, 70]. A weak physical bond of an adsorbate to a surface with bond energies below 10 meV that is described by this Lennard-Jones type interaction is referred to as *physisorption* [71]. If the tip apex is not chemically inert but reactive, the tip apex atom can form a strong covalent bond with the sample atoms due to a hybridization of electronic orbitals of the tip and sample atoms [50]. If an adsorbate forms a chemical bond to a surface, this is defined as *chemisorption* [71]. In chemisorption, bond energies are typically in the eV regime and the equilibrium adsorbate-surface distance is typically less than 200 pm [70]. Recently, it has been found that in certain cases (e.g. Fe adatoms on a copper surface probed with a CO-terminated tip) the tip-sample interaction can undergo a transition from a physisorbed to a chemisorbed interaction state upon reduction of the tip-sample separation [25].

Sub-molecular resolution in experiments with CO-terminated tips is generally attributed to Pauli repulsion [34, 72] and it has been shown that the interaction of the tip-terminating O atom with flat organic molecules can be described in good approximation by Lennard-Jones potentials [22, 73]. Similarly, Pauli repulsion can result in atomic resolution on ionic samples like NaCl [35], but in addition atomic resolution of ionic surfaces can also be achieved due to the electrostatic interaction between a charged tip apex and the surface ions [74]. The opposite charges of the cations and anions building up the crystal result in either an attraction (charges of the tip apex and the respective sample atom have opposite polarities) or a repulsion (equal polarities). As it will be derived in section 4.1.2, the crystal periodicity leads to an exponential decay of the total electric field of the ionic crystal with distance. The decay length  $\lambda$  of the electric field is determined by the crystal lattice as  $\lambda = 1/|\mathbf{a}^*|$ , where  $\mathbf{a}^*$  is the reciprocal primitive vector of the ionic crystal lattice [74]. In case

of a  $\text{CaF}_2(111)$  surface, this results in  $\lambda = 53.2$  pm. The short-range electrostatic tip-sample interaction can be described in good approximation by the force acting on a point charge representing the tip apex in the electric field of the sample (see chapter 4). As shown in Ref. [35], the different short-range contributions dominate the tip-sample interaction at different tip-sample distances. In chapter 5, the relative contributions of vdW attraction, Pauli repulsion and short-range electrostatics to the interaction of a CO-terminated tip with a  $\text{CaF}_2(111)$  surface will be quantitatively analyzed as a function of tip-sample distance.

According to eq. (2.7) and (2.8) the measured frequency shift is proportional to the weighted tip-sample force gradient. Because the weight function  $w(q')$  depends on the cantilever amplitude  $A$ , it becomes obvious that a proper choice of  $A$  determines the sensitivity for long-range and short-range tip-sample interactions [50]. Assuming an exponential distance dependence of the tip-sample interaction with a decay length  $\lambda$ , it has been shown that the signal-to-noise ratio in an AFM experiment is maximized if  $A \approx 1.55 \lambda$  [75, 76]. The short-range force contributions show typical decay lengths between 20 pm and 60 pm [54], which would result in optimal oscillation amplitudes between 31 pm and 93 pm. Hence, an amplitude of  $A = 50$  pm, as it is used throughout this work, is a reasonable choice.

### 2.2.3. Imaging and spectroscopy modes in simultaneous STM and AFM experiments

The experiments presented in this work have been performed with a qPlus sensor [54], which allows simultaneous STM and (FM-)AFM measurements. Hence, the tip oscillates with a constant amplitude  $A$  around its equilibrium position leads to a modulation of the distance-dependent tunneling current. As the bandwidth of the STM preamplifier ( $B_{\text{STM}} = 1.1$  kHz) is much smaller than the sensor oscillation frequency (typically  $f_0 \geq 45$  kHz), the recorded tunneling current signal is a time average over the tip oscillation [50]. Therefore, all tunneling current values presented in this work have to be considered as an average tunneling current  $\langle I \rangle$ . The microscope can be operated either in STM- or AFM-feedback modes or in the constant-height mode. Furthermore, various other imaging and spectroscopy techniques have been employed within this thesis, as briefly described in this section.

#### Tip-sample distance spectroscopy

Tip-sample distance spectroscopy can be used to determine the tip-sample force at a given  $(x, y)$  position by recording the frequency shift as a function of tip-sample

distance  $\Delta f(z)$ . Additionally, if the tunneling current signal  $\langle I(z) \rangle$  is recorded simultaneously, the tip-sample distance can be estimated via the conductance relative to point contact (see e.g. [77]). However, as most experiments presented within this thesis have been performed on the insulating  $\text{CaF}_2(111)$  surface where no tunneling current can be recorded, this is not relevant in context of this work.

In order to quantitatively determine the tip-sample force  $F_{\text{ts}}(z)$ , eq. (2.6) must be inverted [78]. The two most established methods for this purpose are the so-called Sader-Jarvis force deconvolution [78] and the so-called Matrix method developed by Giessibl [58]. In this work, the Sader-Jarvis force deconvolution method [78], implemented as a MATLAB<sup>3</sup> routine (see Ref. [79]), is used to calculate the tip-sample force  $F_{\text{ts}}$  from experimental  $\Delta f$  data. Importantly, it has been shown by Sader *et al.* that the force deconvolution based on eq. (2.6) can be an *ill-posed* problem for certain amplitudes  $A$  and distance dependencies of the force laws, producing nonphysical  $F_{\text{ts}}$  values. While the deconvolution of an exponentially decaying force does not suffer from the ill-posedness, the determination of force curves with an inflection point, like for example the force originating from a Lennard-Jones-type interaction potential, can be ill-posed [80]. In order to determine a proper amplitude so that the force deconvolution is well-posed Sader *et al.* presented an inflection point test, which has to be applied to an experimental force curve  $F_{\text{ts}}(z)$  potentially recorded with an amplitude in the ill-posed range [80, 81]. If the force deconvolution is indeed ill-posed, the amplitude needs to be adjusted properly and the experiment needs to be repeated. All experimentally-determined tip-sample force data shown in this work have been explicitly checked for well-posed behavior in the displayed  $z$  ranges.

Furthermore, tip-sample distance spectroscopy can be used to determine relative height differences of surface atoms from the recorded  $\Delta f(z)$  curves with the so-called  $z^*$  method presented by Schuler *et al.* [82]. With a chemically-inert tip it can be assumed that the  $z$ -dependence of the interaction does not change between measurements on different surface features. Accordingly, a change of the relative height of the surface atoms directly results in an equal vertical shift of the  $\Delta f(z)$  curve, which can be quantified by extracting the heights  $z^*$  of the minima in the  $\Delta f(z)$  curves [82]. This method will be employed in chapter 6 to determine height differences not of surface atoms but of tip apex atoms of O-terminated Cu tips.

### Kelvin probe force spectroscopy

As described by eq. (2.12), the long-range electrostatic tip-sample interaction depends quadratically on the applied bias voltage  $V_b$ . Hence, also the frequency shift depends

<sup>3</sup>The MathWorks Inc., *MATLAB R2019a*, Natick, Massachusetts, United States of America (2019).

quadratically on  $V_b$ ,

$$\Delta f(V_b) \propto \frac{1}{2} \frac{\partial^2 C}{\partial z^2} (V_b - V_{\text{CPD}})^2. \quad (2.14)$$

This dependency can be used in Kelvin probe force spectroscopy to determine the contact potential difference  $V_{\text{CPD}}$  by recording the frequency shift as a function of the applied bias voltage  $\Delta f(V_b)$ . This results in a so-called Kelvin parabola with the apex located at  $V_{\text{CPD}}$  [66]. By setting the imaging voltage to  $V_b = V_{\text{CPD}}$  the long-range electrostatic tip-sample interaction, that can add a significant background attraction especially on bulk insulators, can be effectively minimized.

### Three-dimensional imaging

Three-dimensional imaging is a powerful method to quantify the distance-dependent interaction between an AFM tip and a sample surface or an isolated adsorbate. By recording a three-dimensional  $\Delta f(x, y, z)$  data set built up as a series of subsequently-recorded  $z$ -dependent constant-height  $\Delta f$  images, the three-dimensional force field of the tip-sample interaction can be precisely determined. Depending on the dimensions of the data set and the scan speed, which can be as low as  $v = 200$  pm/s, the acquisition time of a three-dimensional data set can easily exceed two days. Consequently, an experiment with these measurement parameters can be only performed in ultra-high vacuum and at cryogenic temperatures. Even in such a controlled environment thermal drift and piezo nonlinearities can drastically affect the measurement of the  $\Delta f(x, y, z)$  data set as described in Ref. [53]. Hence, in order to obtain a three-dimensional data set that can be quantitatively evaluated an active drift compensation mechanism needs to be implemented. In this work, all three-dimensional data sets have been recorded with a routine developed by Licha and Welker [83, 84]. After a user-set time (typically after three subsequent constant-height  $\Delta f$  images) the acquisition of the  $\Delta f(x, y, z)$  data set is paused and a feedback image is recorded to update the drift compensation values in all three directions. This is done by comparing the newly acquired feedback image to the preceding feedback image using cross-correlation (for details see [83]).

If the three-dimensional data set has been recorded above an isolated adsorbate, the short-range interaction component can be extracted by subtracting the  $z$ -dependent long-range component measured on the bare substrate from the  $\Delta f(x, y, z)$  data set. This “on - off” subtraction method [16, 17] is only valid if no atomic contrast is measured off the adsorbate. The three-dimensional vertical force field can then be calculated analogously to the tip-sample distance spectroscopy experiments using the methods presented e.g. in Ref. [58, 78].

# 3. Experimental setup and measurement techniques

*The described experimental setup and measurement techniques have been used during the author's Master thesis project [85]. Hence, there are similarities in the description of the setup and the employed techniques.*

This chapter will highlight the experimental setup used for the measurements in this work. The experiments have been performed with a commercial microscope setup, which will be described briefly in section 3.1. The microscope is equipped with a qPlus sensor, which allows simultaneous STM and AFM measurements. Section 3.2 introduces the qPlus sensor's main properties and its advantages for high-precision AFM experiments. The methods used for tip preparation and characterization will be explained in section 3.3.

## 3.1. Low-temperature STM/AFM setup

All experiments presented in this thesis have been performed with a commercial Omicron low-temperature (LT) microscope,<sup>1</sup> which allows simultaneous STM and AFM measurements at cryogenic temperatures in ultra-high vacuum (UHV) conditions. The microscope is controlled by a Nanonis scanning probe microscopy (SPM) acquisition electronics.<sup>2</sup> A detailed description of the system has been presented by Welker [84] and Hofmann [86] and this section summarizes the most important aspects that are relevant for the present work.

The microscope is divided into two UHV chambers, separated by a gate valve, and an airlock with another gate valve to transfer samples and sensors to the UHV system. After transfer of new sensors into the preparation chamber, the tips can be cleaned by electron-beam heating, field emission and field evaporation with the installed field-ion microscope [87]. All sensors that are newly introduced to the microscope are

---

<sup>1</sup>LT STM with qPlus option, Scienta Omicron GmbH, 65232 Taunusstein, Germany

<sup>2</sup>Nanonis BP4, Specs Zurich GmbH, Zurich, Switzerland

### 3 Experimental setup and measurement techniques

---

cleaned by field evaporation prior to the experiments. A high voltage of about 15 kV is applied to the tip, which leads to a high electric field at the tip apex that ionizes and removes these tip apex atoms. In this way adsorbates and oxide layers can be effectively cleaned off the tip apex, which leads to clean metal tips that are suitable for STM experiments [84]. The samples can be annealed on the manipulator with a built-in boron-nitride heater. Additionally, the preparation chamber contains a customized gas line system consisting of two separate lines that are each connected to the chamber via separate leak valves. The first line is used to dose argon (Ar) gas into the preparation chamber for Ar-ion sputtering of the samples. The second line can support up to four different gas bottles and is used to dose e.g. carbon-monoxide (CO) or oxygen (O<sub>2</sub>) gas into the UHV system. UHV conditions with base pressures in the 10<sup>-10</sup> mbar regime are achieved by an ion getter pump, a titan sublimation pump and a turbomolecular pump to pump off gas after leakage via the gas lines.

The analysis chamber contains a cryostat and the microscope head, which is thermally connected to the cryostat. The cryostat consists of two concentric tanks, the inner one filled with liquid helium, which enables microscope operation at a temperature of 4.4 K. The outer vessel is filled with liquid nitrogen to reduce the helium evaporation rate, which results in a cryostat hold time of about 2.5 days. UHV conditions in the analysis chamber are maintained at base pressures in the 10<sup>-11</sup> mbar regime with an ion getter pump. By operating the microscope in LT and UHV conditions, a sample can be studied for days or weeks at the same spot on the surface with atomic precision. UHV conditions minimize the adsorption of residual gas atoms and molecules and therefore, freshly prepared sample surfaces are kept clean for several days or weeks. Furthermore, LT operation minimizes the thermal drift and suppresses thermal desorption and diffusion of adsorbates, which is necessary for the study of certain surfaces [88] and adsorbates like single CO molecules [89]. To protect the microscope against mechanical vibrations the head is decoupled by three suspension springs and additionally protected by an eddy current damping stage. Additionally, the chamber contains two room-temperature carousels that provide storage space for up to twelve sensors and samples at UHV conditions. Moreover, the chamber hosts a commercial electron-beam evaporator,<sup>3</sup> which directly aims at the sample stage in the cold microscope head for low-temperature evaporation of e.g. single iron adatoms.

The control electronics are connected to the microscope head with electric cables that enter the UHV system via UHV feedthroughs at the top of the cryostat. Radio frequency (RF) noise can couple into the system via these cables, which limits the energy resolution in scanning tunneling spectroscopy experiments, where the tunneling

---

<sup>3</sup>EFM-3, FOCUS GmbH, 65510 Hünstetten, Germany

current is measured as a function of the applied bias voltage [90]. Hence, the RF noise is filtered from the electrical lines with low-pass filters mounted between the UHV feedthroughs and the cables connected to the control electronics. As described in detail in Ref. [91], this leads to an increased performance in scanning tunneling spectroscopy and inelastic tunneling spectroscopy (IETS) experiments [92–94]. Throughout this work the bias voltage is applied to the sample and the tunneling current is measured via the tip using a FEMTO DLPCA-200 trans-impedance amplifier.<sup>4</sup>

### 3.2. qPlus sensor

The microscope is equipped with a so-called qPlus sensor [37]. The sensor and its physical properties are described in detail in Ref. [54]. Therefore, this section only serves as a brief introduction. In the first design of the sensor one prong of a quartz tuning fork, as found in quartz wristwatches, was glued to a heavy substrate while the second prong was allowed to oscillate freely [37]. For STM/AFM measurements a sharp tip was mounted on the end of the prong [37]. In this work third-generation qPlus sensors have been used, which were invented in 2011 [95]. These sensors feature only a single quartz prong, while the fixed prong of the original tuning fork versions is replaced by a larger quartz plate, which can be easily glued to a ceramic substrate [96]. Figure 3.1(a) shows a photograph of a custom-built third generation qPlus sensor (type qPlus M4 [54]) as it is used in the Omicron microscope. The Omicron sensor holder consists of a ceramic substrate (white), which is glued to a round gold-coated metal plate that stands on three legs [not shown in Fig. 3.1(a), a full image of the sensor holder tripod is shown in Fig. 4.1 of Ref. [84]]. Two of the legs are bent towards the substrate to connect the sensor to the STM and AFM signal lines, while the third leg establishes an electric ground connection of the sensor holder. The qPlus sensor is glued with its thicker base onto the ceramic substrate with non-conductive glue.<sup>5</sup> As it can be seen in the close-up photograph shown in Fig. 3.1(b), the sensor has two gold electrodes on its prong, which end in rectangular contact pads at the left end of the sensor. These electrodes are connected to the bent legs of the sensor holder using conductive glue.<sup>6</sup> One electrode is used to detect the deflection signal (AFM electrode), and the second one electrically contacts the tip at the end of the prong (STM electrode). When the free prong is bent, surface charges are formed due to the piezoelectric effect of quartz, which are directly proportional

<sup>4</sup>FEMTO Messtechnik GmbH, 10179 Berlin, Germany.

<sup>5</sup>EPO-TEK H70E, Epoxy Technology, Inc., Billerica, Massachusetts, United States of America.

<sup>6</sup>EPO-TEK H20E, Epoxy Technology, Inc., Billerica, Massachusetts, United States of America.

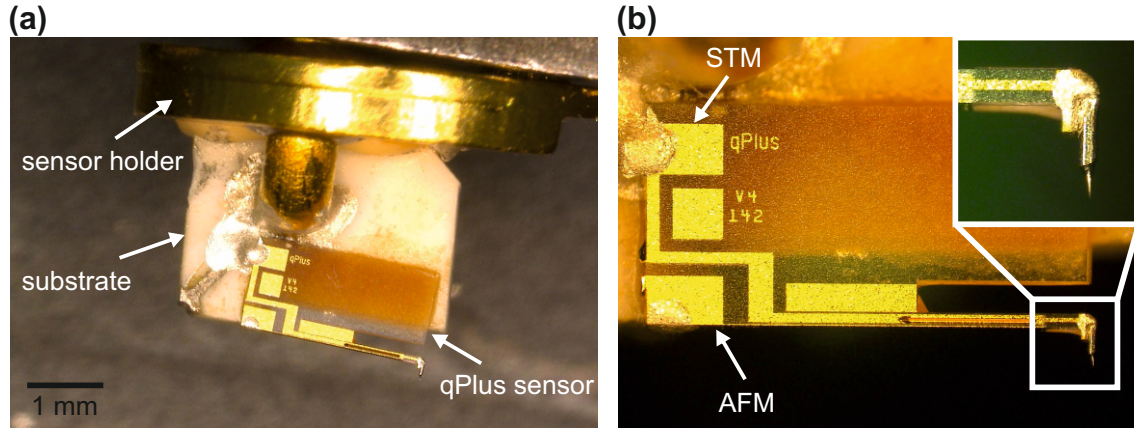


**Figure 3.1.: Custom-built qPlus sensor used in the Omicron microscope.**

(a) Photograph of a qPlus sensor (type qPlus M4 [54]) mounted on an Omicron sensor holder. The qPlus sensor is glued to a ceramic substrate and electrically connected to two legs of the sensor holder tripod. (b) Close-up photograph of the qPlus sensor. The sensor has two separate gold electrodes to simultaneously detect the STM and AFM signal. Inset: Zoom in the area marked by the white box. An electrochemically-etched tungsten tip ( $50\ \mu\text{m}$  diameter) is glued with conductive glue to the end of the free prong.

the sensor deflection amplitude  $A$ . These surface charges can be collected via the AFM electrode on the qPlus sensor that is electrically connected to the AFM signal line. The resulting current is detected with a current-to-voltage amplifier to measure the sensor amplitude and frequency [97]. This method of deflection detection is a major simplification compared to the original design of the AFM where the cantilever deflection was detected with STM [9] or the commonly-used optical detection in AFM experiments using Si cantilevers [50]. The latter is especially problematic if experiments are to be performed in non-transparent, biologically-relevant liquids, where the piezoelectric detection of the qPlus sensor deflection is still possible [98].

If the tip material is conductive, a tunneling current can be detected simultaneously. The inset of Fig. 3.1(b) shows a zoom-in of the end of the free prong, in this case hosting an electrochemically-etched  $50\ \mu\text{m}$  thick tungsten wire as the tip, which is electrically connected to the STM electrode. Due to its larger dimensions compared to traditional Si cantilevers, the qPlus sensor can be equipped with various types of tips from different materials [99]. This possibility enabled optimization of experiments at ambient conditions [100] and liquid environments [98], observation of spin contrast without an external magnetic field by using magnetic tips [27] and usage of superconductive tips [92].

A further benefit of the qPlus sensor are the high stiffness values of quartz tuning forks that are in the range of  $\text{kN/m}$  [75]. As explained in section 2.2, to study short-

range forces, optimal oscillation amplitudes are on the order of the length scales of these interactions [75]. As short-range tip-sample interactions have typical decay lengths of  $\lambda \approx 50$  pm and below, the sensor is generally excited to oscillate with  $A = 50$  pm throughout this work. The high stiffness values of the qPlus sensor prevent the jump-to-contact problem present in AFM experiments with soft Si cantilevers that have stiffnesses on the order of several N/m [59]. If the restoring force  $F_{\text{spring}} = kA$  is smaller than the maximum attractive tip-sample force  $F_{\text{ts}}^{\text{max}}$ , the cantilever may snap to the sample in an uncontrolled way [50]. This problem can be overcome if the oscillation amplitude is increased so that  $F_{\text{spring}} > F_{\text{ts}}^{\text{max}}$  [59, 99]. As a consequence, soft Si cantilevers generally need to oscillate at amplitudes on the order of several nm up to tens of nanometers in UHV environments [12, 59]. Hence, the sensitivity to short-range tip-sample interactions is greatly diminished.

Before a new sensor is transferred to the UHV system, its quality should be checked at ambient conditions by measuring the sensor's thermally-excited resonance peak [54]. This measurement is described in detail in Refs. [54, 76, 101, 102]. The thermal noise peak is useful to determine key properties of the sensor like the resonance frequency  $f_0$ , the quality factor  $Q$  and the experimental voltage sensitivity  $S_V$ . According to the equipartition theorem each degree of freedom of a harmonic oscillator holds a thermal energy of  $\frac{1}{2}k_B T$ . The sensor gets thermally excited and the average potential energy is equal to this thermal energy, which results in [101]

$$\frac{1}{2}k(A_{\text{rms}}^{\text{th}})^2 = \frac{1}{2}k_B T. \quad (3.1)$$

For a standard qPlus sensor with  $k = 1800$  N/m this yields a thermal amplitude of  $A_{\text{rms}}^{\text{th}} = 1.52$  pm at  $T = 300$  K. The sensitivity  $S_V$  relates the generated voltage at the output of the AFM amplifier due to thermal excitation  $V_{\text{out}}^{\text{th}}$  to  $A_{\text{rms}}^{\text{th}}$  as the output voltage generated for a given deflection,  $S_V = V_{\text{out}}^{\text{th}}/A_{\text{rms}}^{\text{th}}$ . In the control unit of the microscope  $S_V^{-1}$  is used as a calibration factor to translate the voltage at the AFM amplifier output into the actual amplitude  $A$ . Only sensors that show a single resonance peak and a quality factor of  $Q > 3000$  should be transferred to the UHV system. However, the value for  $S_V$  determined by the thermal peak method in ambient conditions is not valid for the AFM amplifier used in the LT-UHV setup, because  $S_V$  depends both on the sensor and on the amplifier. In order to determine the sensitivity at low temperatures, the equilibrium tip-sample distance  $z_{\text{eq}}$  is recorded as a function of the (potentially wrongly calibrated) amplitude  $A$  in STM feedback on a metal surface like Cu(111) [92, 103]. For sufficiently large amplitudes  $A > 500$  pm,  $z_{\text{eq}}(A)$  depends linearly on  $A$  with a slope close to unity [103]. If the slope  $\alpha$  of the recorded

### 3 Experimental setup and measurement techniques

---

$z_{\text{eq}}(A)$  curve differs from 1, the sensitivity needs to be corrected as  $S_V = S'_V/\alpha$ , where  $S'_V$  is the original sensitivity used to calibrate the amplitude.

A key property of sensor and amplifier is the deflection detector noise density  $n_q$ , which describes how precise the sensor deflection can be determined. It is related to the sensitivity via  $n_q = n_{\text{el}}/S_V$ , where  $n_{\text{el}}$  is the electrical noise density of the amplifier, i.e. the noise floor in the power spectral density of the amplifier output [54]. The Omicron setup typically achieves a deflection detector noise density of  $n_q \approx 50 \text{ fm}/\sqrt{\text{Hz}}$ . For a standard measurement bandwidth of  $B = 50 \text{ Hz}$  this results in an error in the deflection measurement of  $\delta q = n_q \sqrt{B} = 0.35 \text{ pm}$ . As it will be discussed in section 4.3.2, the measurement noise caused from the error in the deflection detection is the dominant contribution in the low-temperature AFM experiments presented within this work and its magnitude can be effectively diminished by reducing the bandwidth  $B$ .

### 3.3. Tip preparation and characterization

A stable and well-defined tip apex configuration is crucial for performing AFM experiments, as on the one hand this ensures repeatability and on the other hand knowledge of the tip apex configuration facilitates the theoretical description of the measurements. After the initial preparation of a new sensor with field evaporation to clean off oxide layers on the tip (see section 3.1), the tips are further prepared on a Cu(111) surface, which is partly covered with single CO molecules. This section describes the tip preparation and characterization protocol for single-atom metal and CO-terminated tips, as they have been used for the experiments presented in chapters 4 and 5. In chapter 6, experiments with O-terminated Cu tips are discussed. These tips are prepared on a partially oxidized Cu(110) surface, as explained in section 6.1.

#### 3.3.1. CO/Cu(111) sample preparation

For tip preparation and consecutive scanning, at first, a clean Cu surface needs to be prepared. The Cu(111) sample is cleaned by repeated sputtering and annealing cycles [104]. For the sputtering the preparation chamber is pumped with the turbomolecular pump and Ar gas is dosed via a leak valve into the chamber until a constant pressure of  $2.0 \times 10^{-6} \text{ mbar}$  is obtained. The ion getter pump is switched off during the sample preparation. The sample is then sputtered for 20 minutes with  $\text{Ar}^+$  ions, which are accelerated to a kinetic energy of  $E_{\text{kin}} = 1.0 \text{ keV}$ . By shooting  $\text{Ar}^+$  ions

onto the sample surface contaminants are removed and multiple atomic layers of the Cu crystal are ablated, which generally results in a relatively rough surface with only small terraces [105]. As a next step, the Ar gas is pumped out of the chamber and the surface is annealed for 20 minutes at a temperature of about 410 °C, which results in a flat sample surface with single-atom steps and terraces with dimensions on the order of several 100 nm<sup>2</sup>. Depending on the contamination level this cleaning cycle (consisting of 20 minutes sputtering, followed by 20 minutes annealing) is repeated 2–5 times in order to clean the Cu single crystal.

Copper crystallizes in a face-centered cubic (fcc) lattice and has a cubic lattice constant of  $a_0 = 361.5$  pm [106]. Hence, the Cu(111) surface shows a hexagonal lattice with a nearest-neighbor distance of  $d_{nn} = a_0/\sqrt{2} = 255.6$  pm. The distance between (111) planes is  $d_{(111)} = a_0/\sqrt{3} = 208.7$  pm [107]. Steps on Cu(111) should therefore be integer multiples of  $d_{(111)}$ , where a step height of  $1 \times d_{(111)}$  corresponds to a single-atom step. Figure 3.2(a) shows an STM topography image recorded of the Cu(111) sample after cleaning with sputtering and annealing, showing two step edges. From the line profile shown in Fig. 3.2(b), extracted along the blue line in Fig. 3.2(a), it follows that both steps are single atom steps, as their height  $h$  is in agreement with  $d_{(111)}$ .

Tip preparation and characterization on the Cu(111) surface requires single CO molecules adsorbed on the Cu(111) sample, as described in section 3.3.2 and 3.3.3. Since CO desorbs from Cu surfaces well below room temperature, the sample is transferred directly to the microscope head after cleaning and cooled down to 4.4 K. To adsorb CO molecules on the sample the gate valve between the preparation and analysis chamber is opened and CO gas is leaked to the preparation chamber via the gas line system until a pressure of  $p_{LT} \approx 3 \times 10^{-9}$  mbar is established in the analysis chamber. During this process the ion getter pump in the preparation chamber is switched off, which results in a pressure of  $p_{prep} \approx 2 \times 10^{-6}$  mbar in the preparation chamber. Subsequently, the thermal shields of the microscope are opened for 2 – 5 minutes depending on the desired amount of CO. As described in section 3.3.2, the tips are prepared by repeated collisions with the Cu sample. Experience has shown that when the CO density is too high, it is difficult to prepare a stable tip. Therefore, the optimal CO coverage for tip preparation is below 0.01 ML CO (ML: monolayer). A dosage time of 2 minutes results in a coverage of about 0.002 ML CO. Figure 3.2(c) shows an STM topography image of a clean Cu(111) sample after CO dosing. The single CO adsorbates appear as dark spots in the STM topography when probed with a metal tip at small bias voltages [108–110]. Cu(111) hosts a two-dimensional surface state at the Fermi level  $E_F$  and as shown in Ref. [108] surface

### 3 Experimental setup and measurement techniques

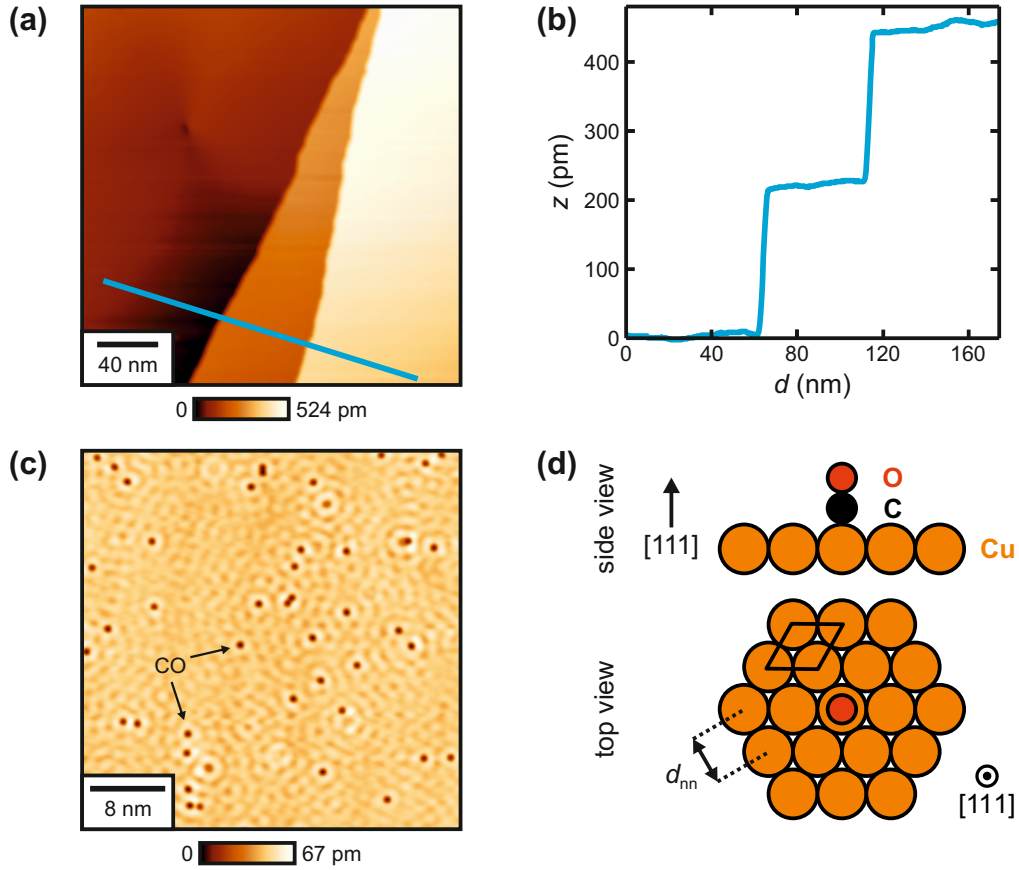


**Figure 3.2.: The CO/Cu(111) sample.** (a) STM topography image recorded of the Cu(111) sample after cleaning with sputter and anneal cycles. Two single-atom steps can be identified in the image. Imaging parameters:  $V_b = -10$  mV,  $\langle I \rangle = -100$  pA,  $A = 50$  pm. (b) Line profile extracted from the image in (a) along the blue line. The single-atom steps show the expected height of approximately  $d_{(111)} = 208.7$  pm. (c) STM topography image of the Cu(111) surface after CO adsorption. CO molecules appear as dark features in the STM topography images. Imaging parameters:  $V_b = -10$  mV,  $\langle I \rangle = -100$  pA,  $A = 50$  pm. Scattering of surface state electrons at defects and CO molecules causes the appearance of a standing wave pattern in STM images at small bias voltages. (d) Schematic of the CO adsorption position on Cu(111). Top: Side view. Bottom: Top view. Single CO molecules adsorb on top positions on Cu(111). The nearest-neighbor distance between Cu atoms is  $d_{nn} = 255.6$  pm.

state electrons get repelled by CO adsorbates, which leads to a local depletion of the electron density of states at  $E_F$ . Hence, the tunneling current gets reduced above the CO molecules and the tip has to approach closer to the sample to maintain the tunneling current setpoint. Surface state electrons scatter at step edges, point defects and adsorbates, which causes the formation of standing-wave patterns (Friedel oscillations [111]) caused by interference of the scattered surface state electrons [112] as visible in Fig. 3.2(c). Figure 3.2(d) shows the adsorption geometry of CO molecules on Cu(111) (top: side view, bottom: top view). The CO molecules adsorb on top

sites with the oxygen atom pointing away from the surface [113, 114]. The hexagonal unit cell of the Cu(111) surface lattice and the nearest-neighbor distance  $d_{\text{nn}}$  are additionally marked in the bottom part of Fig. 3.2(d).

#### 3.3.2. Tip preparation

As explained in section 2.2.2 the long-range vdW attraction can be significantly reduced if the tip apex is sharpened. The microscopic tip apex shape can be engineered on a clean Cu(111) sample partially covered with CO molecules. To change the microscopic shape of the tip apex the tip is repeatedly poked into a clean area of the Cu(111) sample [115, 116]. As explained in Ref. [29], the indentations can have three possible outcomes. First, tip material can be dropped on the sample, which leads to the appearance of bright bumps in STM images recorded in the vicinity of the poke position subsequently. Second, the tip can pick up sample material resulting in larger depressions in STM images. Third, the sample structure is not affected by the poke and only the tip apex atoms are rearranged. Depending on the poke strength the tip apex is modified only slightly or a strong reconfiguration is observed. Strong pokes are usually required for initial tip preparation with a new sensor or after a tip-sample collision on a non-conducting sample in order to reassure the metallic tip apex character. For a strong poke the tip is positioned in STM feedback (feedback settings:  $V_b = -10$  mV,  $\langle I \rangle = -100$  pA,  $A = 50$  pm) above a clean area on the Cu(111) sample. The tip is then approached to the sample several nanometers up to 50 nm while a bias voltage between 3 V and 5 V is applied. If the overall tip condition is close to the expected criteria, gentle pokes are used to modify only the first few atomic layers of the tip apex. For a gentle poke the tip is again placed above the clean Cu(111) surface in STM feedback and subsequently approached towards the sample by typically less than 2 nm, while a bias voltage less than 1 V is applied. Note that if a new sensor is first approached on a Cu(111) sample, the tip usually has to be poked into the Cu(111) surface multiple times before stable imaging conditions are established. Thereafter, it is assumed that the tip apex is covered with sample material, i.e. that tips showing a metallic character are terminated by Cu atoms [29, 117].

After the poke the tip is moved onto a clean spot on the bare Cu surface in STM feedback to judge the sharpness of the tip from the simultaneously recorded  $\Delta f$  signal. The sharpness of the tip directly affects the  $\Delta f$  signal, as the long-range van der Waals interaction between the tip and the surface lead to an attractive background signal and, hence, a more negative frequency shift. As a threshold value a frequency shift of  $\Delta f = -10$  Hz with the above settings ( $V_b = -10$  mV,  $\langle I \rangle = -100$  pA,  $A = 50$  pm)

### 3 Experimental setup and measurement techniques

---

has been established. If the  $\Delta f$  signal is less than  $-10$  Hz, the tip is considered as too blunt and the poking procedure is repeated. On the contrary, if the  $\Delta f$  signal is greater than  $-10$  Hz, the tip is considered as reasonably sharp. In this case the tip apex is further characterized with the COFI method [29] (section 3.3.3), which enables the determination of the number of tip apex atoms. Achieving atomic resolution requires a reasonable sharp tip apex ideally terminating in a single metal atom (single-atom metal tip). Due to the strong distance dependence of the tunneling current and the short-range tip-sample forces the tip-sample interaction is mainly mediated via the front-most tip apex atom. As will be shown in chapter 4, the theoretical description of experiments with single-atom metal tips can therefore often be confined to the interaction of the single, front-most apex atom with the sample, still reproducing the experiments with sufficient accuracy. However, as shown by Hofmann [86] single-atom metal tips turned out to be too reactive for stable imaging on certain sample systems like graphene.

Moreover, the spatial resolution achieved in STM and AFM experiments can be drastically increased by picking up an adsorbate [34], which is referred to as tip functionalization. Individual atoms and molecules can be picked up with the tip from a surface using vertical manipulation [113, 116, 118, 119]. CO-terminated tips (CO tips), prepared by picking up a single CO molecule from a surface [113, 120], effectively reduce the chemical reactivity of a single-atom metal tip [33, 34]. The usage of CO tips in AFM experiments has been introduced by Gross *et al.* in 2009, demonstrating atomic resolution imaging of a single pentacene molecule [33]. Since then, CO tips have been used in various AFM experiments enabling the real space observation of single organic molecules [121, 122], bond-order discrimination [18], imaging of different types of surfaces [35, 36, 123, 124] and adsorbates such as interfacial water [125] and metal clusters [32] with atomic resolution. Furthermore, CO tips enabled imaging of single metal adatoms with sub-atomic resolution [25, 32] and determination of the chemical reactivity of small iron clusters, that can be created with lateral manipulation on a Cu(111) surface [126, 127]. The imaging mechanisms in AFM experiments with CO tips will be discussed in detail in chapter 5 on the example of the ionic CaF<sub>2</sub>(111) surface.

The CO pickup process employed in this work is a modified version of the protocol originally proposed by Bartels *et al.* in Ref. [113]. As sketched in Fig. 3.3(a) a single-atom metal tip is placed in STM feedback (feedback settings:  $V_b = 1$  V,  $\langle I \rangle = 1$  nA,  $A = 50$  pm) above an isolated CO molecule adsorbed on a Cu(111) surface. After the STM feedback loop is switched off, the bias voltage is increased in 100 mV steps until for bias voltages between 2.3 V and 2.6 V either a sudden drop or increase in

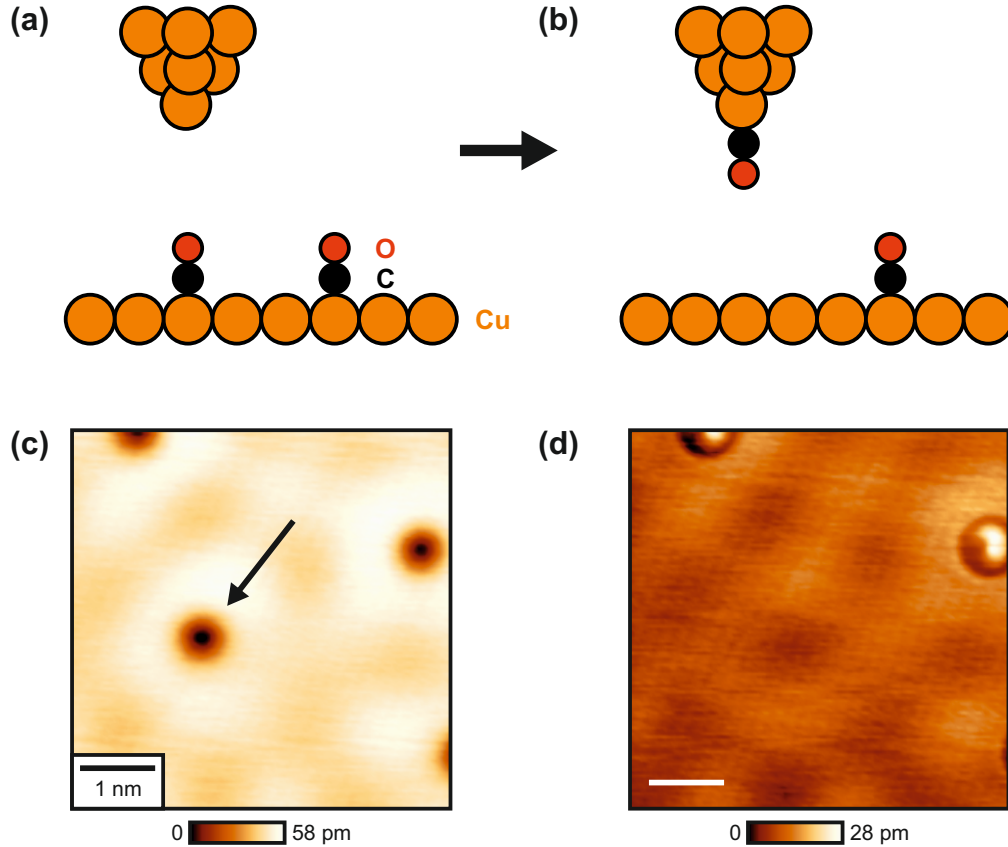


**Figure 3.3.: CO tip functionalization on Cu(111).** (a), (b) Schematic of tip functionalization with a single CO molecule. A tip terminated by a single metal atom is placed above a CO molecule adsorbed on a copper surface (a). After increasing the bias voltage in constant height, the CO flips and gets attached to the tip apex (b). (c) STM topography image of Cu(111) recorded with a metal tip before CO tip functionalization. (d) STM topography image of the same area as in (c) after picking up the CO molecule marked by the arrow in (c). The CO appearance changed with respect to (c). Imaging parameters for both images:  $V_b = -10$  mV,  $\langle I \rangle = -100$  pA,  $A = 50$  pm. All scale bars are 1 nm long.

the tunneling current signal is detected. An increase of  $\langle I \rangle$  is evidence for a lateral manipulation of the CO molecule away from the tip-sample junction, whereas a drop indicates the hopping of the CO molecule to the tip apex as sketched in Fig. 3.3(b). A successful CO tip functionalization can be judged from a change in the STM appearance of CO adsorbates imaged with either CO or metallic tips as illustrated in Fig. 3.3(c),(d). Figure 3.3(c) shows an STM topography image recorded of CO/Cu(111) with a single-atom metal tip, where the individual CO molecules appear as approximately 50 pm deep depressions. Afterwards, the CO molecule marked by the arrow has been picked up with the metal tip. Figure 3.3(d) shows an STM topography image of the same area as imaged in Fig. 3.3(c) after the CO pickup.

### 3 Experimental setup and measurement techniques

---

The molecule that was transferred to the tip apex is no longer visible on the surface and the remaining CO adsorbates resemble a “sombbrero”-like shape with a bright center [113].

Typically, the CO pickup process described above works only for circularly-symmetric single-atom metal tips. The sharpness of the tip apex (i.e. the number of metal atoms in the front-most layer of tip atoms) can be initially judged from the depth of the CO depressions in the STM topography. While the CO molecules are imaged as approximately 50 pm deep depressions with single-atom metal tips as shown in Fig. 3.3(c), the CO adsorbates appear less deep when imaged with blunter metal tips. Furthermore, it can occur that the CO molecule adsorbs at the tip apex in a tilted configuration due to an inherent asymmetry of the single-atom metal tip apex. Thus, the tip apex needs to be characterized at the atomic scale before and after the CO pickup attempt. In this work, tip characterization of metal and CO-terminated tips is performed with the so-called COFI method that will be introduced in section 3.3.3.

#### 3.3.3. Tip characterization with the COFI method

The tips used for the experiments presented in this work have been characterized with the carbon monoxide front atom identification (COFI) method [30–32]. In COFI the tip is scanned at constant-height above a CO molecule adsorbed on a Cu(111) surface, which is schematically shown in Fig. 3.4(a). The COFI method exploits the upright adsorption geometry of individual CO molecules on Cu(111): CO molecules adsorb on top sites with the oxygen atom pointing away from the surface [114, 128] as sketched in Fig. 3.4(a). Due to the smaller diameter of oxygen compared to metal atoms the CO adsorbate acts as a probe [30, 31, 129]. The resulting constant-height  $\Delta f$  image, the COFI image, shows the atomic configuration of the tip apex. To atomically resolve the tip apex the tip usually has to be approached to a tip-sample distance just before the molecule would get manipulated laterally during the constant-height scan. Initially, the different patterns in COFI images were interpreted as signatures of the crystallographic orientation of different single-atom metal tips [29–31]. In 2015, Emmrich *et al.* performed the reverse experiment. They imaged single metal adatoms and various small metal clusters adsorbed on a Cu(111) surface with a CO tip [32]. The constant-height  $\Delta f$  images of the metal adatoms and clusters showed striking similarities to the COFI images recorded of different metal tip apices. From these findings it was concluded that the number of tip apex atoms in the first atomic layer and their geometric configuration are imaged by the COFI method [32]. A similar imaging mechanism was also found when probing individual CO molecules

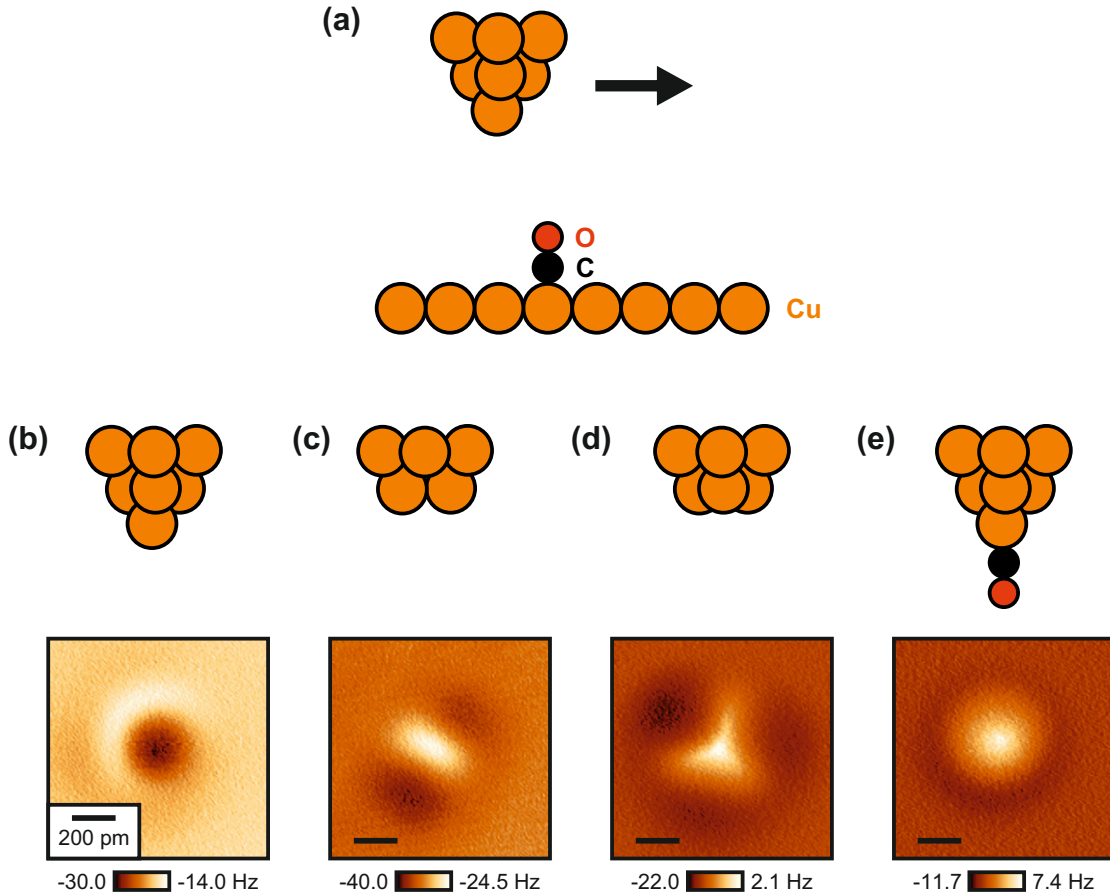


**Figure 3.4.: The COFI method.** (a) Schematic of the COFI method. A tip is scanned in constant-height across a CO molecule adsorbed on a Cu(111) surface to characterize the tip apex. (b)–(e) Representative COFI images of frequently observed tip apex configurations during tip preparation (bottom row) with sketches of the atomic configuration (top row). COFI image of (b) a single-atom metal tip, showing a single attractive feature (dark); (c) a two-atom metal tip apex, showing two attractive features; (d) a three-atomic tip apex, showing three attractive features; (e) a CO-terminated tip, showing a repulsive feature (bright). All scale bars are 200 pm long.

adsorbed on a nickel oxide surface [130, 131] and the dangling bonds on a Si(111)- $7 \times 7$  surface [31]. Interestingly, tunneling current maps recorded simultaneously to the constant-height COFI images on Cu(111) reflect the number and the geometric configuration of tip apex atoms after image processing but not in the raw data [30]. Recently, Gretz *et al.* extended the COFI method to the Pt(111) surface showing atomic contrast also in simultaneously-recorded raw tunneling current maps, which was attributed to an increased spatially-localized conductance through the CO adsorbate on Pt(111) [110].

Figure 3.4(b)–(e) show examples of COFI portraits of different tip apices that are frequently observed during tip preparation. The COFI image of a single-atom

### 3 Experimental setup and measurement techniques

---

metal tip as shown in Fig. 3.4(b) presents a circularly-symmetric attractive feature (dark) with a repulsive ring (bright) around it. In most cases the tip is slightly tilted with respect to the sample normal and the repulsive ring appears rather in the form of a sickle [126]. As already mentioned above this COFI portrait closely resembles the appearance of single metal adatoms when probed with a CO tip [25, 32]. The interaction between a CO tip and single metal adatoms is analyzed in detail in Ref. [25]. While the repulsive ring originates from Pauli repulsion between the CO and the metal atom, the two interaction partners can undergo a transition from a physisorbed to a chemisorbed state. Specifically, there is a hybridization of the electronic states of the CO molecule and the metal adatom when the tip is placed exactly in the center of the adatom, which leads to a strong attraction [25]. For preparation of a CO-terminated tip a symmetric single-atom metal tip is required, which can be ensured by observing a circularly-symmetric COFI portrait. Most frequently, the poke action does not result in a single-atom metal tip but in a tip terminated by more than one metal atom. In Fig. 3.4(c) a COFI image of a two-atomic tip and in Fig. 3.4(d) a COFI image of a three-atomic tip apex are shown. Each of the dark, attractive features which are separated by repulsive parts is interpreted as a single metal atom in the front-most atomic tip layer, as confirmed by the above-mentioned reverse experiment in Ref. [32]. COFI images can also be recorded of CO-terminated tips to ensure a successful CO tip functionalization and a circularly-symmetric tip apex. The COFI image of a CO tip recorded at close tip-sample distances as shown in Fig. 3.4(e) exhibits a circularly-symmetric repulsive feature (bright) with an attractive ring (dark) around it. The repulsive feature originates in Pauli repulsion between the two CO molecules, while the attractive ring is formed due to attractive van der Waals interaction at larger tip-sample distances [16, 21]. The CO-CO interaction is analyzed in detail in chapter 6 for the case of a CO molecule adsorbed on Cu(110).

A major benefit of the COFI method is the ability to directly characterize the atomic composition of the tip apex *in-situ*. For the experiments presented in chapters 4 and 5 the tips have been characterized with COFI before and after each measurement session on a CaF<sub>2</sub>(111) sample. If the COFI portraits of the tip recorded before and after the experiment are equal, it is proof that the tip apex remained stable during the complete experiment on the CaF<sub>2</sub>(111) surface.

# 4. High-precision AFM measurements on $\text{CaF}_2(111)$ with an atomically-characterized metal tip

*Most of the work presented in this chapter has been published in New Journal of Physics [132].<sup>1</sup> Parts of the text, figures and interpretations are identical to the publication. The author performed all experiments, implemented the electrostatic point charge calculation and carried out the complete data analysis with support from the co-authors of Ref. [132]. Initial experimental results and a first version of the model are presented in the author's Master thesis [85]. Therefore, parts of this chapter, particularly the theoretical considerations in sections 4.1 and 4.2, build upon the work presented in Ref. [85].*

Traditional AFM experiments on bulk ionic crystals generally involve poking the tip into the sample to generate a sharp apex. This covers the tip apex with a cluster of sample atoms and therefore leaves the tip termination and polarity unknown. Even with the assumption that the tip ends in one of the ionic species of the surface, atomic identification requires indirect theoretical characterization [133, 134] or adsorbed marker molecules [66, 135]. Furthermore, in order to achieve atomic resolution, AFM measurements with these poorly-characterized tips usually have to be conducted at close tip-sample distances where the tip-sample forces are in the nanonewton regime [14]. However, as already mentioned in the introduction, these strong tip-sample forces can lead to lateral and vertical relaxations of the tip apex [16–18, 21–23] and induce relaxations in the sample [19, 20]. In particular, tip relaxation and sample perturbation have been major problems in AFM studies of bulk ionic crystals, where sample relaxations greater than 100 pm were observed [14, 15]. Above ionic surfaces, when the tip is close to the sample, short-range chemical and van der Waals interactions can play a dominant role in AFM images [35, 136]. At larger tip-

---

<sup>1</sup>A. Liebig, A. Peronio, D. Meuer, A. J. Weymouth and F. J. Giessibl, *High-precision atomic force microscopy with atomically-characterized tips*, New J. Phys. **22**, 063040 (2020).

## 4 High-precision AFM measurements on $\text{CaF}_2(111)$ with an atomically-characterized metal tip

---

sample separations, electrostatic interactions have been shown to dominate the AFM contrast [35, 74, 137]. Hence, for non-perturbative imaging of a bulk ionic crystal in a deep non-contact regime an atomically-characterized tip with a well-defined electric field configuration is necessary.

Single-atom metal tips expose a dipole with its positive pole pointing towards the surface [35, 36, 136, 137] and are therefore suitable to probe ionic crystals. This is attributed to the Smoluchowski effect [138], according to which the negative electron charge distribution does not follow the sharp curvature of a step edge, or in this case of the tip apex. Instead it smears out, leading to a protrusion of the positive charge distribution coming from the atomic cores. As explained in section 3.3 the apex of a metal tip can be characterized at the atomic scale with the COFI method on a  $\text{Cu}(111)$  surface. In this way, a suitable metal tip ending in a single front atom can be prepared by a sequence of poking with intermediate COFI analysis until a single atom tip is obtained. Consequently, by gaining control over the atomic-scale tip apex composition and knowing its polarity, interpretation of experimental AFM data recorded with such an atomically-characterized tip is much more straightforward.

This chapter reports on high-precision AFM experiments on a  $\text{CaF}_2(111)$  surface with an atomically-characterized single-atom metal tip. First, the  $\text{CaF}_2(111)$  sample system is introduced and the theoretically-expected distance dependence of the electric field outside an ionic crystal is derived (see section 4.1). Second, an electrostatic point charge calculation to simulate the experimental AFM data of the  $\text{CaF}_2(111)$  surface is described (see section 4.2). Afterwards, experimental data recorded of the  $\text{CaF}_2(111)$  surface with a single-atom metal tip are compared to the calculation (see section 4.3.1). The experiment was performed at tip-sample distances where the atomic AFM contrast decayed to less than 1 pN and implications of measurement noise on experimental AFM data recorded in this tip-sample distance regime are described in section 4.3.2. Then, based on the experimental characterization of the second layer of tip atoms, the accuracy of the calculation is improved to reproduce small but measurable asymmetries in the experimental images of  $\text{CaF}_2(111)$  (see section 4.3.3). Finally, possible influences of a polarization of the tip apex in the electric field of the sample or tip-induced relaxations of sample atoms are discussed in section 4.3.4.

## 4.1. CaF<sub>2</sub>(111) surface

Crystals of the rock-salt structure possess charge inversion symmetry, which means that multiplying the ionic charges with  $-1$  just shifts the atomic pattern by half a cubic lattice vector [139]. Hence, assignment of atomic species to the features in AFM images required additional theoretical considerations [133, 134] or usage of marker molecules with a known adsorption site [66, 135], as described above. The CaF<sub>2</sub>(111) surface is an ionic surface that lacks charge inversion symmetry and has been used for this reason to identify the charge at the AFM tip apex [14, 15, 140–142]. This section first describes the CaF<sub>2</sub>(111) surface structure and then derives the distance dependence of the electric field outside of an ionic crystal surface.

### 4.1.1. Surface structure

Calcium fluoride (CaF<sub>2</sub>) crystallizes in a face-centered cubic (fcc) lattice and has a lattice constant of  $a_0 = 546$  pm [143]. The crystal has a three-atomic basis, with a Ca<sup>2+</sup> ion at the lattice origin  $(0, 0, 0)$  and two F<sup>-</sup> ions at  $\pm(a_0/4, a_0/4, a_0/4)$ . Figure 4.1(a) shows a side view of the CaF<sub>2</sub>(111) surface. The crystal cleaves naturally along the  $\{111\}$  planes and the surface layer consists solely of negatively charged F<sup>-</sup> ions [143]. Crystals cleaved along the (111) plane have to be terminated by complete, electrically neutral F<sup>-</sup>-Ca<sup>2+</sup>-F<sup>-</sup> triple layers that are spaced by  $a_0/\sqrt{3} = 315$  pm, as otherwise the surface would possess an infinitely high surface energy [144]. The three sublayers of one triple layer are spaced by 79 pm [143]. Figure 4.1(b) shows a top view of the CaF<sub>2</sub>(111) surface. The surface unit cell (drawn black) presents three high-symmetry sites that correspond to the different ions of the topmost triple layer. The surface F<sup>-</sup> ions are spaced by  $a_0/\sqrt{2} = 386$  pm and form a hexagonal lattice [143]. In the following, these F<sup>-</sup> ions will be called F<sub>top</sub><sup>-</sup> and the ions in the lower F<sup>-</sup> layer will be called F<sub>bot</sub><sup>-</sup>.

Initially, CaF<sub>2</sub>(111) samples were glued onto a sample holder and transferred directly to the microscope head after cleaving in UHV conditions. Similar to the findings in Refs. [145] and [146] this lead to strong charging of the surfaces and therefore, approaching to the surface was not possible without strong attractive long-range interaction between tip and sample already several  $\mu\text{m}$  away from the surface. Hence, for the AFM experiments presented in this chapter a CaF<sub>2</sub>(111) sample was screwed onto a modified sample holder and cleaved in ambient conditions. It was then transferred to the UHV system and annealed several hours at about 550 °C in order to remove contaminants due to the ambient cleavage and surface charges [146–148].

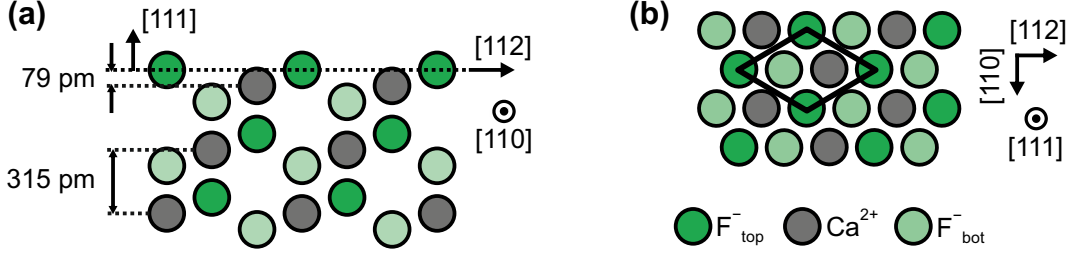


**Figure 4.1.: Schematic of the CaF<sub>2</sub>(111) surface.** (a) Side view of the CaF<sub>2</sub>(111) surface. The surface layer consists solely of negatively charged F<sup>-</sup> ions. The crystal is built up from electrically neutral F<sup>-</sup>-Ca<sup>2+</sup>-F<sup>-</sup> triple layers that are spaced by 315 pm, where the sublayers are spaced by 79 pm [144]. (b) Top view of the CaF<sub>2</sub>(111) surface. The surface unit cell (marked black in the image) presents three inequivalent sites, corresponding to the different ions of the topmost triple layer. Figure adapted from Ref. [132].

#### 4.1.2. Decay length of the electric field outside an ionic crystal

In 1928 Lennard-Jones and Dent predicted that the electric field outside an ionic crystal decays exponentially with distance, where the decay length is determined by the crystal lattice constant [149]. In this section, the decay length of the electric field will be derived and applied to calculate the decay length of the field above the CaF<sub>2</sub>(111) surface.

The potential  $V(\mathbf{r})$  at position  $\mathbf{r}$  above a crystal surface has the periodicity of the surface itself in the  $x$  and  $y$  directions. Hence, it can be expanded in a Fourier series as [150, 151]

$$V(\mathbf{r}) = \sum_{\mathbf{K} \neq \mathbf{0}} V_{\mathbf{K}}(z) e^{i\mathbf{K} \cdot \mathbf{r}}, \quad (4.1)$$

and the sum contains only plane waves

$$e^{i\mathbf{K} \cdot \mathbf{r}} = e^{i(m_1 \mathbf{a}_1^* + m_2 \mathbf{a}_2^*) \cdot \mathbf{r}} = e^{iK_x x} e^{iK_y y} e^{iK_z z}, \quad (4.2)$$

where  $\mathbf{K} = m_1 \mathbf{a}_1^* + m_2 \mathbf{a}_2^*$  is a surface reciprocal lattice vector,  $m_1$  and  $m_2$  are integers, and  $\mathbf{a}_1^*$  and  $\mathbf{a}_2^*$  are the surface reciprocal primitive vectors [152]. Note that the sum in eq. (4.1) excludes the component  $V_0$ . As the crystal unit cell is electrically neutral, this component can be taken as 0 [151, 153]. Furthermore, as  $\mathbf{a}_1^*$  and  $\mathbf{a}_2^*$  have no  $z$  component, the plane waves in eq. (4.2) do not depend on  $z$  and eq. (4.1) translates into

$$V(\mathbf{r}) = \sum_{\mathbf{K} \neq \mathbf{0}} V_{\mathbf{K}}(z) e^{iK_x x} e^{iK_y y} \quad (4.3)$$

Outside the crystal (where no charges are present) the potential must fulfill the Laplace equation  $\nabla^2 V(\mathbf{r}) = 0$  [152]. For the potential described by eq. (4.3) this

leads to

$$\sum_{\mathbf{K} \neq \mathbf{0}} V_{\mathbf{K}}(z)(-K_x^2) e^{i\mathbf{K} \cdot \mathbf{r}} + V_{\mathbf{K}}(z)(-K_y^2) e^{i\mathbf{K} \cdot \mathbf{r}} + \partial_z^2 V_{\mathbf{K}}(z) e^{i\mathbf{K} \cdot \mathbf{r}} = 0 \quad (4.4)$$

$$\Leftrightarrow \sum_{\mathbf{K} \neq \mathbf{0}} e^{i\mathbf{K} \cdot \mathbf{r}} \left( V_{\mathbf{K}}(z)(-K_x^2) + V_{\mathbf{K}}(z)(-K_y^2) + \partial_z^2 V_{\mathbf{K}}(z) \right) = 0. \quad (4.5)$$

Equation (4.5) can only be true if all summands are zero themselves [150] and with  $e^{i\mathbf{K} \cdot \mathbf{r}} \neq 0$ , always, one obtains

$$V_{\mathbf{K}}(z)(-K_x^2) + V_{\mathbf{K}}(z)(-K_y^2) + \partial_z^2 V_{\mathbf{K}}(z) = 0. \quad (4.6)$$

This differential equation can be solved by

$$V_{\mathbf{K}}(z) = V_{\mathbf{K},0}(z) e^{\pm \sqrt{K_x^2 + K_y^2} z} = V_{\mathbf{K},0}(z) e^{\pm Kz}, \quad (4.7)$$

where  $K = \sqrt{K_x^2 + K_y^2}$  is the magnitude of the surface reciprocal lattice vector  $\mathbf{K}$ . The solution with the plus sign in eq. (4.7) is unphysical as this would describe a diverging potential far from the surface, leaving only the solution

$$V_{\mathbf{K}}(z) = V_{\mathbf{K},0}(z) e^{-\sqrt{K_x^2 + K_y^2} z} = V_{\mathbf{K},0}(z) e^{-Kz} = V_{\mathbf{K},0}(z) e^{-z/\lambda}. \quad (4.8)$$

Hence, the potential is described by exponentially decaying components  $V_{\mathbf{K}}(z)$  with their decay length  $\lambda$  given by the reciprocal lattice vector  $\mathbf{K}$ . Components originating from longer  $\mathbf{K}$  vectors decay faster than components originating from shorter  $\mathbf{K}$  vectors. Therefore, far from the surface the potential is dominated by the components originating in the shortest  $\mathbf{K}$  vectors, i.e. the surface reciprocal primitive vectors  $\mathbf{a}_1^*$  and  $\mathbf{a}_2^*$  that have a length  $a^*$ . Neglecting the components from longer  $\mathbf{K}$  vectors, the decay length  $\lambda$  of the potential  $V$  is defined according to eq. (4.8) as

$$\lambda = \frac{1}{K} = \frac{1}{a^*}. \quad (4.9)$$

The  $z$  component of the electric field is given by  $E_z(z) = -\partial V/\partial z$ , and will therefore show the same distance dependence as the potential. For a square lattice with lattice constant  $a$  one obtains  $\lambda = a/2\pi$  as derived by Giessibl [74]. As shown in section 4.1.1, the surface unit cell vectors of CaF<sub>2</sub>(111) have a length  $d = 386$  pm, which results in  $a^* = (4\pi)/(\sqrt{3}d)$ . Hence, the decay length of the electric field normal to the CaF<sub>2</sub>(111) surface is

$$\lambda = \frac{1}{a^*} = \frac{\sqrt{3}d}{4\pi} = 53.2 \text{ pm}. \quad (4.10)$$

It is interesting to note that  $\lambda$  depends only on the crystal lattice constant and is not influenced by the positions or ionic charges of the basis atoms.

### 4.2. Electrostatic point charge calculation

In section 4.1.2 the exponential distance dependence of the electric field outside an ionic crystal has been derived. The decay length of the electric field is of a similar magnitude as the exponential decay length of the tunneling current observed in STM. Because of this, Giessibl suggested in 1992 that an ionic crystal surface can be imaged with a polarized AFM tip with atomic resolution [74]. This section introduces an electrostatic calculation to simulate the electrostatic tip-sample interaction between a charged tip apex and the CaF<sub>2</sub>(111) surface. The calculation has been implemented in MATLAB and the code is provided in the appendix A.1.

Figure 4.2 shows a schematic of the electrostatic calculation. The sample atoms are modeled as point charges with  $q_{\text{Ca}} = +1.730 e$  and  $q_{\text{F}} = -0.865 e$ , where  $e$  denotes the elementary charge, as calculated by density functional theory (DFT) [154]. Initially, the model crystal was created following the hexagonal lattice of the CaF<sub>2</sub>(111) surface which resulted in a rhomboid structure. In this configuration, however, finite size effects were observed in the calculated electrostatic potential leading to a tilt in the potential for a given height  $z$  above the surface. Hence, the model crystal structure was optimized to minimize these finite size effects. Precisely, a circular slab with a radius of 57 nm has been used as a model crystal. Since the decay length of the potential above the CaF<sub>2</sub>(111) surface is  $\lambda = 53.2$  pm as shown in section 4.1.2 and the distance between two triple layers is 315 pm, contributions of lower triple layers to the total electrostatic potential are negligible: the second triple layer contributes only  $\exp(-315 \text{ pm}/53.2 \text{ pm}) = 0.27\%$  to the total potential. Therefore, only one triple layer was taken into account in the calculation. The total electrostatic potential  $V(\mathbf{r})$  at position  $\mathbf{r}$  has been calculated by summing the contributions  $V_i$  of all sample atoms as

$$V(\mathbf{r}) = \sum_i V_i(\mathbf{r}) = \frac{1}{4\pi\epsilon_0} \sum_{\mathbf{R},j} \frac{q_j}{|\mathbf{r} - (\mathbf{R} + \mathbf{b}_j)|}, \quad (4.11)$$

where  $\mathbf{R} = n_1\mathbf{a}_1 + n_2\mathbf{a}_2 + n_3\mathbf{a}_3$  is a vector of the direct lattice,  $\mathbf{a}_1$ ,  $\mathbf{a}_2$  and  $\mathbf{a}_3$  are the unit cell vectors, and  $q_j$  is the charge of the atom at site  $\mathbf{b}_j$  of the basis ( $j \in \{1, 2, 3\}$ ). The potential has been calculated in a 3D grid with a spacing of 5 pm and a total volume of  $1 \text{ nm} \times 1 \text{ nm} \times 1 \text{ nm}$ , centered on the crystal surface to minimize finite size

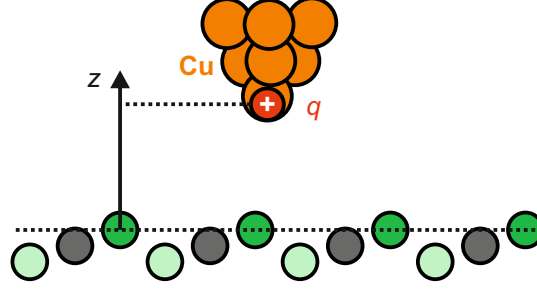


**Figure 4.2.: Schematic of the electrostatic calculation.** The tip, in this case a single-atom metal tip, is represented by a single point charge  $q$  and the sample atoms are modeled with point charges,  $q_{\text{Ca}} = +1.730e$  and  $q_{\text{F}} = -0.865e$ . The tip-sample distance  $z$  is defined as the vertical distance between the point charge modeling the tip apex and the  $\text{F}_{\text{top}}^-$  nucleus. Figure adapted from Ref. [132].

effects. The  $z$  component of the electric field  $E_z$  was calculated by

$$E_z(z) = -\frac{\partial V}{\partial z}. \quad (4.12)$$

The force  $\mathbf{F}$  acting on a point charge  $q$  in an electric field  $\mathbf{E}$  is given by

$$\mathbf{F} = q \mathbf{E}. \quad (4.13)$$

From eq. (4.13) it follows that the vertical force component acting between the tip, which is represented by a single point charge  $q$  in the calculation (see Fig. 4.2), and the sample is calculated as

$$F_z(z) = q E_z(z). \quad (4.14)$$

From this, the vertical tip-sample force gradient follows as

$$k_{\text{ts}}(z) = -\frac{\partial F_z(z)}{\partial z} = q \frac{\partial^2 V}{\partial z^2}, \quad (4.15)$$

which is then converted to frequency shift  $\Delta f$  according to eq. (2.7) in order to be able to directly compare the calculation to the experimental data. The sensor stiffness  $k = 1800 \text{ N/m}$ , the resonance frequency  $f_0 = 55\,051 \text{ Hz}$  and the oscillation amplitude  $A = 50 \text{ pm}$  were set to match the parameters of the sensor used in the experiment. The tip-sample distance  $z$  is defined as the vertical distance between the point charge modeling the tip apex and the  $\text{F}_{\text{top}}^-$  nucleus (see Fig. 4.2). From eqs. (4.12) to (4.15) it follows that the exponential distance dependence of the electrostatic potential is also reflected in the  $z$  component of the electric field, the tip-sample force, and the frequency shift. Additionally, the latter two quantities depend linearly on the effective

## 4 High-precision AFM measurements on CaF<sub>2</sub>(111) with an atomically-characterized metal tip

---

charge at the tip apex  $q$ ,

$$\Delta f \propto q e^{-z/\lambda}. \quad (4.16)$$

This dependency has certain implications that need to be considered in the following discussion. First, according to eq. (4.16), the effect of an offset  $\Delta$  in the  $z$  axis

$$q e^{-(z+\Delta)/\lambda} = q e^{-\Delta/\lambda} e^{-z/\lambda} = q' e^{-z/\lambda} \quad (4.17)$$

is equivalent to changing the tip charge from  $q$  to  $q' = q e^{-\Delta/\lambda}$ . It is important to note that the real tip-sample distance in an AFM experiment cannot be determined easily. In context of eq. (4.17), by comparing the experiment to the simulation, it is therefore not possible to independently determine the experimental tip-sample distance and the tip apex charge  $q$  in the calculation. Hence, the point charge that represents the tip has been fixed to match the value given by Schneiderbauer *et al.* in Ref. [137]. The single-atom metal tip has been modeled with  $q = +0.13 e$  [137].

Second, the exponential decay of the short-range electrostatic interaction enables determination of the experimental tip-sample distance with high accuracy. The apex charge of  $q = +0.13 e$  corresponds to a dipole moment of 0.87 D (1 D = 0.2082 eÅ), when assuming a dipole distance of 135 pm as given in Ref. [137]. The dipole at the tip apex of a single-atom Cu tip has also been reported by Gross *et al.*, who found 0.52 D [136] and Ellner *et al.*, who obtained 1.5 D [35]. Thus, if the actual tip apex charge differs from the value used here by a factor of two (all of the above values are within this range), eq. (4.16) translates into

$$e^{\delta z/\lambda} = 2, \quad (4.18)$$

where  $\delta z$  is the uncertainty in determining the experimental tip-sample distance, and thus,

$$\delta z = \lambda \ln 2 \approx 36.9 \text{ pm}. \quad (4.19)$$

Similarly, changing the ionic charges of the sample atoms from  $q_{\text{Ca}} = +1.730 e$  and  $q_{\text{F}} = -0.865 e$  to  $q_{\text{Ca}} = +2 e$  and  $q_{\text{F}} = -1 e$  is equivalent to a change in tip-sample distance of only 8 pm, and will therefore not strongly affect the results.

### 4.3. Experimental results

The experiments presented in this chapter have been conducted with a qPlus sensor (type qPlus M4 [54]), equipped with an iridium tip that was sharpened by a focused-ion-beam (FIB),<sup>2</sup> showing a resonance frequency of  $f_0 = 55\,051$  Hz and a quality factor of  $Q = 811\,485$ . As explained in section 2.2, to increase the sensitivity to short-range tip-sample interactions the oscillation amplitude of the sensor should be set to a similar magnitude as the decay length of the tip-sample interaction [75]. As derived in section 4.1.2 the electric field outside a  $\text{CaF}_2(111)$  surface decays exponentially with a decay length of  $\lambda = 53.2$  pm. Hence, the sensor oscillation amplitude was set to  $A = 50$  pm.

Single-atom metal tips were characterized and prepared on a  $\text{Cu}(111)$  sample as explained in section 3.3. Before the experiments on the  $\text{CaF}_2(111)$  sample, the tip was characterized with the COFI method, and changes in the atomic structure of the tip apex were excluded by investigating the tips again on  $\text{Cu}(111)$  after data was acquired of  $\text{CaF}_2(111)$  similar to Ref. [31]. Note that this procedure is experimentally challenging as first, a  $\text{Cu}(111)$  sample is inserted into the microscope, covered by CO molecules and then used to poke and characterize the tip. Second, the Cu sample is replaced by a  $\text{CaF}_2(111)$  sample and the measurements are conducted. As a last step, the samples are again exchanged and the tip apex is characterized by COFI on the  $\text{Cu}(111)$  sample again. If the tip suffered changes during data acquisition or sample transfer, the data had to be discarded.

Figure 4.3(a) shows a COFI image of the single-atom metal tip recorded before the measurement on the  $\text{CaF}_2(111)$  surface. As explained in section 3.3, the COFI image of a single-atom metal tip shows a circularly-symmetric, attractive center with a repulsive ring around it. Figure 4.3(b) shows the COFI image of the tip recorded after the measurements on  $\text{CaF}_2(111)$ . For direct comparison the two images were recorded at the same tip-sample distance, i.e. at the same relative distance to a given STM setpoint above the bare Cu surface, in this case 220 pm closer from ( $V_b = -10$  mV,  $\langle I \rangle = -100$  pA). In this way it was verified that the tip had not changed during the experiment. Note that the COFI image in Fig. 4.3(a) shows a slightly higher contrast compared to the image in Fig. 4.3(b). The reason is that the two imaging heights are not perfectly aligned: on  $\text{Cu}(111)$  STM topography images recorded at low bias voltage are governed by the Cu surface state and due to the interference pattern of the surface state with adsorbates, like adsorbed CO molecules, height differences of approximately 10 to 20 pm occur (see section 3.3) [112]. Figures 4.3(c) and (d)

<sup>2</sup>The sensor was fabricated by Daniel Meuer, the FIB sharpening was done by Dr. Tobias Preis.

## 4 High-precision AFM measurements on $\text{CaF}_2(111)$ with an atomically-characterized metal tip

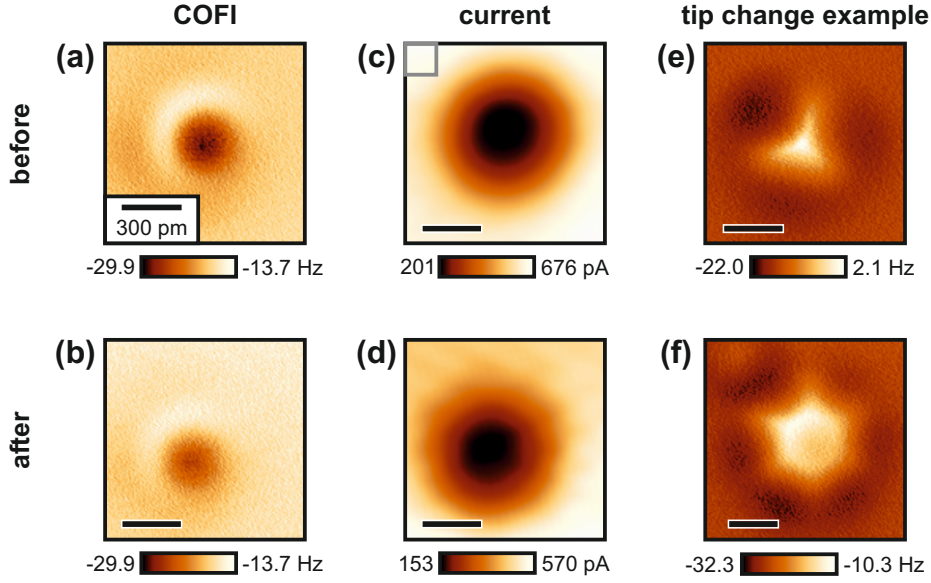


**Figure 4.3.: COFI images before and after the measurement on  $\text{CaF}_2(111)$ .** Left column: COFI images of the single-atom metal tip recorded before (a) and after (b) the measurement on  $\text{CaF}_2(111)$ . The images were recorded 220 pm closer from the STM setpoint ( $V_b = -10$  mV,  $\langle I \rangle = -100$  pA) on the bare Cu(111) surface. Center column: Simultaneously recorded tunneling current before (c) and after (d) the measurement on  $\text{CaF}_2(111)$ . The tunneling current images have been processed with a  $78 \text{ pm} \times 78 \text{ pm}$  Gaussian low-pass filter [155]. Right column: Example of COFI images before (e) and after (f) a tip change. A tip apex consisting of three atoms (indicated by three attractive features in the COFI image) changed to an apex with seven atoms. All scale bars are 300 pm long. Figure adapted from Ref. [132].

show the tunneling current maps recorded simultaneously with the COFI images in Fig. 4.3(a) and (b), respectively. Although the imaging voltage was set to  $V_b = 0$  V, the actual imaging voltage was approximately  $500 \mu\text{V}$  due to a slight offset in the bias voltage channel, resulting in the tunneling current signal. Indeed, comparing the average tunneling current signal in a  $156 \text{ pm} \times 156 \text{ pm}$  area in the left top corner of the images [marked by the gray square in Fig. 4.3(c)] indicates that the COFI image in Fig. 4.3(a) has been recorded approximately 10 pm closer to the surface as compared to Fig. 4.3(b) when assuming a tunneling current decay constant of  $\kappa \approx 11 \text{ nm}^{-1}$  (see section 2.1). It can be therefore concluded that within this experimental accuracy, the two COFI images were recorded with the same single-atom metal tip but with a difference of 10 pm in the tip-sample separation. For illustration, Figs. 4.3(e) and (f) show COFI images before and after a tip change occurred. In this case, a tip apex consisting of three atoms [Fig. 4.3(e)], which is indicated by three local minima in the  $\Delta f$  map, has changed into a tip apex with seven atoms [Fig. 4.3(f)].

After preparation and characterization, the single-atom metal tip was approached

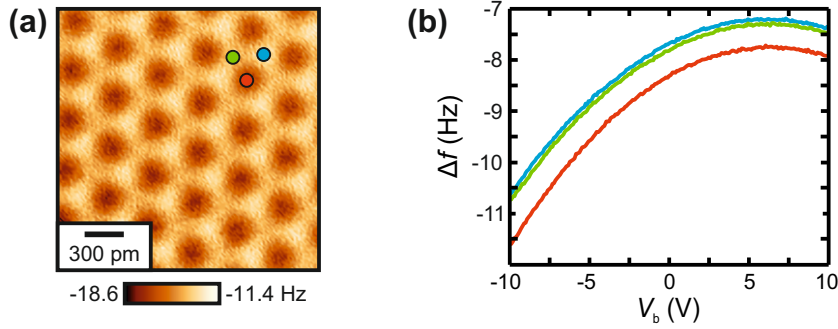


**Figure 4.4.: Determination of the contact potential difference.** (a) Constant-height frequency shift image of the  $\text{CaF}_2(111)$  surface recorded with the single-atom metal tip. The image has been recorded 90 pm closer from the setpoint. Setpoint on attractive site:  $A = 50$  pm,  $V_b = 5.8$  V,  $\Delta f = -7.8$  Hz. (b)  $\Delta f(V_b)$  curves (Kelvin parabolas) recorded on the three high-symmetry sites marked in the constant-height image. The apex voltage  $V_{\text{CPD}} = 5.8$  V was used as the imaging voltage to minimize the long-range electrostatic tip-sample interaction. Panel (b) adapted from Ref. [132].

to the  $\text{CaF}_2(111)$  surface. Figure 4.4(a) shows an experimental constant-height frequency shift image of the  $\text{CaF}_2(111)$  surface recorded with the single-atom metal tip. The image presents three prominent sites with the hexagonal symmetry of the  $\text{CaF}_2(111)$  surface namely a dark, a bright and a site of intermediate contrast. To minimize the long-range electrostatic interaction (compare section 2.2.3) a Kelvin parabola,  $\Delta f(V_b)$ , has been measured and the apex voltage  $V_{\text{CPD}}$  has been used as the imaging voltage  $V_b$  [Fig. 4.4(b)]. The overall electrostatic interaction is, however, slightly different on the three high-symmetry sites, which causes a slight shift of  $V_{\text{CPD}}$ . Hence, the actual imaging voltage was obtained by averaging the apex positions measured on the three prominent sites resulting in a voltage of  $V_b = 5.8$  V. All experimental data measured on the  $\text{CaF}_2(111)$  sample shown in this chapter have been measured with this bias voltage. Note that the measured value of  $V_{\text{CPD}}$  is comparable to previously reported values on the  $\text{CaF}_2(111)$  surface in Ref. [140, 156].

### 4.3.1. Comparison to the electrostatic calculation

To assign atomic species to the high-symmetry sites in the experimental image and to address the contrast mechanisms, the experimental data is compared to the electrostatic calculation introduced in section 4.2.

Figure 4.5(a) shows an experimental constant-height  $\Delta f$  image of the  $\text{CaF}_2(111)$  surface recorded 20 pm closer to the surface as compared to the image in Fig. 4.4(a). Again, the three high-symmetry sites can be seen in the image and from symmetry

## 4 High-precision AFM measurements on $\text{CaF}_2(111)$ with an atomically-characterized metal tip

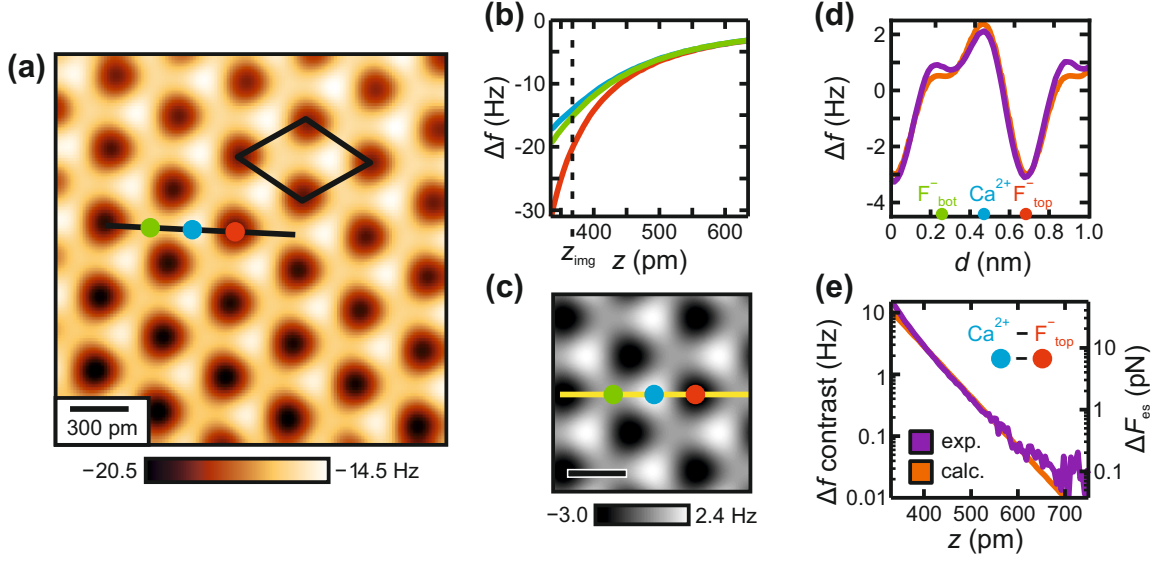


**Figure 4.5.: Experimental and calculated data of  $\text{CaF}_2(111)$ .** (a) Constant-height  $\Delta f$  image of the  $\text{CaF}_2(111)$  surface recorded with the single-atom metal tip. The unit cell defined in Fig. 4.1(b) is drawn black in the image. The image has been processed with a  $78 \text{ pm} \times 78 \text{ pm}$  Gaussian low-pass filter [157] to remove measurement noise before comparison between experiment and theory. (b) Experimental frequency shift versus distance  $\Delta f(z)$  curves recorded above the three high-symmetry sites marked in (a). The constant-height image has been recorded at the height  $z_{\text{img}}$ . (c) Calculated constant-height  $\Delta f$  image for a positively terminated tip obtained with the electrostatic calculation described in section 4.2. All scale bars are 300 pm long. (d) Comparison of experimental and calculated line profiles following the respective traces in (a) and (c). (e) Comparison of experimental and calculated  $\Delta f(z)$  contrasts, together with the calculated electrostatic force contrast  $\Delta F_{\text{es}}$ . Figure adapted from Ref. [132].

considerations it follows that these sites correspond to the positions of the atoms in the surface triple layer of  $\text{CaF}_2(111)$ . Figure 4.5(b) shows experimental frequency shift versus distance  $\Delta f(z)$  curves recorded above the three sites with the single-atom metal tip. The spectra show that the tip-sample interaction is attractive over the accessible  $z$  range as  $\Delta f$  is entirely negative. At smaller tip-sample separations, reversible tip relaxations occurred indicated by an increased AFM dissipation signal. In order to maintain the atomic configuration of the metal tip apex the tip has not been approached closer to the surface to prevent any irreversible tip changes. The constant-height image in Fig. 4.5(a) has been recorded at the height  $z_{\text{img}}$ . It is not easy to determine the real tip-sample distance in the experiment. In particular as  $\text{CaF}_2$  is an insulator, methods such as distance determination via the point-contact conductance as applied e.g. in Ref. [137] cannot be used. The tip-sample distance  $z$  has therefore been determined by fitting the experimental to the calculated  $\Delta f(z)$  contrast [compare Fig. 4.5(e), which will be discussed later] using the tip-sample

distance as a fit parameter. In this way, the closest tip-sample approach in the experiment has been determined to be  $z_0 = 335$  pm.

Figure 4.5(c) shows a calculated constant-height  $\Delta f$  image obtained from the electrostatic point charge calculation. Analogous to the experimental images, the calculated image presents three high-symmetry sites that correspond to the atoms in the surface triple layer of  $\text{CaF}_2(111)$ . Hence, it is possible to assign atomic species to the experimental data. As expected for the metal tip with a positive charge at the apex, the atoms of the surface  $\text{F}^-$  layer ( $\text{F}_{\text{top}}^-$ ) are imaged dark, i.e. they are most attractive in the constant-height images. The  $\text{Ca}^{2+}$  atoms are imaged bright, i.e. they are least attractive. The atoms of the lower  $\text{F}^-$  layer ( $\text{F}_{\text{bot}}^-$ ) correspond to the sites of intermediate contrast. Figure 4.5(d) shows experimental and calculated line profiles extracted along the traces marked in Figs. 4.3(a) and (c), respectively. To align the curves the average  $\Delta f$  over one surface period was subtracted from each line profile. Note that the contrast in Fig. 4.3(a) is slightly higher as compared to the corresponding line profile in Fig. 4.3(d). This can be attributed to the fact that the imaging plane has not been perfectly aligned with the sample, leading to a slightly higher contrast in the lower half of the image as compared to the upper half, e.g. the  $\text{F}_{\text{top}}^-$  atoms appearing darker in the bottom right corner as compared to the top left corner.

To quantify the agreement between experiment and theory a relative quadratic deviation between the measured and calculated profile curves has been calculated over one surface period. This comparison between experiment and theory via line profiles is done only at the imaging height of the constant-height image. In order to compare the atomic contrast and not the long-range background forces, the average  $\Delta f$  was subtracted from both the experimental and the calculated curves. The experimental short-range frequency shift  $\Delta f_{\text{exp}}^{\text{sr}}$  is calculated as

$$\Delta f_{\text{exp}}^{\text{sr}} = \Delta f_{\text{exp}}(x) - \frac{1}{X} \int_{x=0}^X \Delta f_{\text{exp}}(x) dx, \quad (4.20)$$

where  $\Delta f_{\text{exp}}(x)$  is the experimental line profile extracted from a constant-height image and  $X$  is the length of a single surface period, as defined by the size of the unit cell. Similarly, one obtains  $\Delta f_{\text{th}}^{\text{sr}}$  for the simulated frequency shift data. At first, the squares of the differences between experiment and calculation at each  $x$  position over one period of the curves are integrated:

$$\delta \Delta f_{\text{square}} = \int_{x=0}^X (\Delta f_{\text{exp}}^{\text{sr}}(x) - \Delta f_{\text{th}}^{\text{sr}}(x))^2 dx. \quad (4.21)$$

## 4 High-precision AFM measurements on CaF<sub>2</sub>(111) with an atomically-characterized metal tip

---

The relative quadratic deviation RQD between experiment and calculation is then obtained as

$$\text{RQD} = \frac{\delta \Delta f_{\text{square}}}{X \int_{x=0} (\Delta f_{\text{th}}^{\text{SF}}(x))^2 dx}, \quad (4.22)$$

analogous to a similar quantity used to determine the agreement of a model in low-energy electron diffraction (LEED) experiments ( $R_2$  factor) [158]. Finally, the accuracy of the electrostatic model can be defined as

$$\text{accuracy} = 1 - \text{RQD}. \quad (4.23)$$

For the line profiles shown in Fig. 4.5(d) this results in  $\text{RQD} = 1.9\%$ , yielding an accuracy of  $98.1\%$ . The high accuracy shows that the electrostatic calculation captures almost all the contrast measured with the single-atom metal tip on the CaF<sub>2</sub>(111) surface, i.e. that the AFM contrast is dominated by short-range electrostatic tip-sample interactions.

Furthermore, to determine the distance-dependent evolution of the  $\Delta f$  contrast, experimental and calculated  $\Delta f(z)$  spectra are compared. The experimental  $\Delta f(z)$  curves in Fig. 4.5(b) reflect the total tip-sample interaction, i.e. also the long-range background contributions, whereas the calculation considers only short-range electrostatics. Hence, to eliminate the long-range contribution in the experimental data the difference of  $\Delta f(z)$  spectra recorded above two atomic sites can be considered [159]. Figure 4.5(e) shows experimental and calculated  $\Delta f(z)$  contrasts on a logarithmic plot. The spectrum measured above the most attractive site [ $\text{F}_{\text{top}}^-$ , red in Fig. 4.5(a),(b)] is subtracted from the spectrum recorded above the least attractive site [ $\text{Ca}^{2+}$ , blue in Fig. 4.5(a),(b)] to obtain the total  $\Delta f(z)$  contrast. For tip-sample distances between 350 pm and 700 pm the measured  $\Delta f(z)$  contrast shows an exponential decay with a decay length of  $\lambda_{\text{exp}} = (53 \pm 3)$  pm. This is in good agreement to the predicted decay length of the electric field above the CaF<sub>2</sub>(111) surface of  $\lambda = 53.2$  pm, reflected in the calculated  $\Delta f(z)$  contrast. The agreement between the experimental and theoretically predicted distance dependencies of the  $\Delta f(z)$  contrasts demonstrates that the electrostatic model is sufficient to explain the AFM contrast measured with the metal tip for all accessible tip-sample distances. Specifically, this means that the AFM contrast is dominated by short-range electrostatic tip-sample interactions for all accessible tip-sample distances. This relationship justifies the determination of the real tip-sample distance  $z$  in the experiment by fitting the experimental to the calculated  $\Delta f(z)$  contrast, using the tip-sample distance as a fit parameter.

### 4.3.2. Atomic resolution with femtonewton force contrast

For tip-sample distances larger than 500 pm the  $\Delta f$  contrast lies in the millihertz regime, which corresponds to femtonewton electrostatic force contrasts [Fig. 4.5(e)]. Experimental constant-height images recorded at these distances are governed by measurement noise that exceeds the expected atomic corrugation.

If the frequency shift measurement in FM-AFM would not be subject to any error, infinitely small tip-sample force gradients could be measured. In a real system, noise in the frequency measurement  $\delta f$  translates into an error in the tip-sample force gradient  $\delta k_{\text{ts}}$  according to eq. (2.8) as [54]

$$\delta k_{\text{ts}} = 2k \frac{\delta f}{f_0}. \quad (4.24)$$

A detailed description of the four relevant noise contributions in FM-AFM can be found e.g. in Ref. [54] and hence, the following part briefly recapitulates the points relevant for the present work. *Thermal noise* has been already subject of discussion in the first publication about FM-AFM by Albrecht *et al.* [10]. The sensor gets randomly excited to oscillate due to the finite surrounding temperature, which leads to an error in the frequency detection given as [10, 54]

$$\delta f_{\text{th}} = \sqrt{\frac{k_B T f_0 B}{\pi k A^2 Q}}, \quad (4.25)$$

where  $k_B$  is Boltzmann's constant,  $T$  is the microscope temperature, and  $B$  is the measurement bandwidth. According to eq. (4.24) the thermal noise in the force gradient measurement follows as

$$\delta k_{\text{ts,th}} = \sqrt{\frac{4k k_B T B}{\pi A^2 f_0 Q}}. \quad (4.26)$$

The absolute thermal frequency noise [eq. (4.25)] can be described by introducing a thermal noise density  $n_{\Delta f, \text{th}}$  as [54]

$$n_{\Delta f, \text{th}} = \sqrt{\frac{k_B T f_0}{\pi k A^2 Q}}, \quad (4.27)$$

which describes the magnitude of thermal noise at a given bandwidth  $B$ . This noise density is constant with respect to its modulation frequency  $f_{\text{mod}}$  and therefore, thermal noise is often referred to as white thermal noise [54].

The precision of any length measurement and hence, also the measurement of the

## 4 High-precision AFM measurements on CaF<sub>2</sub>(111) with an atomically-characterized metal tip

---

cantilever deflection, is influenced by noise [54, 160]. The precision at which the cantilever deflection can be measured is described by the deflection detector noise density  $n_q$  that depends on the output voltage noise density  $n_{el}$  of the preamplifier as

$$n_q = \frac{n_{el}}{S_V}, \quad (4.28)$$

where  $S_V$  is the sensitivity of the sensor (and amplifier), defined as the generated voltage per deflection at the preamplifier output (see section 3.2) [97]. The uncertainty in the deflection measurement translates into an uncertainty in the phase and hence, also in the frequency measurement. The noise density of this *detector noise* has been obtained as [161]

$$n_{\Delta f, \text{det}} = \sqrt{2} \frac{n_q}{A} f_{\text{mod}}, \quad (4.29)$$

showing a linear increase with  $f_{\text{mod}}$ . The absolute noise in the frequency measurement is then obtained by integrating the square of the noise density with respect to  $f_{\text{mod}}$  from zero up to the bandwidth  $B$ , which results in [54]

$$\delta f_{\text{det}} = \sqrt{\frac{2n_q^2 B^3}{3A^2}}, \quad (4.30)$$

or in terms of the force gradient

$$\delta k_{\text{ts, det}} = \sqrt{\frac{8kn_q}{3} \frac{B^{3/2}}{f_0 A}}. \quad (4.31)$$

Kobayashi *et al.* [161] discussed a third contribution to frequency noise in FM-AFM that originates in the fact that the sensor is driven with its own, due to a finite  $n_q$  noisy oscillation signal, which excites the sensor slightly off resonance. This *oscillator noise* is inversely proportional to the quality factor and results in a frequency noise [54]

$$\delta f_{\text{osc}} = \sqrt{\frac{n_q^2 f_0^2 B}{2Q^2 A^2}}, \quad (4.32)$$

or, according to eq. (4.25) in a force gradient noise of

$$\delta k_{\text{ts, osc}} = \sqrt{2} \frac{kn_q}{Q} \frac{\sqrt{B}}{A}. \quad (4.33)$$

Similar to thermal noise, the noise density of oscillator noise is constant with respect

to the modulation frequency (white noise) [54]

$$n_{\Delta f, \text{osc}} = \frac{f_0 n_q}{\sqrt{2} A Q}. \quad (4.34)$$

Moreover, temperature changes will lead to slight changes in the sensor's oscillation frequency, which leads to a *thermal frequency drift noise* [54]. This is a major challenge in room-temperature and high-temperature environments. At low temperatures, i.e. in a thermally stable environment, influences of drift noise are low and will therefore be neglected in the following [76]. As all these noise sources are statistically independent, the total noise is obtained by adding the contributions defined in eqs. (4.25), (4.30) and (4.32) in quadrature [54]:

$$\delta f = \sqrt{(\delta f_{\text{th}})^2 + (\delta f_{\text{det}})^2 + (\delta f_{\text{osc}})^2}. \quad (4.35)$$

All of the noise contributions discussed above increase with increasing bandwidth  $B$ . Hence, by reducing the bandwidth and therefore also the scanning speed, these sources can be effectively reduced resulting in the ability to measure smaller force gradients [54]. Figure 4.6 illustrates the effect of sensor noise in experimental constant-height  $\Delta f$  images. The unprocessed experimental constant-height image depicted in Fig. 4.6(a) has been recorded at a tip-sample distance of  $z = 380$  pm, clearly resolving the three atomic sites of the  $\text{CaF}_2(111)$  surface triple layer. The inset shows a part of the image processed with a  $47 \text{ pm} \times 47 \text{ pm}$  Gaussian low-pass filter, revealing the theoretically-expected atomic  $\Delta f$  contrast of 4.2 Hz. The fast Fourier transformed (FFT) image [Fig. 4.6(b)] created from Fig. 4.6(a) shows six peaks that correspond to the surface reciprocal primitive vectors.

Figure 4.6(c) shows an unprocessed constant-height image recorded of the same spot on the surface as Fig. 4.6(a) but at an elevated tip-sample distance of  $z = 570$  pm. As in Fig. 4.6(c) the tip was 190 pm further away from the surface than in Fig. 4.6(a), the atomic contrast is expected to be decreased to  $\exp(-190 \text{ pm}/53.2 \text{ pm}) = 2.8\%$  of the initial value due to the exponential decay of the short-range electrostatic tip-sample interaction. This corresponds to a  $\Delta f$  contrast of only 118 mHz, or to an electrostatic force contrast of 350 fN, as illustrated in Fig. 4.5(e), which is masked by measurement noise. The FFT image [Fig. 4.6(d)] created from Fig. 4.6(c) still shows the six peaks that correspond to the surface reciprocal primitive vectors in the center but with much lower intensity than in Fig. 4.6(b). As explained above, the noise in FM-AFM experiments consists of different components that are inverse with spatial frequency (frequency drift noise), constant (white noise, thermal and oscillator noise) and linear

## 4 High-precision AFM measurements on CaF<sub>2</sub>(111) with an atomically-characterized metal tip

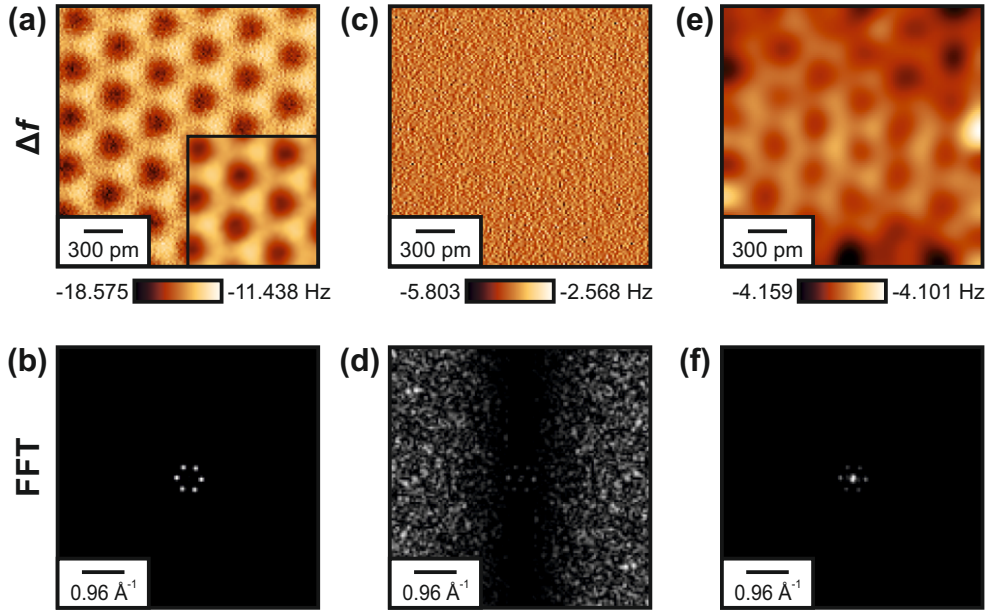


**Figure 4.6.: Experimental images with mHz contrast.** (a) Experimental constant-height  $\Delta f$  image of the CaF<sub>2</sub>(111) surface recorded at a tip-sample distance of  $z = 380$  pm. Inset: part of the image, processed with a  $47$  pm  $\times$   $47$  pm Gaussian low-pass filter [157], showing a  $\Delta f$  contrast of  $4.2$  Hz. (b) Fast Fourier transformed (FFT) image created from (a) resolving six peaks that correspond to the surface reciprocal primitive vectors. (c) Experimental constant-height  $\Delta f$  image recorded at a tip-sample distance of  $z = 570$  pm. The expected atomic contrast of only  $118$  mHz is masked by measurement noise. (d) Corresponding FFT image created from (c), still showing the six peaks corresponding to the reciprocal lattice, but dominated by measurement noise. (e) Same image as in (c), processed with a  $234$  pm  $\times$   $234$  pm Gaussian low-pass filter [157], again resolving the CaF<sub>2</sub>(111) atomic lattice. The strong features at the corners are an effect of the low-pass filtering. (f) FFT image created from (e), showing the increased signal-to-noise ratio after image processing. Figure adapted from Ref. [132].

with spatial frequency (detector noise). The FFT image shows a linear increase of noise with spatial frequency along the horizontal  $x$  direction indicating that detector noise is the dominant contribution. Note that the linear increase of noise with spatial frequency is only seen along the  $x$  direction and not along the  $y$  direction. In the  $x$  direction, which is the fast scan direction, the spatial frequency, i.e. the number of pixels scanned per second, is much higher than in the slow scan direction. As detector noise increases linearly with spatial frequency, it shows up mainly in the fast scan direction ( $x$ ) where it dominates the FFT image.

Neglecting frequency drift noise all noise contributions [eqs. (4.25), (4.30) and (4.32)] depend on the measurement bandwidth  $B$ . Hence, when reducing the scan speed,  $B$  can be effectively decreased and the frequency noise  $\delta f$  is reduced [54]. After

the measurement, low-pass filtering in the time domain (i.e. bandwidth reduction) can be performed by low-pass filtering in the spatial frequency domain, for example by processing the images with a Gaussian low-pass filter [54]. In this case, a scan bandwidth  $B_{\text{scan}}$  which is defined as the number of pixels scanned per second needs to be considered. During analysis of the effect of filtering on frequency noise it has been found empirically that processing an image with a  $n \times n$ -Gauss filter using the WSxM software [155] leads to an effective bandwidth  $B_{\text{eff}} = B_{\text{scan}}/(0.86 n)$ , where  $n$  is the pixel width of the Gauss filter. Consequently, this means that the experimental data are subject to two subsequent low-pass filters and the one with the lower bandwidth determines the frequency noise  $\delta f$ . The dependence of  $\delta f$  and its individual components on Gaussian low-pass filtering is shown in table 4.1. The parameters used to calculate the noise contributions were set to match the real experimental conditions, i.e.  $T = 4.4 \text{ K}$ ,  $f_0 = 55\,051 \text{ Hz}$ ,  $k = 1800 \text{ N/m}$ ,  $A = 50 \text{ pm}$ ,  $Q = 811485$  and  $n_q = 53 \text{ fm}_{\text{rms}}/\sqrt{\text{Hz}}$ . The unprocessed constant-height images in Fig. 4.6(a),(c) are  $2 \text{ nm} \times 2 \text{ nm}$  ( $128 \text{ px} \times 128 \text{ px}$ ) large and have been recorded at a scan speed of  $2 \text{ nm/s}$ , which leads to a scan bandwidth of  $B_{\text{scan}} = 128 \text{ Hz}$ . Hence, in case of unprocessed data the lower measurement bandwidth  $B = 50 \text{ Hz}$  determines the frequency noise rather than  $B_{\text{scan}}$ . By applying a Gauss filter to the constant-height images  $B_{\text{eff}}$  becomes smaller than  $B$  and replaces the latter in eqs. (4.25), (4.30) and (4.32). While thermal [eq. (4.25)] and oscillator noise [eq. (4.32)] are  $\propto B^{0.5}$ , detector noise [eq. (4.30)] is  $\propto B^{1.5}$ , and thus experiences the strongest decrease when  $B$  is reduced.

processing	raw data		Gauss $5 \text{ px} \times 5 \text{ px}$	Gauss $10 \text{ px} \times 10 \text{ px}$
bandwidth	$B = 50 \text{ Hz}$	$B_{\text{scan}} = 128 \text{ Hz}$	$B_{\text{eff}} = 30 \text{ Hz}$	$B_{\text{eff}} = 15 \text{ Hz}$
$\delta f_{\text{th}}$	3.8	6.1	3.0	2.1
$\delta f_{\text{det}}$	306.0	1253.4	142.2	50.3
$\delta f_{\text{osc}}$	0.4	0.6	0.3	0.2
$\delta f$	306.0	1253.4	142.2	50.3

**Table 4.1.:** Influence of Gaussian filtering on the noise in  $\Delta f$  images. As explained in the text, low-pass filtering the images results in an effective bandwidth  $B_{\text{eff}}$  that replaces the measurement bandwidth  $B$  in eqs. (4.25), (4.30) and (4.32). Values are given in mHz.

Indeed, processing the constant-height image in Fig. 4.6(c) with a  $234 \text{ pm} \times 234 \text{ pm}$  ( $15 \text{ px} \times 15 \text{ px}$ ) Gaussian low-pass filter reveals the atomically-resolved  $\text{CaF}_2(111)$  lattice [Fig. 4.6(e)]. The corresponding FFT image [Fig. 4.6(f)] shows the increased signal-to-noise ratio in the processed image with a strongly decreased contribution of detector noise and unchanged intensity of the six data peaks that correspond to

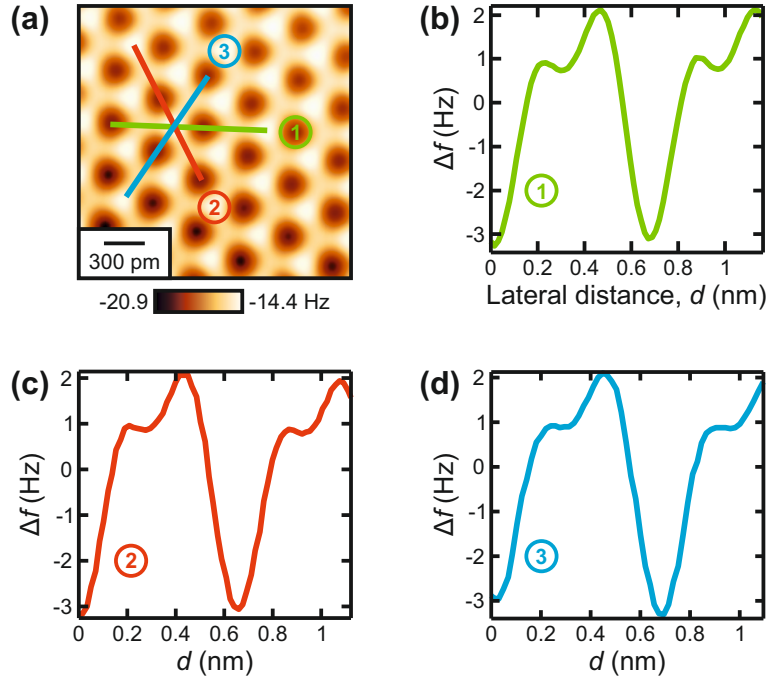


**Figure 4.7.:** Asymmetries in experimental constant-height  $\Delta f$  images recorded of CaF<sub>2</sub>(111). (a) Experimental constant-height  $\Delta f$  image of the CaF<sub>2</sub>(111) surface. The image has been processed with a 78 pm  $\times$  78 pm Gaussian low-pass filter [155]. (b)–(d) Line profiles extracted from the constant-height image along the high-symmetry directions of the surface marked in (a). The average  $\Delta f$  over one surface period was subtracted from each profile.

the surface reciprocal primitive vectors. The atomic contrast in the filtered image of 58 mHz is, however, lower than the theoretically expected contrast of 118 mHz. This can be attributed to the strong Gaussian low-pass filtering that leads to an averaging effect but is needed to resolve the atomic contrast in the constant-height image [54].

### 4.3.3. Improving the tip model by utilizing the COFI data

The CaF<sub>2</sub>(111) surface has a three-fold rotational symmetry with respect to an axis perpendicular to the surface. Line profiles extracted along the three high-symmetry directions of the surface from an experimental constant-height  $\Delta f$  image [Fig. 4.7(a)] are shown in Fig. 4.7(b)–(d). The average  $\Delta f$  value over one surface period was subtracted from each curve to align experiment and theory for comparison (see above). While the constant-height image appears symmetric at a first glance, slight differences between the line profiles can be identified. The green curve depicted in Fig. 4.7(b) shows a significant decrease between  $d = 0.2$  nm and 0.3 nm, which is less prominent in case of the red curve [Fig. 4.7(c)] and barely visible in the blue line profile that remains constant in this range. This asymmetry can be attributed to the fact that

the actual metal tip used in the experiments does not perfectly share the three-fold symmetry of the  $\text{CaF}_2(111)$  surface unlike a tip comprised by a single point charge as it is the case in the electrostatic calculation. Hence, asymmetries in the experimental images cannot be reproduced by a tip model consisting of a single point charge but require a tip model that takes into account atoms in the second or even further tip layers.

The COFI image recorded of the single-atom metal tip used in the experiment shows shallow attractive features outside the bright repulsive ring as indicated by the crosses in Fig. 4.8(a), which can be interpreted as signatures of atoms in the second tip layer. In the following, the information about the atomic tip apex structure obtained from the COFI characterization will be used to refine the theoretical tip apex description and to improve the agreement between the experimental data of  $\text{CaF}_2(111)$  and the electrostatic model. From the COFI image in Fig. 4.8(a) the lateral shifts  $(\Delta x_i, \Delta y_i)$  of the three second layer atoms with respect to the front atom (marked by the white cross) can be extracted. It is important to note that the COFI image is a point-reflected image of the atomic structure of the tip [32]. As an example, if a feature is 200 pm left of the front atom in the COFI image, i.e. in negative  $x$ -direction, it is 200 pm right of the front atom in real space. Consequently, the lateral shifts as read from the COFI image need to be multiplied by  $-1$  in order to obtain the lateral shifts  $(\Delta x_i, \Delta y_i)$  with respect to the front atom.

Subsequently, to calculate the magnitude of the additional contributions to the  $\Delta f$  contrast, the  $\Delta f$  signal strength of each second layer atom in the COFI image is compared to the  $\Delta f$  value of the front atom. As the  $\Delta f$  values in the COFI image are offset to negative values due to long-range background forces, this contribution needs to be subtracted from the COFI image. As a reference, the average  $\Delta f$  value in the top left area of the COFI image indicated by the black square in Fig. 4.8(a) has been calculated, which yields  $\Delta f_{\text{ref}} = -18.7 \text{ Hz}$ . From the line profiles in Fig. 4.8(b)–(d) the frequency shift values of the front atom  $\Delta f_{\text{front}} = -28.5 \text{ Hz}$  and the respective second layer atoms  $\Delta f_{\text{second},i}$  have been obtained. From this the relative magnitude  $P_i$  of the contribution of second layer atom  $i$  to the electrostatic interaction measured on  $\text{CaF}_2(111)$  can be calculated as

$$P_i = \frac{\Delta f_{\text{second},i} - \Delta f_{\text{ref}}}{\Delta f_{\text{front}} - \Delta f_{\text{ref}}}. \quad (4.36)$$

Here, it is assumed that the  $\Delta f$  contrast in the COFI image can be directly translated into the electrostatic contrast measured with the metal tip on the  $\text{CaF}_2(111)$  surface. Indeed, as the COFI image is recorded at a height where the tip-sample interaction

## 4 High-precision AFM measurements on $\text{CaF}_2(111)$ with an atomically-characterized metal tip

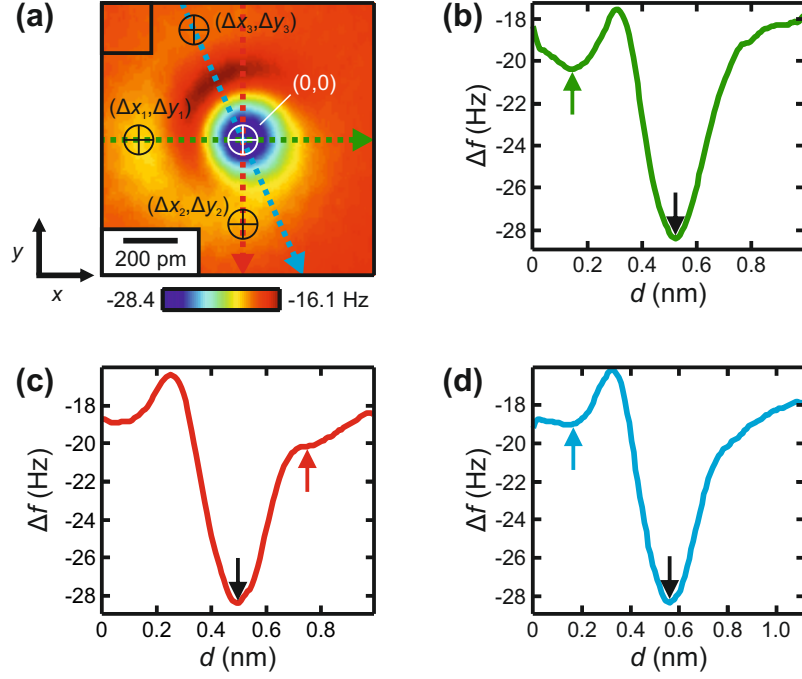


**Figure 4.8.: Extraction of second layer tip atoms from the COFI image.** (a) COFI image of the single-atom metal tip used in the experiment, filtered with a  $47 \text{ pm} \times 47 \text{ pm}$  Gaussian low-pass filter [155]. The crosses indicate first (white) and second layer (black) tip atoms, shifted with respect to the front atom by  $(\Delta x_i, \Delta y_i)$ . Note: yellow color indicates a local minimum. (b)–(d) Line profiles extracted along the directions indicated in (a). Arrows indicate positions of the front atom (black) and second layer atoms (colored). Figure adapted from Ref. [132].

is entirely attractive, the  $\Delta f$  contrast differences in the COFI image are a measure of the height differences between the tip apex atoms. Due to the exponential distance dependence of the electrostatic tip-sample interaction on  $\text{CaF}_2(111)$  a height difference of the additional tip apex atoms is equal to a smaller point charge at the same height as the front atom. Therefore, the relative  $\Delta f$  contrast in the COFI image  $P_i$  can be used in good approximation to determine the relative contribution of second layer tip atoms to the electrostatic tip-sample interaction on  $\text{CaF}_2(111)$ . Table 4.2 summarizes the lateral shifts  $(\Delta x_i, \Delta y_i)$  as well as the relative contribution  $P_i$  to the electrostatic interaction of each second layer atom. The contributions of the second layer atoms are more than five times smaller than the front atom contribution, which shows that including second layer atoms adds only a small correction to the single point charge model.

As both the geometrical tip structure (lateral shifts) as well as the magnitude of the additional interactions (which can be translated into a vertical offset, see section 4.2) are determined directly from the experimental data, the COFI image fixes all relevant

atom	$\Delta f_{\text{second},i}$	$P_i$	$\Delta x_i$	$\Delta y_i$
1	-20.4 Hz	0.17	400 pm	0 pm
2	-20.2 Hz	0.15	0 pm	250 pm
3	-19.0 Hz	0.03	100 pm	-420 pm

**Table 4.2.:** Relative signal strength and lateral shifts of second layer tip atoms with respect to the front atom as extracted from the COFI image. For the numbering of atoms refer to figure 4.8(a).

tip parameters. With this information, the theoretical tip apex description was refined to improve the agreement between the experiment and the electrostatic model. The total electrostatic interaction  $\Delta f_{\text{es}}(x, y, z)$  between the multi-atom tip and the  $\text{CaF}_2(111)$  surface is obtained by summing up the contributions of the individual atoms as

$$\Delta f_{\text{es}}(x, y, z) = \Delta f_{\text{front,es}}(x, y, z) + \sum_{i=1}^3 P_i \Delta f_{\text{front,es}}(x + \Delta x_i, y + \Delta y_i, z). \quad (4.37)$$

Here,  $\Delta f_{\text{front,es}}$  denotes the calculated frequency shift due to the electrostatic interaction between the front atom represented by the single point charge  $q$  and the  $\text{CaF}_2(111)$  surface as implemented in the original calculation described in section 4.2.

From the new data set, constant-height images  $\Delta f_{\text{es}}(x, y, z = \text{const.})$  were extracted and compared to the electrostatic calculation according to eqs. (4.22) and (4.23). Figure 4.9(a) shows a calculated constant-height image at a tip-sample distance of  $z = 370$  pm. Figure 4.9(b)–(d) shows a comparison between experimental data (dotted), the single point charge model (black, dashed) and the calculation including second layer tip atoms (solid). The profile curves were extracted along the directions marked in Fig. 4.9(a). By construction, the calculation with only one charge modeling the tip apex fails to reproduce the experimentally observed differences in the line profiles, especially for lateral distances from  $d = 200$  pm to 300 pm. On the contrary, including second layer tip atoms in the calculation reproduces the experimental data with excellent agreement. Calculating the average accuracy according to eq. (4.23) for the three profile curves in Fig. 4.9(b)–(c) results in an accuracy of 99.8%. To quantify how the more refined model reproduces the experimental data as a function of tip-sample distance  $z$ , the accuracy can be calculated over a distance range of 100 pm resulting in an average of 99.5%. Table 4.3 summarizes the accuracy as a function of tip-sample distance for the metal tip incorporating second layer atoms. The line profiles used to calculate the accuracy are shown in appendix A.2. The excellent agreement of the simulation to the experimental data shows that static electrostatics are the dominant physics between the surface and the tip.

## 4 High-precision AFM measurements on CaF<sub>2</sub>(111) with an atomically-characterized metal tip

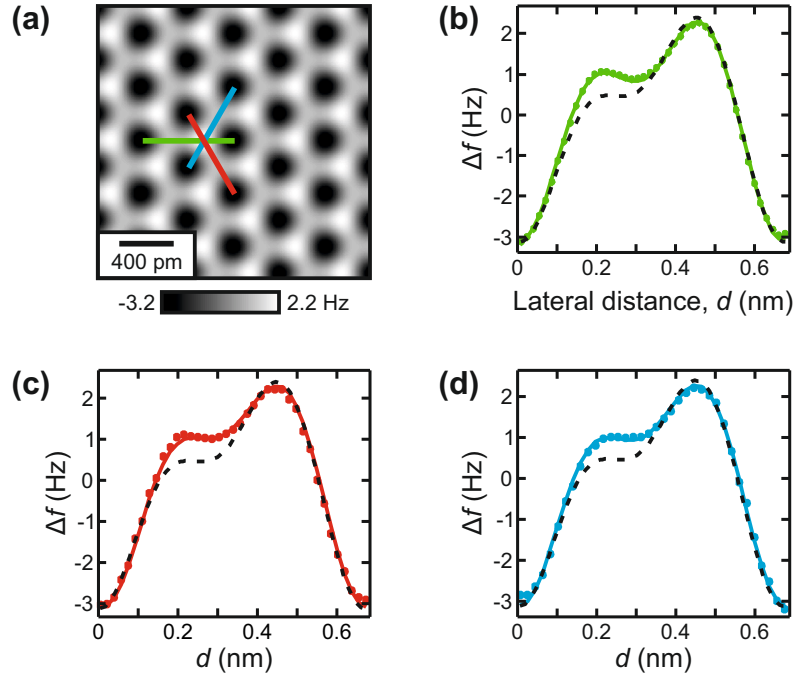


**Figure 4.9.:** Comparison between experimental and calculated line profiles for the calculation including second layer tip atoms. (a) Calculated  $\Delta f$  image of CaF<sub>2</sub>(111) obtained from the multi-atom tip model. (b)–(d) Line profiles along the three high-symmetry directions marked in (a). The calculation including four point charges (solid) matches the asymmetry of the experimental curves (dots) and gives a better agreement than the single point charge model (dashed). Figure adapted from Ref. [132].

$z$	370 pm	400 pm	430 pm	450 pm	470 pm
accuracy	99.8 %	99.6 %	99.6 %	99.3 %	99.3 %

**Table 4.3.:** Accuracy of the electrostatic model of the metal tip incorporating second layer atoms as a function of tip-sample distance  $z$ .

### 4.3.4. Influence of tip polarizability and sample relaxations

All of the above findings depend on the electrostatic tip-sample interaction where tip and sample are represented by static point charges, i.e. the magnitude as well as the relative positions of the charges does not change. Polarization of the tip in the electric field of the sample would lead to a deviation in the shape of the exponential decay of eq. (4.16) as already examined by Giessibl in 1992 [74], who considered that the electric field of an ionic crystal could induce a dipole in the tip. To determine a potential influence of a polarized tip apex the additional force acting on a tip due to a polarization of the tip apex atom can be calculated. The induced dipole moment

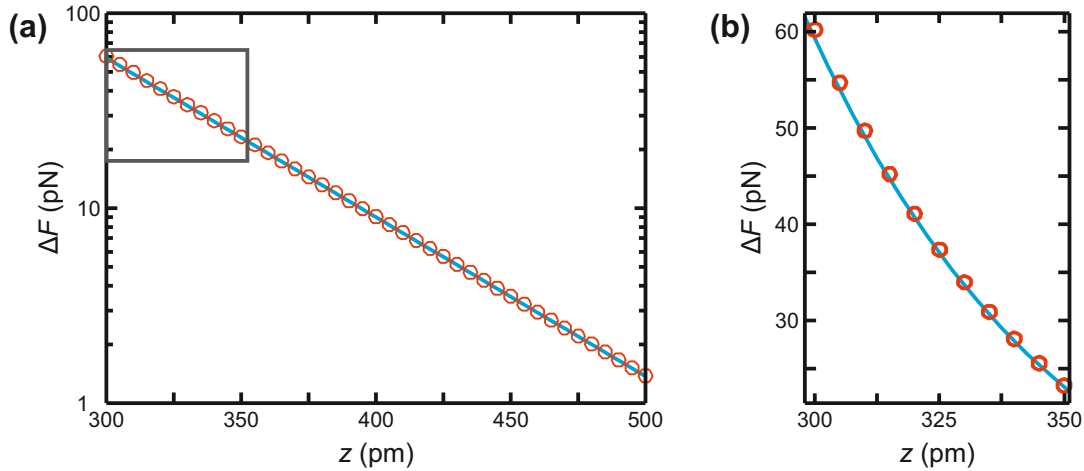


**Figure 4.10.: Effects of tip polarizability.** (a) Calculated force contrasts  $\Delta F$  for the single-atom metal tip as a function of tip-sample distance  $z$ . The blue curve is only the electrostatic force contrast, the curve consisting of red circles is with additional tip polarization. (b) Zoom into the  $z$  region marked by the gray rectangle in (a). Evidently, polarization can be neglected in the calculation for tip-sample distances reached in the experiment. Panel (a) adapted from Ref. [132].

$p_{\text{ind}}$  in a vertical electric field  $E$  is given as

$$p_{\text{ind}} = \alpha \epsilon_0 E, \quad (4.38)$$

where  $\alpha$  is the atomic polarizability. The vertical force experienced by this induced dipole in the electric field  $E$  is

$$F_{\text{ind}} = p_{\text{ind}} \frac{\partial E}{\partial z} = \alpha \epsilon_0 E \frac{\partial E}{\partial z}. \quad (4.39)$$

Since both  $E$  and  $\partial E/\partial z$  decay exponentially with distance,  $F_{\text{ind}}$  decays twice as fast as the electric field and thus the electrostatic force between tip and sample as calculated above [74]. In good approximation  $F_{\text{ind}}$  can therefore be modeled by taking into account only the front-most apex atom. As the tip was prepared on a Cu surface, it is most-likely terminated by a Cu atom [29]. Hence, the atomic polarizability of Cu,  $\alpha_{\text{Cu}} = 6.1 \text{ \AA}^3$ , has been used to calculate  $F_{\text{ind}}$  [62, 162].

Figure 4.10(a) shows the calculated force contrasts  $\Delta F$  as a function of tip-sample distance  $z$  for the metal tip taking into account only the electrostatic force ( $\Delta F_{\text{es}}$ , blue), as well as the contrast with the additional force contribution due to tip polarization ( $\Delta F_{\text{es}} + \Delta F_{\text{ind}}$ , red circles) plotted on a logarithmic scale. Evidently, including polarization does not significantly alter the exponential decay of the force contrast.

## 4 High-precision AFM measurements on CaF<sub>2</sub>(111) with an atomically-characterized metal tip

---

To highlight the slight differences between both curves, Fig. 4.10(b) shows a zoom into the  $z$  region marked by the gray rectangle in Fig. 4.10(a) on a linear scale. At the smallest tip-sample distance reached in the experiment of  $z = 335$  pm the difference between both curves is  $\Delta F_{\text{ind}} = 0.23$  pN, which is only 0.76 % of the electrostatic force contrast  $\Delta F_{\text{es}} = 30.66$  pN. With increasing  $z$  the relative contribution of  $\Delta F_{\text{ind}}$  decreases even further as  $\Delta F_{\text{ind}}$  decays twice as fast as  $\Delta F_{\text{es}}$  [74]. Consequently, polarization of the tip apex in the sample's electric field can be neglected in the calculation for all tip-sample distances reached in the experiment.

Additionally, strong tip-sample interactions could potentially induce relaxations of either the surface or the tip which would result in a deviation from the electrostatic calculation. This has been a major problem in previous AFM studies of bulk ionic crystals, where sample relaxations greater than 100 pm were observed that even lead to an inversion of the atomic-scale AFM contrast [14, 15]. In order to estimate a possible influence of tip-induced relaxations of sample atoms, in particular of the F<sup>-</sup><sub>top</sub> ions, the sample stiffness has been determined via the interaction potential  $V_{\text{Ca-F}}$  between a F<sup>-</sup> and a Ca<sup>2+</sup> ion, which at a distance  $r$  is given by [163, 164]

$$V_{\text{Ca-F}}(r) = A'e^{-r/\rho} - \frac{q_{\text{Ca}}q_{\text{F}}}{4\pi\epsilon_0 r}, \quad (4.40)$$

where the parameters  $A' = 943.569$  eV and  $\rho = 33.2$  pm were taken from Ref. [164], and  $q_{\text{Ca}} = +1.730e$  and  $q_{\text{F}} = -0.865e$  are the ionic charges used in the electrostatic calculation. From eq. (4.40) an equilibrium bond distance  $\sigma = 212$  pm between the F<sup>-</sup> and Ca<sup>2+</sup> ions is obtained. Evaluating the second derivative of eq. (4.40) with respect to  $r$  at the equilibrium distance  $\sigma$  determines the bond stiffness of  $k_{\text{Ca-F}} = 159$  N/m.

In CaF<sub>2</sub>(111), the surface F<sup>-</sup> ions bind to three Ca<sup>2+</sup> ions, where the horizontal angles between the bonds are 120° and the vertical angle between the  $xy$  plane and the bond is about  $\theta = 19.5^\circ$  as illustrated in Fig. 4.11(a). Hence, a vertical force  $F_z$  acting on a surface F<sup>-</sup> ion will not cause a lateral deflection but only a vertical relaxation. As sketched in Fig. 4.11(a),  $F_z$  can be separated into three components  $F'$  that are directed along the three springs representing the interaction between the surface F<sup>-</sup> ion and the three Ca<sup>2+</sup> ions and have a  $z$ -magnitude of  $1/3 F_z$ . The stretch  $\Delta l$  of one spring is then calculated as

$$\Delta l = \frac{F'}{k_{\text{Ca-F}}} = \frac{F_z}{3 \sin \theta k_{\text{Ca-F}}}. \quad (4.41)$$

The projection of  $\Delta l$  on the  $z$  axis gives the contribution to the vertical relaxation

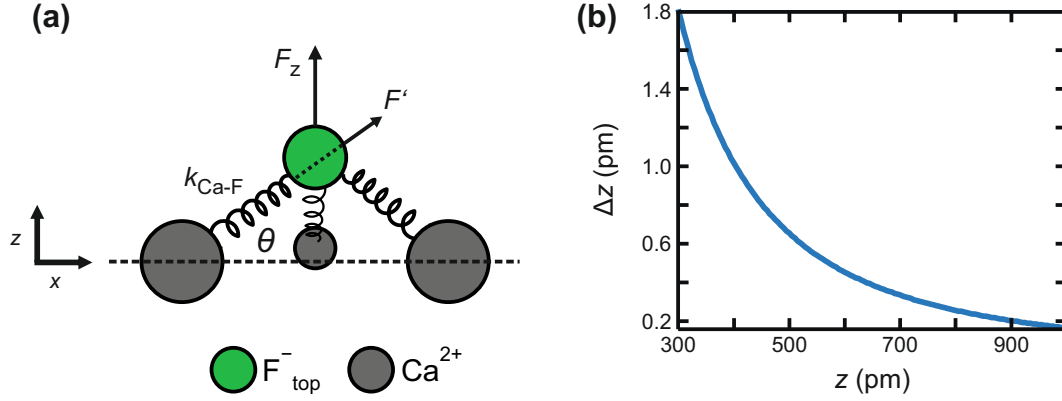


**Figure 4.11.: Estimation of tip-induced relaxation of surface  $F^-$  ions.** (a) Schematic of the model used to calculate the relaxation of the surface  $F^-$  ions. A vertical force  $F_z$  pulls on the bonds between the  $Ca^{2+}$  and  $F^-$  ions that have a stiffness of  $k_{Ca-F} = 159 \text{ N/m}$ . (b) Relaxation of a surface  $F^-$  ion  $\Delta z$  as a function of tip-sample distance  $z$  in the electric field of the tip apex. At  $z = 335 \text{ pm}$ , the relaxation is only  $\Delta z = 1.5 \text{ pm}$ . Note that a positive  $\Delta z$  is defined as a relaxation towards the tip. Figure adapted from Ref. [132].

of one spring as

$$\Delta z_1 = \Delta l \sin \theta = \frac{F_z}{3 k_{Ca-F}}, \quad (4.42)$$

yielding a total relaxation of

$$\Delta z = 3 \Delta z_1 = \frac{F_z}{k_{Ca-F}}. \quad (4.43)$$

Here, a positive  $\Delta z$  is defined as a relaxation in positive  $z$  direction, i.e. towards the tip.  $F_z$  is the force experienced by the  $F^-$  ion in the electric field of the metal tip and can therefore be described by

$$F_z(z) = q_F \frac{0.13 e}{4\pi\epsilon_0 z^2}, \quad (4.44)$$

where  $z$  is the tip-sample distance. In Fig. 4.11(b), the tip-induced relaxation  $\Delta z$  of a surface  $F^-$  ion as obtained by eqs. (4.43) and (4.44) is plotted as a function of  $z$ . At  $z = 335 \text{ pm}$  which corresponds to the closest tip-sample approach in the experiment, the relaxation amounts to only  $\Delta z = 1.5 \text{ pm}$  and will therefore only have a minor influence on the measured contrast.

### 4.4. Discussion

This chapter presented high-precision AFM measurements of the CaF<sub>2</sub>(111) surface in a deep non-contact regime, i.e. at tip-sample distances where the atomic force contrast is in the femtonewton regime. Due to the non-invasive imaging of the surface at these tip-sample distances a polarization of the tip apex in the electric field of the sample or tip-induced sample relaxations could be excluded. Hence, the experimental data could be reproduced by an electrostatic calculation where both the tip and the surface atoms are represented by static point charges. This showed that short-range electrostatic tip-sample interactions dominate the interaction between a single-atom metal tip and an ionic crystal surface. The AFM contrast was found to decay exponentially with tip-sample distance and the decay length matched the theoretically predicted decay length of the sample's electric field.

The experiments were performed with an atomically-characterized metal tip, which made the structural and chemical composition of the tip apex experimentally accessible. With this information the theoretical description of the tip could be refined, increasing the accuracy of an electrostatic calculation to reproduce experimentally observed asymmetries in the AFM images. This showcases how the interpretation of experimental AFM data benefits from the precise characterization of the tip apex at the atomic level. By experimentally ensuring the structural stability of the tip in the experiment the theoretical description of the system can be confined to only one tip model increasing the effectiveness of calculations to reproduce experimental AFM data.

The CaF<sub>2</sub>(111) surface has been chosen as a reference sample, because it presents an ionic crystal surface that lacks charge inversion symmetry, which had therefore been studied by AFM previously to identify the tip apex polarity. As shown in this chapter, the AFM contrast measured on this surface originates entirely in short-range electrostatic tip-sample interactions when probing the surface with a single-atom metal tip. Because of the reactivity of single-atom metal tips it is not possible to image the surface also in a repulsive imaging regime without risking irreversible tip changes. As described in section 3.3, terminating a single-atom metal tip with a CO molecule effectively passivates the tip apex and enables stable imaging of adsorbates and surfaces also at tip-sample distances where the AFM contrast is dominated by Pauli repulsion. Building upon the findings in this chapter, the imaging mechanisms of CO tips on ionic crystal surfaces are studied on the CaF<sub>2</sub>(111) surface in chapter 5.

# 5. Quantifying the evolution of atomic interaction of a CO-terminated tip with a complex ionic crystal surface

*Most of the work presented in this chapter has been published in Scientific Reports [139].<sup>1</sup> Parts of the text, figures and interpretations are identical to the publication. The author performed all experiments and carried out the complete data analysis with support from the co-authors of Ref. [139]. The accompanying calculations with the probe particle model were provided by Prokop Hapala from the Czech Academy of Sciences in Prague, who co-authored the publication, and analyzed in detail by the author of this thesis. Initial experimental results are presented in the author's Master thesis [85].*

The previous chapter reported on AFM measurements on the ionic  $\text{CaF}_2(111)$  surface with a single-atom metal tip. It was found that the atomic-scale contrast is entirely described by short-range electrostatic interactions at all experimentally accessed tip-sample distances. Due to the reactivity of the tip apex it was not possible to stably record images in a repulsive interaction regime at closer tip-sample distances. Functionalizing a metal tip apex with a single CO molecule effectively passivates the tip and enables imaging also at small tip-sample distances where repulsive forces start to dominate the interaction. In 2009, Gross *et al.* showed that this drastically increases the spatial resolution in AFM experiments opening the possibility to resolve the internal structure of simple organic molecules in real space [33]. Since then CO-terminated tips have been widely applied in AFM experiments to study organic molecules [16, 121, 122, 125, 165–167] and various types of surfaces and adsorbates with atomic resolution [32, 35, 36, 123, 126, 127].

---

<sup>1</sup>A. Liebig, P. Hapala, A. J. Weymouth and F. J. Giessibl, *Quantifying the evolution of atomic interaction of a complex surface with a functionalized atomic force microscopy tip*, Sci. Rep. **10**, 14104 (2020).

## 5 Quantifying the evolution of atomic interaction of a CO-terminated tip with a complex ionic crystal surface

---

The interaction of a CO tip with a sample surface is composed of different physical mechanisms, including van der Waals attraction and Pauli repulsion, which can be described by a Lennard-Jones potential, and electrostatic interaction between the complex electric field of the CO tip and the sample electron density. Recently, Huber *et al.* discovered an additional transition from a physisorbed to a chemisorbed interaction state in the interaction of CO tips with single iron adatoms adsorbed on a copper surface [25]. While the tip-sample interaction is dominated by different mechanisms at different tip-sample distances, interpretation of AFM images obtained with CO tips is additionally complicated by the lateral deflection of the CO at the tip apex if lateral forces act between tip and sample. This can lead to image distortions and an elongated appearance of atomic-scale features in AFM images [18, 166, 168].

The electrostatic tip-sample interaction is particularly important when probing the surface of an ionic crystal and the complex electric field at the CO tip apex needs to be considered in this case. Ellner *et al.* considered AFM images of Cl vacancies in NaCl thin films with a CO tips and showed that for such a charged feature the interaction with the strong background metal tip dipole dominates the overall electrostatic tip-sample interaction [35], similarly to the case when imaging the atomic lattice of hexagonal boron nitride [36]. On the contrary, the strongly spatially localized negative charge density at the tip apex is relevant when imaging the flat NaCl lattice [35, 137]. As these works focused on the study of atomically-flat NaCl films a potential effect of sample corrugation on the bending mechanism of CO tips has not been discussed. As described in chapter 4, the complex interplay of ionic charges and different atomic heights makes the CaF<sub>2</sub>(111) surface an ideal model surface to study the contribution of different physical mechanisms to the total tip-sample interaction.

This chapter presents a quantitative study of the atomic-scale AFM contrast formation on the corrugated CaF<sub>2</sub>(111) surface when probed with CO-terminated tips. First, the evolution of the atomic contrast in experimental  $\Delta f$  images is discussed (section 5.1). Second, the *probe particle model* is introduced, which is a mechanical model to simulate AFM images with CO-functionalized tips (section 5.2). The experimental images can be reproduced with this model at all tip-sample distances, which enables the characterization of the complete atomic-scale contrast formation on CaF<sub>2</sub>(111) with CO tips. Finally, in section 5.3 the electrostatic imaging regime is analyzed in more detail by comparing the experimental data recorded with the CO tip to the electrostatic point-charge calculation that was introduced already in section 4.2.

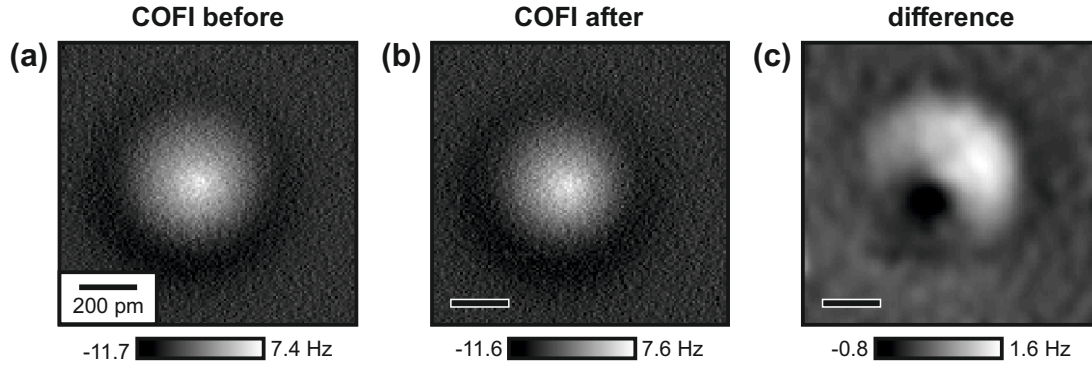


**Figure 5.1.:** COFI images recorded of the CO tip before and after the measurement on  $\text{CaF}_2(111)$ . (a) COFI image recorded of the CO-terminated tip before the measurement on  $\text{CaF}_2(111)$ . (b) COFI image recorded after the measurement on  $\text{CaF}_2(111)$ . The images were recorded 70 pm further away from the STM setpoint ( $V_b = -10$  mV,  $\langle I \rangle = -100$  pA) on the bare Cu(111) surface. (c) Difference image after subtracting (b) from (a) and subsequent Gaussian low-pass filtering. The difference image shows only weak contrast compared to the COFI images, proving that the tip did not change during the experiment. Slight differences can be attributed to a small offset in the imaging height, compare Fig 4.3. All scale bars are 200 pm long. Figure adapted from Ref. [139].

## 5.1. Evolution of atomic contrast in experimental constant-height images

The experiments presented in this chapter were performed with the same sensor and on the same  $\text{CaF}_2(111)$  sample as used in chapter 4. Hence, the measured images presented in both chapters are directly comparable to each other as the orientation of the  $\text{CaF}_2$  single crystal may not have changed between both measurements. CO-terminated tips were characterized and prepared on a Cu(111) surface as described in section 3.3. The CO tips were characterized with the COFI method before and after the measurement on  $\text{CaF}_2(111)$ , i.e. in a similar measurement cycle as the metal tip used in the experiments presented in chapter 4 and Ref. [31]. Figure 5.1(a),(b) shows COFI images of the CO tip recorded before and after the measurement on  $\text{CaF}_2(111)$ , respectively. At small tip-sample distances the CO-CO interaction results in a bright, circularly-symmetric feature in constant-height  $\Delta f$  images [16, 169]. A detailed analysis of the AFM contrast in COFI images of CO-terminated tips can be found in chapter 6. To assert that the two COFI images are equal they are subtracted from each other. The resulting difference image is depicted in Fig. 5.1(c). The difference image shows only weak contrast compared to the two COFI images, which confirms that the atomic composition of the tip apex did not change during

## 5 Quantifying the evolution of atomic interaction of a CO-terminated tip with a complex ionic crystal surface

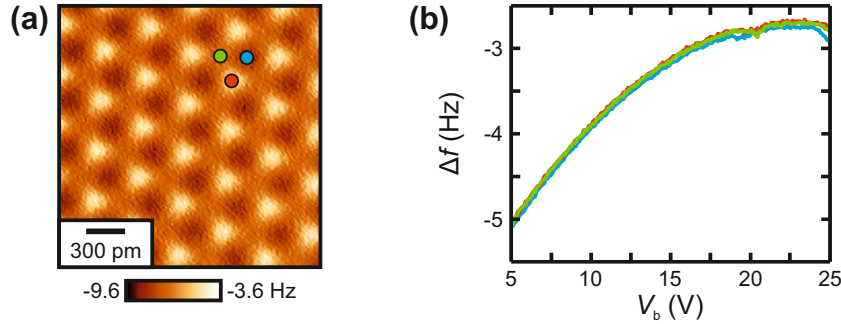


**Figure 5.2.: Determination of the contact potential difference.** (a) Constant-height frequency shift image of the  $\text{CaF}_2(111)$  surface recorded with the CO-terminated tip. The image has been recorded 50 pm closer from the AFM setpoint. Setpoint on the attractive site:  $A = 50$  pm,  $V_b = 22.5$  V,  $\Delta f = -5.5$  Hz. (b)  $\Delta f(V_b)$  curves (Kelvin parabolas) recorded on the three high-symmetry sites marked in the constant-height image. The apex voltage  $V_{\text{CPD}} = 22.5$  V was used as the imaging voltage to minimize the long-range electrostatic tip-sample interaction. Panel (b) adapted from Ref. [139].

the measurement on  $\text{CaF}_2(111)$ . The slight contrast visible in Fig. 5.1(c) can be attributed to a small offset in the imaging height as already discussed in context of Fig. 4.3.

After the tip was prepared and characterized on  $\text{Cu}(111)$  the sample was replaced by the  $\text{CaF}_2(111)$  sample and the CO tip was approached to the surface. Figure 5.2(a) shows an experimental constant-height frequency shift image recorded of the  $\text{CaF}_2(111)$  surface after the CO tip was approached to a tip-sample distance regime where atomic resolution was first visible in the constant-height images. Analogous to the constant-height images recorded with the single-atom metal tip that are presented in chapter 4, the image presents three high-symmetry sites that correspond to the atoms of the surface triple layer of  $\text{CaF}_2(111)$ . To minimize the long-range electrostatic interaction (see section 2.2.3), Kelvin parabolas  $\Delta f(V_b)$  have been measured on the three high-symmetry sites and the average apex voltage  $V_{\text{CPD}}$  has been used as the imaging voltage  $V_b$  as described in section 4.3 for the experiment on  $\text{CaF}_2(111)$  with the single-atom metal tip. The Kelvin parabolas measured on the three sites marked in Fig. 5.2(a) are presented in Fig. 5.2(b) resulting in a voltage of  $V_b = 22.5$  V. All experimental data measured on the  $\text{CaF}_2(111)$  sample shown in this chapter have been recorded with this bias voltage. While the measured value of  $V_{\text{CPD}} = 22.5$  V appears quite high at a first glance it should be noted that on bulk ionic crystals such CPD values are not unusual [140]. The contact potential difference depends on work function differences between tip and sample and the surface charge created during the cleave. The  $\text{CaF}_2(111)$  sample used in the experiments has a thickness of about  $d = 3$  mm. The surface charge density  $\sigma_{\text{surf}}$  creating an additional contact potential

## 5.1 Evolution of atomic contrast in experimental constant-height images

difference  $V_{\text{CPD}}$  of 22.5 V can be estimated by viewing tip and sample as a capacitor filled with  $\text{CaF}_2$  as a dielectric, which results in only

$$\sigma_{\text{surf}} = \epsilon_0 \epsilon_r \frac{V_{\text{CPD}}}{d} = 4.3 \times 10^{-7} \frac{\text{C}}{\text{m}^2} = 2.7 \times 10^{12} \frac{e}{\text{m}^2} = 2.7 \frac{e}{\mu\text{m}^2}, \quad (5.1)$$

where  $e$  denotes the elementary charge and  $\epsilon_r = 6.5$  is the dielectric constant of  $\text{CaF}_2$  at  $T = 4.4 \text{ K}$  [170, 171].

Figure 5.3 shows a series of constant-height  $\Delta f$  images recorded of the  $\text{CaF}_2(111)$  surface as a function of tip-sample distance with 25 pm distance decrements. The images are extracted from a three-dimensional data set  $\Delta f(x, y, z)$  with active drift compensation, as described in section 2.2.3 to ensure that the images were recorded of the same spot on the surface. The distance  $z_{\text{exp}} = 0 \text{ pm}$  is defined as the closest tip-sample approach in the experiment with the CO tip. At closer distances, an increased AFM dissipation signal was observed and the sample was not imaged at these distances to avoid damaging the CO tip apex. To reduce the influence of frequency measurement noise  $\delta f$  (see section 4.3.2) the images were acquired at a scan speed of  $v = 200 \text{ pm/s}$  resulting in a pixel rate of 12.8 px/s. Following eqs. (4.25), (4.32) and (4.30) and replacing the measurement bandwidth  $B$  with this pixel rate, the total frequency noise according to eq. (4.35) amounts to  $\delta f = 40 \text{ mHz}$ . Hence, an influence of frequency noise is visible only in the constant-height images at largest tip-sample separations where the total  $\Delta f$  contrast is less than 1 Hz [Fig. 5.3(a)–(d)].

Initially [Fig. 5.3(a)–(f)], the constant-height images present three high-symmetry sites that correspond to the atoms of the surface triple layer of  $\text{CaF}_2(111)$  in analogy to the images recorded with the single-atom metal tip in chapter 4. In this regime, the atomic  $\Delta f$  contrast increases monotonically upon approach. When the tip-sample distance is further reduced [Fig. 5.3(g)–(i)], a sharpening of features can be observed which has previously been attributed to CO bending in images recorded of organic molecules [18, 34]. By further decreasing the tip-sample distance, the contrast between the three sites starts to change drastically [Fig. 5.3(j),(k)] until the surface appears as a hexagonal arrangement of bright spheres in the image at closest approach [Fig. 5.3(l)]. Compared to the data recorded of the  $\text{CaF}_2(111)$  surface with the single-atom metal tip, where the short-range tip-sample interaction is governed entirely by electrostatics, the data recorded of  $\text{CaF}_2(111)$  with the CO tip shows a strong contrast variation. Apparently, the electrostatic point charge calculation introduced in chapter 4 cannot reproduce the experimental data over the complete tip-sample distance regime and additional influences of van der Waals attraction, Pauli repulsion and CO bending need to be considered.

## 5 Quantifying the evolution of atomic interaction of a CO-terminated tip with a complex ionic crystal surface

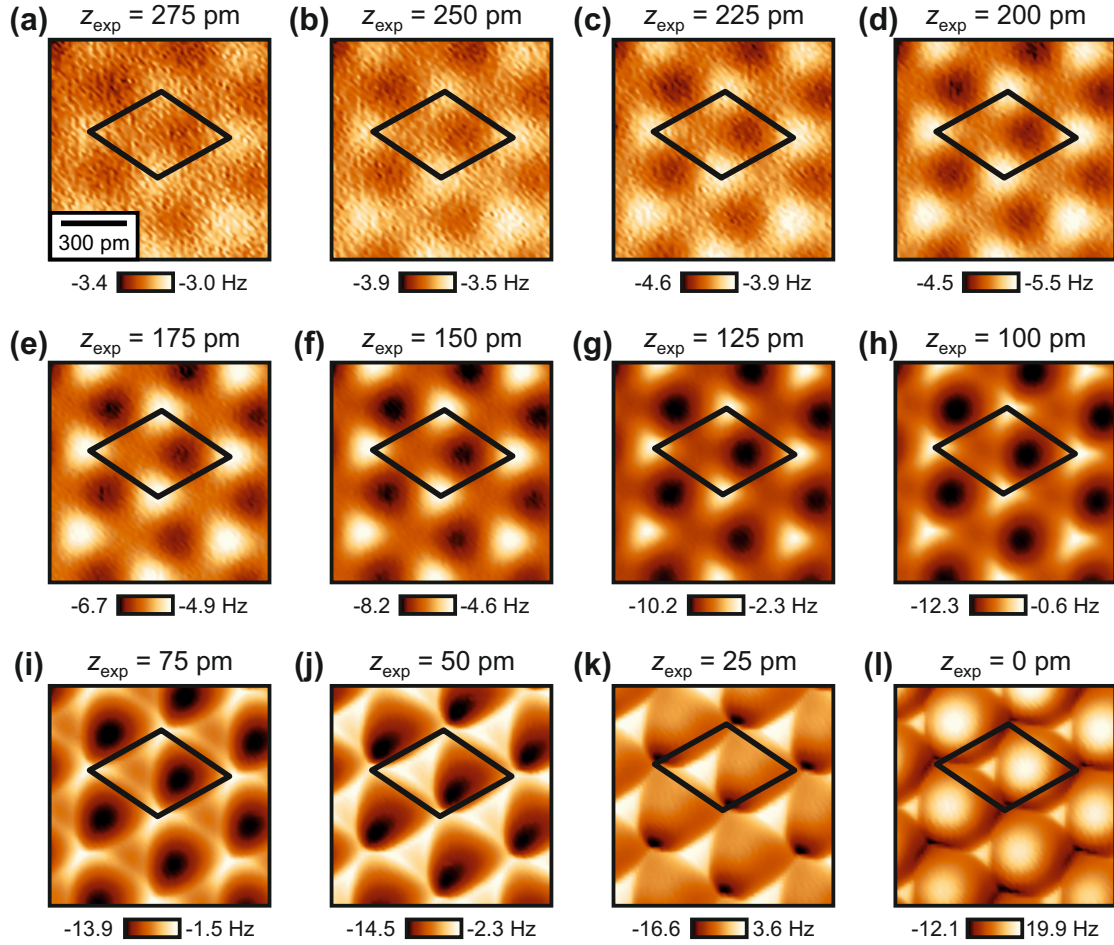


**Figure 5.3.: Distance-dependent experimental constant-height images.** Unprocessed experimental constant-height  $\Delta f$  images as a function of tip-sample distance recorded of the CaF<sub>2</sub>(111) surface with the CO tip.  $z_{\text{exp}} = 0$  pm is defined as the closest tip-sample approach in the experiment. All images have a size of 1 nm<sup>2</sup> and are recorded at a scan speed of  $v = 200$  pm/s. The unit cell defined in Fig. 4.1(b) is drawn in all images. Figure partly adapted from Ref. [139].

### 5.2. Probe particle model simulations

To understand the rich contrast features observed in the experimental constant-height images, AFM image simulations have been performed by Prokop Hapala with the *probe particle model* (PPM)<sup>2</sup> [22, 73], which is a mechanical model to calculate STM and AFM images with functionalized tips. The PPM considers the lateral deflection of a *probe particle* representing the tip apex due to the tip-sample interactions and is described in detail in Ref. [22]. In its original implementation the tip-sample interaction is calculated as a sum of pairwise Lennard-Jones potentials describing the interaction of the probe particle with each surface atom [22]. The bending of the

<sup>2</sup>The PPM can be downloaded at <https://github.com/ProkopHapala/ProbeParticleModel>.

AFM tip apex is then considered by vertically approaching the probe particle to the sample and allowing it to relax to its global energy minimum after each step. Since then, the PPM has been further developed to include also electrostatic tip-sample interactions [73, 172] and was extended to be able to calculate  $\Delta f$  images obtained by lateral force microscopy [173].

For the PPM simulations the relaxed atomic structure of the  $\text{CaF}_2(111)$  surface, its electrostatic potential and the electron density of both tip and sample are required. All these quantities were obtained by DFT using the *Vienna Ab initio Simulation Package* (VASP) [174] with default projector augmented wave (PAW) pseudopotentials [175] for Ca, F, C and O with a cutoff energy set to 400 eV. For the  $\text{CaF}_2(111)$  surface, Bloch wavefunctions of a  $2 \times 2$  unit cell with two layers containing 24 atoms were sampled using only the  $\Gamma$ -point. The ionic radii of the calcium and fluorine ions were determined by analyzing the sample electron density obtained from the DFT calculations taking an isosurface value of  $0.01 \text{ eV}/\text{\AA}^3$ . In this way, the Lennard-Jones radius of the calcium cation was modified with respect to the default parameter of  $2.78 \text{ \AA}$  [176] to  $1.70 \text{ \AA}$ , while the radius of the fluorine anion was consistent with the default value of  $1.75 \text{ \AA}$  [177]. A similar method has been previously used in Ref. [125] to estimate the ionic radius of a sodium cation hydrated by water on a NaCl surface, since in common classical force fields there are no good estimates of Lennard-Jones radii valid for ionic crystal surfaces.

The respective potentials and force fields were evaluated on a regular rectangular grid using the FFT approach described in Ref. [73]. The final force field stored on a rectangular grid was then used by the probe particle relaxation procedure with the lateral stiffness of the CO tip apex set to  $0.5 \text{ N/m}$ . Note that in Ref. [21] a lateral stiffness of  $0.24 \text{ N/m}$  has been determined for the CO tip. However, as stated by Neu *et al.* [168], the stiffness of the CO molecule depends on the underlying tip apex and a better agreement between experiment and theory was found for a lateral stiffness of  $0.5 \text{ N/m}$ . The resulting force was converted to frequency shift according to eq. (2.7) using an amplitude of  $A = 50 \text{ pm}$  as set in the experiment.

During the analysis of the experimental data presented in this chapter, two PPM approaches to calculate the tip-sample interaction, in particular the contribution from Pauli repulsion, have been conducted. In the first (section 5.2.1), the contributions from Pauli repulsion and electrostatic interaction that come from the DFT output are included overtop the attractive van der Waals component. In the second (section 5.2.2), the standard PPM method is used, where Pauli repulsion and van der Waals attraction are approximated by semi-empirical Lennard-Jones potentials. The electrostatic interaction is calculated as a convolution of the sample electrostatic

potential obtained from the DFT output and a quadrupole-like charge distribution modeling the CO tip.

### 5.2.1. Determining Pauli repulsion via the overlap of the electron densities of tip and sample

To get a quantitative comparison between experiment and theory, AFM image simulations have been performed with a modified version of the PPM. Instead of using standard Lennard-Jones potentials, the contribution of Pauli repulsion was obtained by calculating the overlap of the electron densities of tip and sample [72, 178] that were both calculated on a three-dimensional grid by DFT. The attractive van der Waals component was calculated with the modified ionic radii of the sample atoms and was added to the contribution of Pauli repulsion. Additionally, the electrostatic interaction is added via a convolution between the electrostatic sample potential and the tip's electron density that were obtained independently from the DFT calculations. In this way, the PPM calculation is closely related to the method developed by Ellner *et al.* [178], when the exponent in eq. (1) in Ref. [178] is set to  $\alpha = 1$ . Figure 5.4 shows the redistribution of the electron density of a CO molecule that was calculated with VASP to represent the CO tip apex in the experiment. Here, redistribution refers to the difference in electron density between the CO molecule after forming the chemical bond and two isolated carbon and oxygen atoms. Hence, a more positive value corresponds to a larger electron density (red areas): when the carbon and oxygen atoms form a covalent bond, the electron density between the two atoms increases leading to more positive values. The image in Fig. 5.4(a) presents a vertical cut through the data grid at  $y = 0 \text{ \AA}$  and the positions of the C and O atoms are marked black and red, respectively. To illustrate the rotational symmetry of the CO electron density, a three-dimensional representation is shown in Fig. 5.4(b).

The calculation of the CO electron density shows that a strongly spatially localized negative charge density is present in front of the O atom around  $z = -0.3 \text{ \AA} = -30 \text{ pm}$ . This localized negative charge density has been identified to dominate the electrostatic tip-sample interaction when probing ionic lattices with CO-terminated tips [35, 137]. On the contrary, the background metal tip dipole (see also chapter 4) dominates the electrostatic interaction when imaging an isolated charged feature on a surface such as Cl vacancies in a NaCl thin film with CO tips [35], similar to the case when imaging the atomic lattice of hexagonal boron nitride [36]. The CO electron densities shown in Fig. 5.4 were calculated without considering an influence of the background metal tip dipole, which can strongly alter the overall tip dipole depending

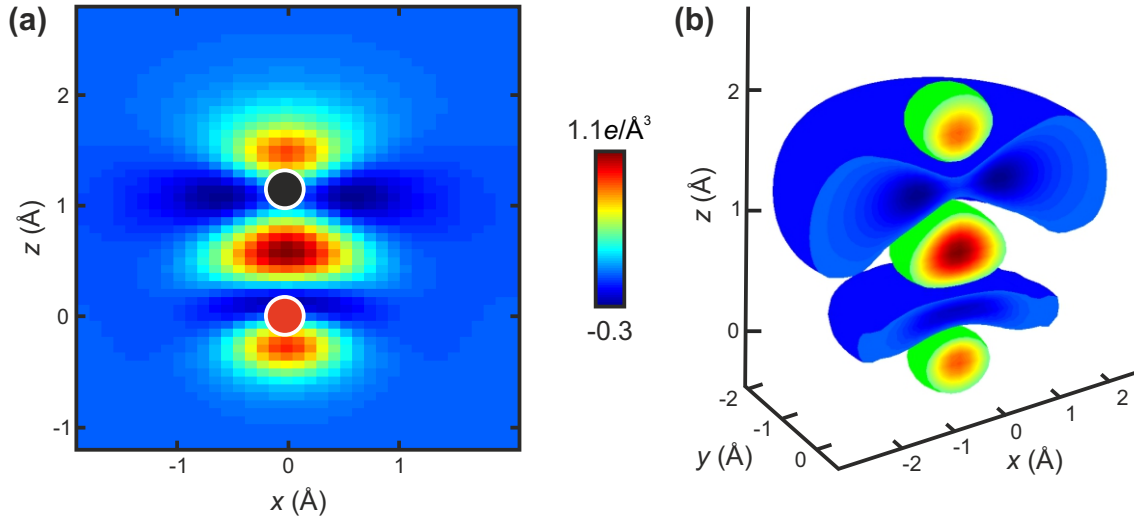


**Figure 5.4.: Calculated redistribution of electron density on a CO molecule.** (a) Vertical cut through the CO electron density data grid at  $y = 0 \text{ \AA}$ . The positions of the C and O atoms are marked black and red, respectively. (b) Three-dimensional representation of the CO electron density showing its rotational symmetry. The iso-surfaces were extracted for isosurface values of  $-0.02 e/\text{\AA}^3$  (blue) and  $0.3 e/\text{\AA}^3$  (green). Note that a more positive value corresponds to an increase in the electron density.

on the geometry of the metal slab [36]. However, as the defect-free  $\text{CaF}_2(111)$  lattice has been probed with CO tips in this chapter, only the contribution of the CO molecule at the tip apex has been considered in the PPM calculation.

Figure 5.5 shows calculated constant-height  $\Delta f$  images obtained with the modified PPM as a function of tip-sample distance over a similar range as the experimental images shown in Fig. 5.3. The tip-sample distance  $z$  is defined as the vertical distance between the  $\text{F}_{\text{top}}^-$  and the tip apex oxygen nuclei. While the experimental images in Fig. 5.3 show continuous transitions as the distance is reduced in steps of  $\Delta z = 25 \text{ pm}$  from the deep non-contact regime to close contact where significant bending occurs, the calculated data are shown in heights so that the calculated images present an optimized match to the experimental images [e.g.  $\Delta z_{\text{exp}} = 25 \text{ pm}$  between Fig. 5.3(j) and (k) compared to  $\Delta z = 50 \text{ pm}$  between Fig. 5.5(j) and (k)]. For better comparison, the experimental and the calculated images are shown as a single figure in appendix A.3. The model reproduces the experimentally observed contrast patterns in good agreement. When approaching the surface the contrast first starts to increase [Fig. 5.5(a)–(f)] monotonically. By further approaching the surface [Fig. 5.5(g)–(i)] a sharpening of features is observed above the  $\text{F}_{\text{top}}^-$  ions that are imaged bright. At the smallest tip-sample distances, the strong contrast variations that are observed in the experiment [Fig. 5.3(j),(k)] are reproduced by the PPM [Fig. 5.5(j),(k)], in-

## 5 Quantifying the evolution of atomic interaction of a CO-terminated tip with a complex ionic crystal surface

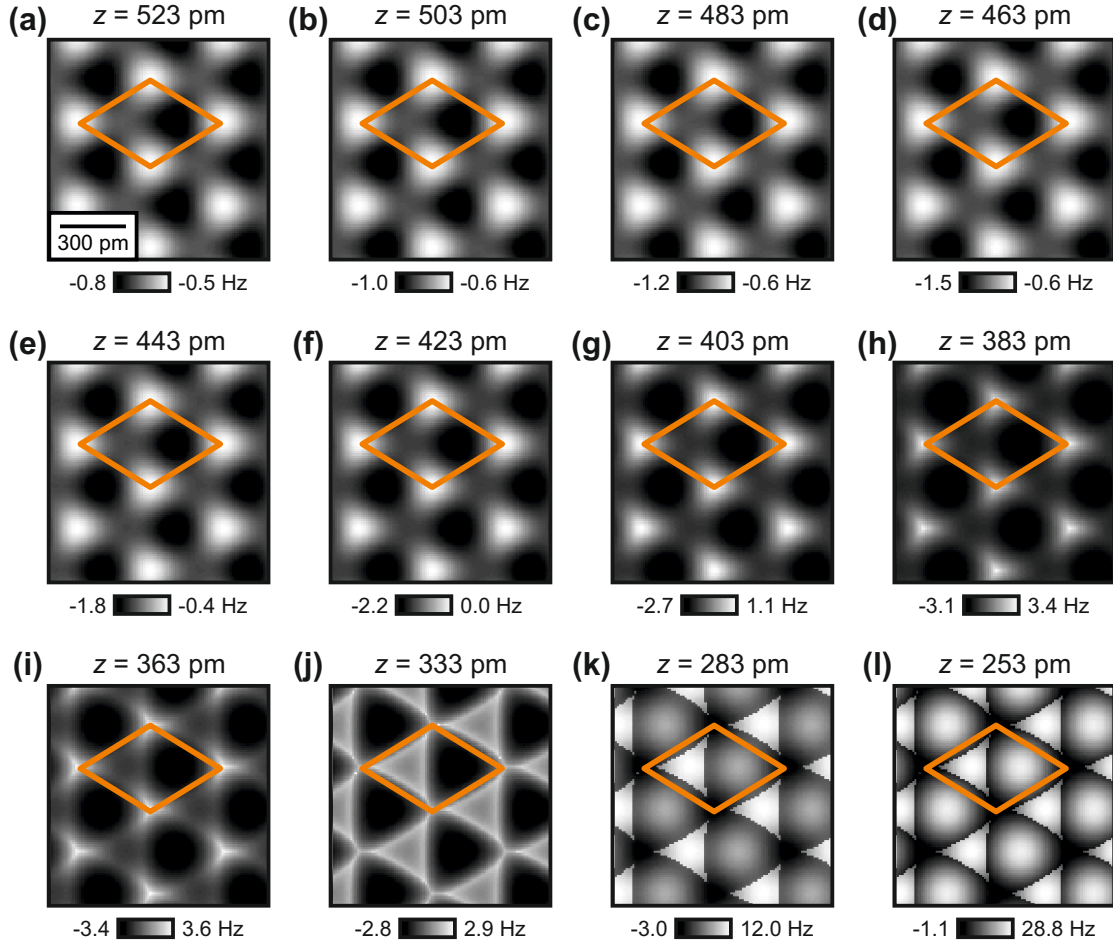


**Figure 5.5.:** Calculated constant-height images of  $\text{CaF}_2(111)$ . Constant-height  $\Delta f$  images of the  $\text{CaF}_2(111)$  surface calculated with the PPM code that calculates Pauli repulsion via the overlap of the electron densities of tip and sample over a similar  $z$  range as the experimental images shown in Fig. 5.3. The tip-sample distance  $z$  is defined as the vertical distance between the  $\text{F}_{\text{top}}^-$  and the tip apex oxygen nuclei. The unit cell defined in Fig. 4.1(b) is drawn in all images. Figure partly adapted from Ref. [139].

cluding the appearance of the surface as a hexagonal arrangement of bright spheres [Fig. 5.3(l) and Fig. 5.5(l)]. A slight difference between the experimental and the calculated images is the shrinking of the bright triangular features in the experimental constant-height images at closest tip-sample distances, located in the left halves of the unit cells in Fig. 5.3(j)–(l). This shrinking is visible in the simulation only at smaller tip-sample distances. Additional calculated images at smaller  $z$  values that show this shrinking are shown in appendix A.4. Note that the overall  $\Delta f$  values obtained from the PPM are offset to more positive values as compared to the experimental values. This can be attributed to the attractive offset that is added in the experiment due to the long-range van der Waals interaction which is not included in the simulation. Furthermore, the PPM calculation slightly underestimates the  $\Delta f$  contrast in the

experimental images. For example, while the experimental image in Fig. 5.3(j) shows a  $\Delta f$  contrast of 12.2 Hz, the corresponding calculated image shown in Fig. 5.5(j) has a  $\Delta f$  contrast of only 5.7 Hz. A possible explanation for this discrepancy is the fact that in the DFT calculation an isolated CO molecule was considered, which is a simplification of the experimental conditions with the CO adsorbed on a metal tip apex. This could potentially affect the electron density of the CO molecule shown in Fig. 5.4, which was used in the simulation to calculate both the contribution from Pauli repulsion as well as the electrostatic interaction.

To determine which tip-sample interaction dominates the AFM contrast, the individual contributions to the overall tip-sample force can be decomposed from the PPM data. Figure 5.6 shows the contributions of electrostatic interaction, van der Waals attraction and Pauli repulsion to the total force [Fig. 5.6(a)–(c)] at a tip-sample distance of  $z = 451$  pm, i.e. at a tip-sample distance regime where the  $\Delta f$  contrast in the simulated constant-height images increases monotonically and no sharpening is observed [Fig. 5.5(a)–(f)]. The total force shown in Fig. 5.6(d) is obtained by summing the three individual contributions and closely resembles the pattern that is obtained by short-range electrostatics. Above the atoms of the surface  $F^-$ -layer the electrostatic repulsion between the ions and the negative charge density in front of the CO tip apex leads to a decrease of the overall attractive tip-sample interaction.

The strong height differences between the atoms in the surface triple layer are key to understanding why the AFM contrast in this regime is explained solely by short-range electrostatics. The individual contributions of van der Waals attraction, Pauli repulsion and electrostatic interaction as a function of tip-sample distance are shown in Fig. 5.6(e),(f). The force contributions from atomic van der Waals attraction (green) and Pauli repulsion (blue) decay faster than the electrostatic interaction (red). Therefore, in this tip-sample distance regime, a sizable contribution to the overall interaction due to these two components is obtained only above the atoms in the surface  $F^-$ -layer that are approximately 79 pm closer to the tip than the  $Ca^{2+}$  atoms in the second layer [Fig. 5.6(b),(c)]. Additionally, the opposite nature of the two forces leads to a cancellation effect: the attractive van der Waals interaction is partly compensated by Pauli repulsion, which further contributes to the fact that short-range electrostatics dominate the atomic-scale AFM contrast at large tip-sample separations. Note that the decomposition of the individual force components was performed for a rigid probe particle, because CO bending has only a negligible influence on the measured contrast at this tip-sample distance regime.

If the tip-sample distance is decreased, the lateral component in the tip-sample force is increased. Therefore, the probe particle starts to deflect laterally, which results in

## 5 Quantifying the evolution of atomic interaction of a CO-terminated tip with a complex ionic crystal surface

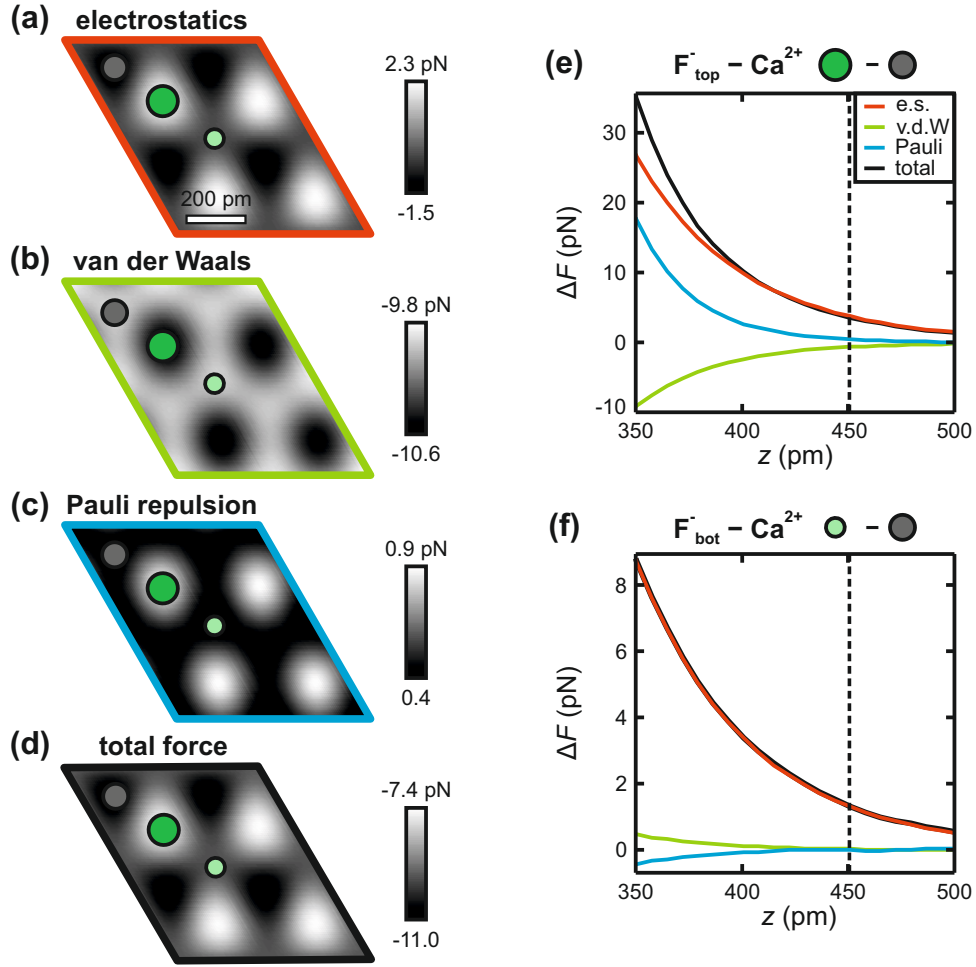


**Figure 5.6.:** Comparison of force contributions obtained from the PPM in the electrostatic imaging regime. (a)–(c) Interaction decomposed images of a  $\text{CaF}_2(111)$  supercell at a tip-sample distance of  $z = 451$  pm, and (d) the total force obtained by summing all three contributions obtained with the PPM. (e), (f) Individual contributions to the atomic force contrasts  $\Delta F$  as a function of tip-sample distance  $z$ . The dashed line marks the tip-sample distance at which the images in (a)–(d) were extracted. Colors match the frames in (a)–(d). Figure adapted from Ref. [139].

the already discussed sharpening of the atomic features in the constant-height images [Fig. 5.5(g)–(i)] as also seen in the experimental images shown in Fig. 5.3(g)–(i). Upon further approach, the probe particle model [Fig. 5.5(j)–(l)] correctly reproduces the experimentally observed contrast patterns [Fig. 5.3(j)–(l)]. To determine the dominant interaction at this tip-sample distance regime the individual force components are decomposed from the PPM data. Figure 5.7 shows the individual force components [5.7(a)–(c)] that add to the total force [5.7(d)] at a tip-sample distance of  $z = 272$  pm, revealing that Pauli repulsion is the dominant contribution to the total AFM contrast with strong repulsive features above the surface  $F_{\text{top}}^-$  ions [Fig. 5.7(c)]. This is further illustrated by the individual force contrast versus distance plots shown

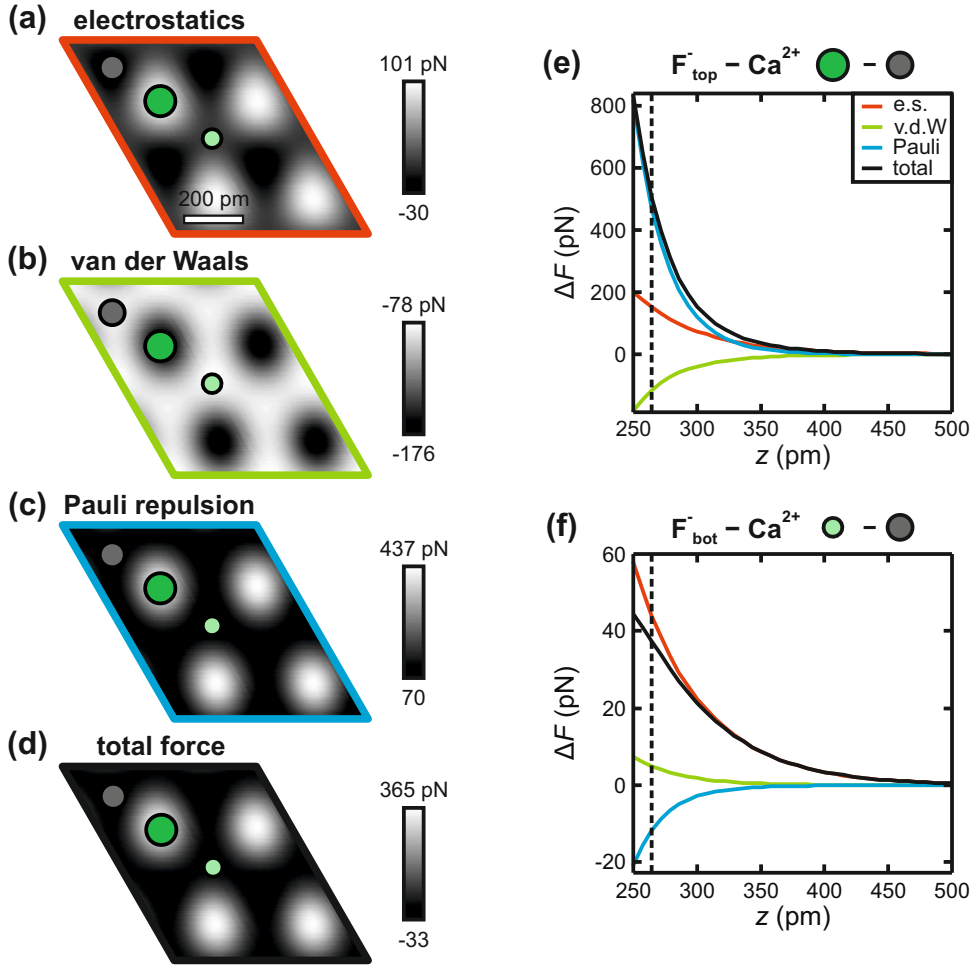


**Figure 5.7.:** Comparison of force contributions obtained from the PPM at closest approach. (a)–(c) Interaction decomposed images of a CaF<sub>2</sub>(111) supercell at a tip-sample distance of  $z = 272$  pm, and (d) the total force obtained by summing all three contributions obtained with the PPM. (e), (f) Individual contributions to the atomic force contrasts  $\Delta F$  as a function of tip-sample distance  $z$ . The dashed line marks the tip-sample distance at which the images in (a)–(d) were extracted. Colors match the frames in (a)–(d). Figure adapted from Ref. [139].

in Fig. 5.7(e),(f). The contrast caused by Pauli repulsion above the  $F_{\text{top}}^-$  ions [blue curve in Fig. 5.7(e)] is largest in magnitude.

Having addressed the relevant physics at this tip-sample distance regime, the influence of CO bending on the AFM contrast can be discussed. In the image recorded at the smallest tip-sample separation shown in Fig. 5.3(l), the AFM contrast pattern resembles a hexagonal arrangement of bright spheres. This pattern would not be obtained by simply adding the three interactions obtained for a rigid probe particle [Fig. 5.7(a)–(c)], which would yield a strongly repulsive feature above the surface  $F^-$  atoms as shown in Fig. 5.7(d). If the probe particle is allowed to relax, it will slide around the exposed atoms of the surface  $F^-$  layer, which completely alters the pre-

## 5 Quantifying the evolution of atomic interaction of a CO-terminated tip with a complex ionic crystal surface

---

dicted AFM contrast. This mechanism leads to the above-mentioned appearance of bright, repulsive sphere-like features at the positions of the  $\text{Ca}^{2+}$  atoms and triangular features at the positions of the  $\text{F}_{\text{bot}}^-$  ions in the AFM images. Above the surface  $\text{F}_{\text{top}}^-$  ions CO bending causes the occurrence of sharp attractive ridges [see Fig. 5.3(1) and Fig. 5.5(1), the corners of the unit cell are at the  $\text{F}_{\text{top}}^-$  positions].

Based on this  $z$ -dependent analysis of the decomposed interactions the AFM contrast formation of CO tips on the  $\text{CaF}_2(111)$  surface can now be discussed as a function of tip-sample distance. At large tip-sample distances, short-range electrostatics dominate the AFM contrast, while Pauli repulsion and van der Waals attraction compensate each other. If the tip-sample distance is decreased to about  $z = 300$  pm, Pauli repulsion starts to overcome the electrostatic interaction. The strongest repulsion is observed above the protruding  $\text{F}_{\text{top}}^-$  ions for a rigid probe particle. At this point, CO bending has additional influence on the images, as this leads first to a sharpening of features and then, at even closer distances, to a contrast inversion [18]. The observation of a transition from an electrostatic imaging regime to a regime where Pauli repulsion dominates the AFM contrast is in agreement with the findings of Ellner *et al.* [35]. This suggests that the interaction of a CO tip with an ionic crystal is generally dominated by short-range electrostatics at larger tip-sample distances where the negative charge density at the tip apex is responsible for the atomic contrast and Pauli repulsion at close tip-sample distances.

### 5.2.2. Probe particle model simulations using Lennard-Jones potentials to describe Pauli repulsion

In the PPM calculations presented in section 5.2.1 a modified version of the PPM was used, where Pauli repulsion was calculated using the overlap of the electron densities of tip and sample. For comparison, additional calculations using the standard PPM method that is based on Lennard-Jones potentials as formulated in Ref. [22] to describe van der Waals attraction and Pauli repulsion were performed. As described above, the ionic radii of the sample ions were modified from the default values by analyzing the DFT-obtained sample electron density. The electrostatic interaction is added as a convolution of the sample electrostatic potential obtained from density functional theory and a quadrupole-type charge distribution modeling the CO tip. The tip's charge distribution was set to the  $dz^2$ -orbital as defined in Ref. [73, 167], normalized to a quadrupole of  $-0.1 e\text{\AA}^2$ . A quadrupole-like charge distribution representing the CO tip has been previously employed by Schulz *et al.* in Ref. [36] to simulate images of a chlorine vacancy in a flat NaCl lattice. The calculations in

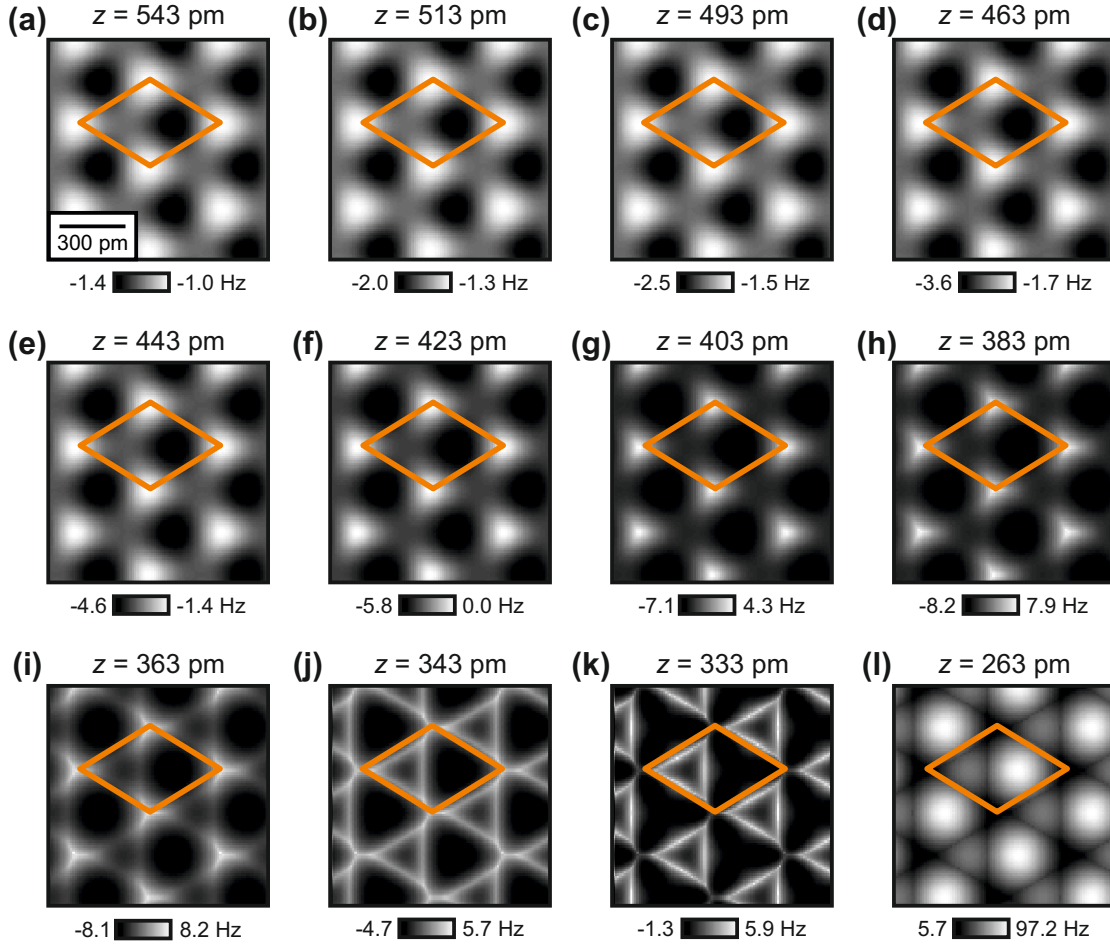


**Figure 5.8.:** Calculated constant-height images of  $\text{CaF}_2(111)$  using the standard PPM approach. Constant-height  $\Delta f$  images of the  $\text{CaF}_2(111)$  surface calculated with the PPM using the standard choice of Lennard-Jones potentials to describe van der Waals attraction and Pauli repulsion as a function of tip-sample distance  $z$ . The unit cell defined in Fig. 4.1(b) is drawn in all images. Figure partly adapted from Ref. [139].

Ref. [36] are in good agreement to the work of Ellner *et al.* on the same sample system [35]. Hence, the calculations in this section should be directly comparable to the calculations presented in section 5.2.1, where the DFT-calculated electron charge redistribution at the CO tip apex is used to determine the electrostatic tip-sample interaction.

Figure 5.8 shows constant-height  $\Delta f$  images of the  $\text{CaF}_2(111)$  calculated with this standard PPM approach over a similar  $z$  range as the experimental and calculated images in Figs. 5.3 and 5.5. For better comparison, both series of calculated images are shown in one figure in appendix A.5. Both simulations give similar results that reproduce the experimental images well especially at larger tip-sample distances. Strong discrepancies between both simulations occur only at smallest tip-sample dis-

## 5 Quantifying the evolution of atomic interaction of a CO-terminated tip with a complex ionic crystal surface

---

tances: in the density overlap simulation [Fig. 5.5(j),(k)] the experimentally observed appearance of a bright triangular feature in the left half of the unit cell [Fig. 5.3(j),(k)] is nicely reproduced. In contrast, in the images created from the simulation using Lennard-Jones potentials [Fig. 5.8(j),(k)] these features appear with a dark center and bright ridges instead of a triangular feature with a bright center. On the contrary, the shrinking of this bright triangle observed in the experimental data at the smallest tip-sample distance [Fig. 5.3(l)] is better reproduced by the standard PPM approach [Fig. 5.8(l)] as compared to the density overlap simulation [Fig. 5.5(l)], where this shrinking is observed at slightly smaller tip-sample separations, as shown in appendix A.4. Note that the overall  $\Delta f$  contrast is slightly overestimated in the simulation incorporating Lennard-Jones potentials as compared to the experimental contrast. A potential reason for this is the simplification made in the second simulation in order to estimate the contribution from Pauli repulsion, which is described by the empirical  $1/z^{12}$  law, see eq. (2.13). From the large positive  $\Delta f$  values in the closest simulated image shown in Fig. 5.8(l) it follows that the Lennard-Jones potentials used here overestimate Pauli repulsion. It can be therefore concluded that the density overlap simulation provides a more realistic description of the tip-sample interaction compared to the original PPM approach based on Lennard-Jones potentials. Nonetheless, also the latter can qualitatively reproduce the experimental AFM images.

### 5.3. Electrostatic imaging regime

By comparing the experimental data to the PPM calculations all physical mechanisms that are relevant in the contrast formation are identified. At small tip-sample distances below  $z = 300$  pm Pauli repulsion dominates the contrast and this contribution has been calculated using two different approaches in the PPM, as described in detail in section 5.2. This section discusses the electrostatic imaging regime in more detail, i.e. the AFM contrast for tip-sample distances larger than  $z = 400$  pm, where the electrostatic tip-sample interaction dominates the AFM contrast (see Fig. 5.6). In the PPM calculations the electrostatic tip-sample interaction is included by a convolution of the electrostatic potential of the sample and the tip's electron density. Previous works incorporating electrostatic tip-sample interactions successfully used a single negative point charge to represent the CO tip apex [137, 172]. This section compares the experimental data recorded of  $\text{CaF}_2(111)$  with the CO tip to the electrostatic point charge calculation that is presented in section 4.2 in context of experimental data recorded of the same surface with a single-atom metal tip. While

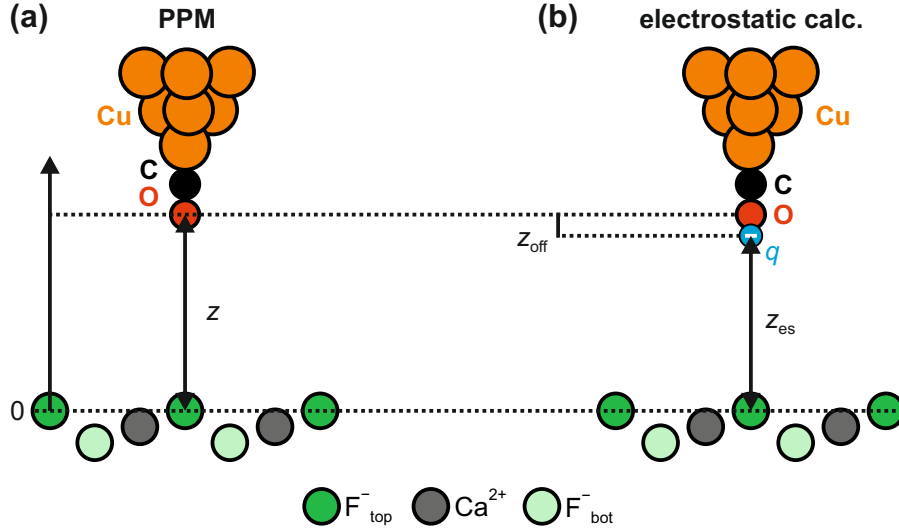


**Figure 5.9.:** Comparison of the vertical distances in the different models.

(a) In the PPM the distance  $z$  is defined as the vertical distance between the  $F_{\text{top}}^-$  and the tip apex oxygen nuclei. (b) In the electrostatic point charge calculation the distance  $z_{\text{es}}$  is defined as the vertical distance between the point charge  $q$  representing the tip apex (blue) and the  $F_{\text{top}}^-$  nucleus. To align both simulations, an offset of  $z_{\text{off}} = 80$  pm needs to be added to  $z_{\text{es}}$ .

the metal tip apex is represented by a positive point charge  $q = +0.13e$ , the CO tip will be modeled as a single negative point charge of  $q = -0.03e$  as estimated by Schneiderbauer *et al.* in Ref. [137].

Whereas in the PPM the tip-sample distance  $z$  is defined as the vertical distance between the  $F_{\text{top}}^-$  and the tip apex oxygen nuclei, the distance  $z_{\text{es}}$  is defined as the vertical distance between the point charge  $q$  representing the tip apex and the  $F_{\text{top}}^-$  nucleus in the electrostatic calculation as illustrated in Fig. 5.9. As shown in Fig. 5.4, the negative charge density responsible for the electrostatic tip-sample interaction on  $\text{CaF}_2(111)$  is located slightly in front of the oxygen nucleus. Hence, the  $z$  axes of both models are aligned by adding an offset of  $z_{\text{off}} = 80$  pm to the tip-sample distance obtained from the electrostatic calculation as shown in Fig. 5.9. The offset  $z_{\text{off}}$  is determined by comparing the electrostatic force contrast  $\Delta F_{\text{es}}$  that is obtained from the PPM calculation presented in section 5.2.1 to the force contrast obtained from the electrostatic point charge calculation. Figure 5.10 shows the electrostatic force contrast obtained from the PPM (red) as well as the electrostatic point charge calculation (blue) as a function of tip-sample distance  $z$  after aligning both calculations. The contrast is calculated by subtracting the force determined above the  $\text{Ca}^{2+}$  atom from the force determined above surface  $F_{\text{top}}^-$  atom. Indeed, for tip-sample distances larger than  $z = 400$  pm, where short-range electrostatics dominate the AFM contrast, both

## 5 Quantifying the evolution of atomic interaction of a CO-terminated tip with a complex ionic crystal surface

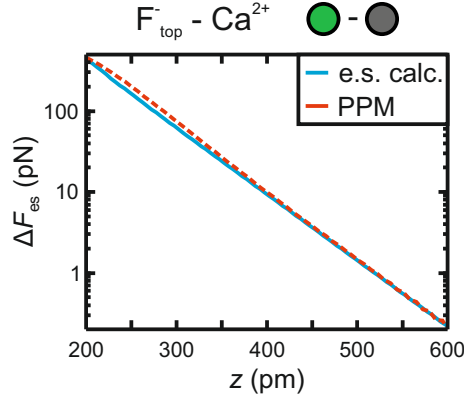


**Figure 5.10.: Comparison of the calculated electrostatic force contrast in the different models.** The electrostatic (e.s.) force contrast  $\Delta F_{\text{es}}$  is calculated by subtracting the force determined above the  $\text{Ca}^{2+}$  atom from the force determined above surface  $F_{\text{top}}^-$ . An offset of  $z_{\text{off}} = 80$  pm has been added to the tip-sample distance  $z_{\text{es}}$  in the electrostatic point charge calculation.

calculations show an exponential decay as expected due to the electric field outside the  $\text{CaF}_2(111)$  surface and match each other. For smaller tip-sample distances the PPM slightly deviates from the exponentially-decaying electrostatic calculation. Overall, this illustrates that representing the CO tip apex with a single negative point charge is a reasonable approximation to estimate the short-range electrostatic tip-sample interaction between CO tips and an ionic lattice.

Figure 5.11(a) shows an experimental constant-height  $\Delta f$  image of the  $\text{CaF}_2(111)$  surface recorded at a tip-sample distance of  $z = 430$  pm, i.e. at a tip-sample distance regime where short-range electrostatics dominate the AFM contrast. As discussed in section 5.2.1, images recorded of the surface at this distance regime present three prominent sites that correspond to the atomic positions of the surface  $\text{CaF}_2(111)$  triple layer. Figure 5.11(b) shows frequency shift versus distance  $\Delta f(z)$  spectra recorded on the three prominent sites. The constant-height image shown in Fig. 5.11(a) has been recorded at the tip-sample distance  $z_{\text{img}}$ , indicating that the overall tip-sample interaction is attractive in this  $z$  range, as approaching the surface from large tip-sample separations yields entirely negative  $\Delta f$  values. Figure 5.11(c) shows a calculated constant-height  $\Delta f$  image obtained from the electrostatic point charge model. Similar to the experimental constant-height image and the simulated images obtained from the PPM in this regime [Fig. 5.5(a)–(f)], the image presents three prominent sites that correspond to the atoms in the surface  $\text{CaF}_2(111)$  triple layer: the  $\text{Ca}^{2+}$  atoms are imaged dark, i.e. most attractive, the atoms of the surface  $\text{F}^-$  layer are imaged bright, i.e. least attractive, and the sites of intermediate contrast correspond to the atoms of the lower  $\text{F}^-$  layer.

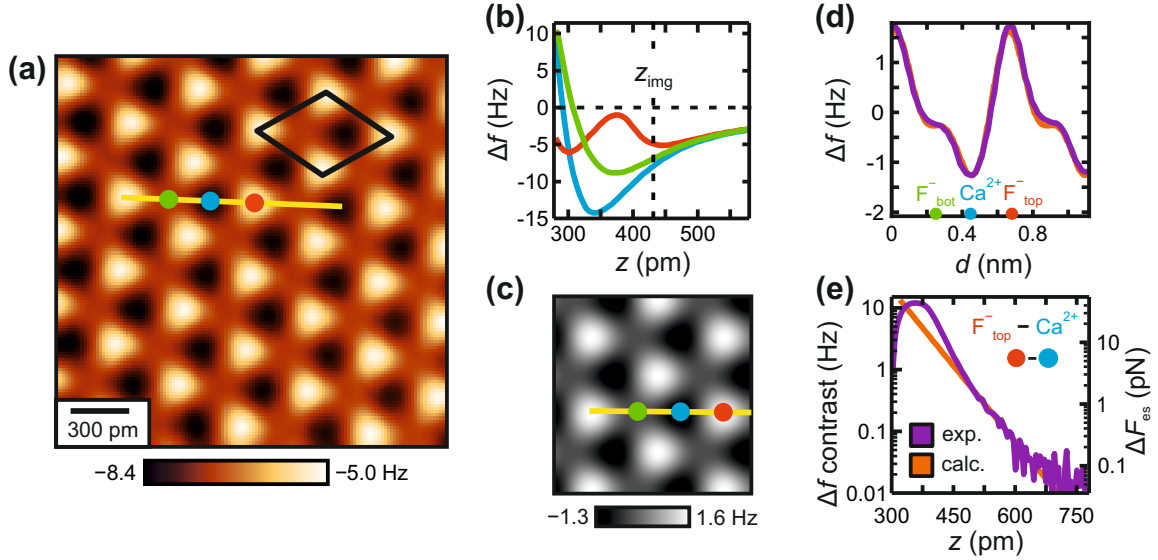


**Figure 5.11.: Experimental and calculated data of the CO tip on CaF<sub>2</sub>(111) in the electrostatic imaging regime.** (a) Experimental constant-height  $\Delta f$  image of the CaF<sub>2</sub>(111) surface recorded with the CO tip at a tip-sample distance of  $z = 430$  pm. The image is processed with a  $78 \text{ pm} \times 78 \text{ pm}$  Gaussian low-pass filter [157]. The unit cell defined in Fig. 4.1(b) is drawn black in the image. (b) Experimental  $\Delta f(z)$  curves recorded above the three high-symmetry sites marked in (a). The constant-height image in (a) has been recorded at a tip-sample distance  $z_{\text{img}}$ . (c) Calculated constant-height  $\Delta f$  image for a negatively-terminated tip using the electrostatic point charge calculation. (d) Comparison of experimental (purple) and calculated (orange) line profiles following the traces in the respective images (a) and (c). To align the experimental to the calculated data, the average over one period of the profile has been subtracted from each curve. (e) Comparison of experimental and calculated  $\Delta f(z)$  contrasts, together with the calculated electrostatic force contrast  $\Delta F_{\text{es}}$ . Figure adapted from Ref. [139].

In order to quantify the success of the electrostatic point charge calculation, the relative quadratic deviation (RQD) and from that the accuracy are calculated according to eqs. (4.22) and (4.23). This is done analogously to the experiment with the single-atom metal tip presented in chapter 4. For this purpose, line profiles are extracted from the experimental and calculated images as shown in Fig. 5.11(d). As the experimental images are offset with respect to the calculation due to the contribution of long-range van der Waals background forces, the experimental and calculated line profiles are aligned by subtracting the average over one surface period of the respective profile from each curve. For the line profiles depicted in Fig. 5.11(d) one obtains  $\text{RQD} = 0.4\%$  resulting in an accuracy of 99.6%, which illustrates that approximating the electric field of CO tips with a single negative point charge is sufficient to reproduce the electrostatic interaction of CO tips with ionic lattices.

Furthermore, in order to compare also the  $z$ -dependence of the AFM contrast in this

## 5 Quantifying the evolution of atomic interaction of a CO-terminated tip with a complex ionic crystal surface

---

regime the difference between two  $\Delta f(z)$  curves, in particular between spectra measured on the  $F_{\text{top}}^-$  and the  $\text{Ca}^{2+}$  sites, can be considered [159] as shown in Fig. 5.11(e). The calculated  $\Delta f$  contrast (orange curve) decays exponentially with  $z$  with the expected decay length  $\lambda = 53.2$  pm of the electric field of  $\text{CaF}_2(111)$  as described in section 4.1.2. For  $z$  values larger than 450 pm also the experimental  $\Delta f$  contrast decays exponentially with distance, where the decay length  $\lambda_{\text{exp}} = (53 \pm 3)$  pm matches the calculated decay rate. The  $\Delta f$  contrast at these tip-sample distance lies in the millihertz regime, which corresponds to an electrostatic force contrast in the femtonewton regime as determined from the point charge calculation [Fig. 5.11(e)]. At closer tip-sample distances ( $z < 450$  pm) the experimental spectrum deviates from the exponential behavior and the electrostatic calculation can no longer reproduce the measured contrast.

### 5.4. Discussion

The experimental data presented in chapter 4 and in chapter 5 have been recorded with two tip apices that present an opposite charge polarity at the tip apex. This indeed influences the AFM contrast recorded on the  $\text{CaF}_2(111)$  surface. As illustrated in Fig. 5.12, when comparing the data recorded with the positively-terminated metal tip [Fig. 5.12(a)] to the data recorded with the negatively-terminated CO tip [Fig. 5.12(b)], the contrast is inverted at a distance where electrostatics dominate the imaging mechanism. While the surface  $F_{\text{top}}^-$  atoms (marked by the red dots in Fig. 5.12) are imaged dark, which means more attractive with the single-atom metal tip, they are imaged bright (less attractive) with the CO tip. Additionally, the  $\text{Ca}^{2+}$  atoms (blue dots) are imaged bright (less attractive) with the metal tip and dark (more attractive) with the CO tip. In agreement to previous studies [35, 137], this contrast inversion is a result of the opposite effective tip apex polarities when imaging an ionic lattice. Metal tips present a positive pole at the tip apex due to the Smoluchowski effect [35, 36, 130, 136–138], while the negative charge density in front of the oxygen atom at the CO tip apex is relevant when imaging an ionic lattice [35, 36, 137].

At the largest tip-sample distances where the surface is resolved with atomic resolution, a single negative point charge is sufficient to reproduce the short-range electrostatic interaction of the CO tip with the defect-free ionic lattice. Upon approaching the surface the atomic contrast is governed by Pauli repulsion and the CO molecule at the tip apex is subject to strong lateral deflections around the exposed  $F_{\text{top}}^-$  atoms, which completely changes the AFM contrast. The PPM successfully reproduced the unique contrast patterns observed in the tip-sample distance regime. This illustrates

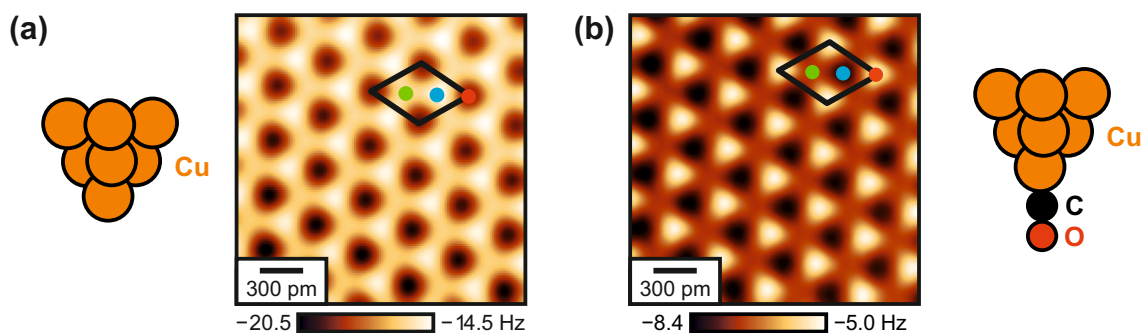


**Figure 5.12.:** Comparison of experimental constant-height images of CaF<sub>2</sub>(111) measured with metal and CO tips. (a) Experimental constant-height  $\Delta f$  image of the CaF<sub>2</sub>(111) surface recorded with the metal tip, as shown already in Fig. 4.5(a). (b) Experimental constant-height  $\Delta f$  image of the CaF<sub>2</sub>(111) surface recorded with the CO tip, as shown already in Fig. 5.11(a). The unit cell defined in Fig. 4.1(b) is drawn in both images, showing that the contrast is inverted between the two images. Equivalent high-symmetry sites are marked by the colored dots.

that the treatment of the CO bending mechanism in the PPM model is valid also for a corrugated ionic crystal surface like CaF<sub>2</sub>(111).

In this chapter, two different PPM calculations were presented yielding similar results. Hence, this approach allows to compare the degree of correspondence between the standard approach based on Lennard-Jones interaction potentials and the density overlap method developed by Ellner *et al.* [178]. Overall, the calculation based on the overlap of electron densities yields a better agreement to the experimental data, reproducing the experimentally observed contrast pattern in good agreement at all accessible tip-sample distances. Moreover, in common classical force fields there are no good estimates of Lennard-Jones radii valid for ionic crystal surfaces. Hence, the ionic radii of the sample atoms need to be modified in the Lennard-Jones-potential-based calculation as previously performed by Peng *et al.* in case of sodium cations hydrated by water on a NaCl surface [125]. In the calculation that relies on the overlap of the electron densities of tip and sample the ionic radii are obtained *ab initio*. Therefore, the approach of combining high-resolution AFM imaging with detailed DFT simulations presented in this chapter can be employed to validate ionic radii that are used in classical force field simulations. This could be interesting for the development of biochemical simulations of processes like the interactions of proteins or DNA with ions on surfaces and in solution that can be performed with molecular force field simulations like AMBER [179].

In the experiment with the single-atom metal tip presented in chapter 4 it was possible to stably record images only in the attractive regime. Terminating the tip with a CO molecule effectively passivates the tip apex and enables data acquisition

## 5 Quantifying the evolution of atomic interaction of a CO-terminated tip with a complex ionic crystal surface

---

also in the repulsive imaging regime at smaller tip-sample distances as discussed in this chapter. At closest tip-sample distances, the CO molecule at the tip apex is subject to strong lateral deflections due to lateral components in the tip-sample interactions, which drastically alters the appearance of the surface in constant-height  $\Delta f$  images. Recently, Mönig *et al.* showed that O-terminated Cu tips provide a similar spatial resolution as CO tip but possess a much higher lateral stiffness [38, 180]. Characterization of successful tip functionalization with oxygen relies on the theoretical and experimental analysis of STM and AFM images of oxidized copper surfaces. Chapter 6 introduces a straightforward characterization of the tip apex of O-terminated Cu tips using the COFI method that has been successfully applied already for the characterization of metal and CO tips.

## 6. *In-situ* characterization of O-terminated Cu tips based on the COFI method

*Most of the work presented in this chapter has been published in Applied Physics Letters [169].<sup>1</sup> Parts of the text, figures and interpretations are identical to the publication. The author performed all experiments and carried out the complete data analysis.*

The previous chapters reported on AFM measurements on CaF<sub>2</sub>(111) with single-atom metal and CO-terminated tips. The use of metal tips allows imaging of the surface only in the attractive regime. On the contrary, terminating the tip apex with CO effectively passivates the tip apex, which allows data acquisition also in the repulsive imaging regime closer to the surface. Although functionalizing the tip with a CO molecule yields an increase in spatial resolution, interpretation of atomic-scale contrast with these tips is highly nontrivial: when the tip interacts with the sample, lateral forces cause lateral deflection of the CO molecule that can create artifacts in the images and, hence, inhibit a direct interpretation of data [16, 18, 21–23]. Recently, Mönig *et al.* proposed using oxygen-terminated Cu tips (CuOx tips) that show a comparable spatial resolution and much higher lateral stiffness of the tip apex [38, 180]. With such CuOx tips it is for example possible to quantitatively measure intramolecular bond lengths [180], which appear elongated when using CO tips [18] and, theoretically, to scan with video rate imaging velocities [181]. Recently, Yesilpinar *et al.* showed that CuOx tips are stable also at liquid nitrogen temperatures ( $T \approx 78$  K) where CO would desorb from the tip apex, yielding intramolecular resolution on organic molecules [182].

While the functionalization of a metal tip with a CO molecule is a well-controlled process [113], CuOx tips are prepared by repeated collisions of the tip with an ox-

---

<sup>1</sup>A. Liebig and F. J. Giessibl, *In-situ characterization of O-terminated Cu tips for high-resolution atomic force microscopy*, Appl. Phys. Lett. **114**, 143103 (2019).

dized Cu surface [38]. This is a random process involving many atoms of both tip and sample, which means that the exact atomic structure and the chemical species of the atoms composing the tip apex after the collision are unknown. Knowledge of the chemical and structural identities of the tip is of crucial importance, especially when experiments are accompanied by calculations involving the tip structure and its chemical composition. In existing literature, characterization of successful tip functionalization with oxygen relies on the theoretical and experimental analysis of STM and AFM images of oxidized copper surfaces, which serve as a tip fingerprint [183–186]. A description of the atomic tip apex structure requires a large tip model database obtained after extensive and time-consuming simulations, and precise determination of the structural apex composition is not always possible [186].

This chapter presents experimental characterization of CuOx tips by a combination of COFI and force spectroscopy on a Cu(110) surface to determine both the structural and the chemical compositions of the tip apices *in-situ*. First, the preparation of CuOx tips on a partially oxidized Cu(110) surface is introduced (section 6.1). Second, COFI and force spectroscopy data of CuOx tips terminated by a single O atom are presented (section 6.2). The data recorded with CuOx tips is compared to data recorded with CO-terminated tips. For comparison to existing literature tip fingerprinting experiments conducted with CuOx tips that have been previously characterized with COFI and force spectroscopy are presented. Finally, the experimental characterization of CuOx tips with multiple oxygen atoms at the tip apex is introduced in section 6.3.

### 6.1. Oxygen tip functionalization on the Cu(110)-(2×1)O surface

Functionalizing a single-atom metal tip with a single CO molecule is a well-controlled process, as CO-terminated tips can be prepared by picking up a CO molecule from a copper surface (see section 3.3) [113]. On the contrary, single oxygen atoms cannot be picked up from a surface in a similarly controlled way so far and preparation of O-terminated tips relies on repeated collisions of the tip with an oxidized Cu surface [38]. This section briefly explains how CuOx tips can be prepared on a partly oxidized Cu(110) surface and how the geometric tip apex structure is determined in existing literature.

All experimental data presented in this chapter have been, except when mentioned otherwise, recorded with a qPlus sensor (type qPlus M4 [54]) equipped with

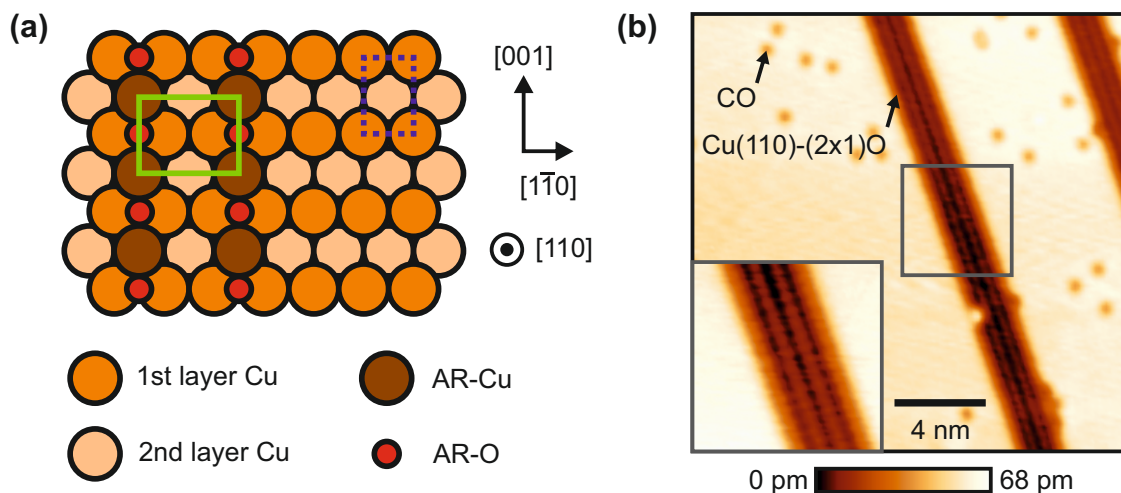


**Figure 6.1.: Partly oxidized Cu(110) surface used for CuOx tip preparation.**

(a) Top view schematic of the Cu(110)-(2×1)O added-row reconstruction. Additional Cu atoms (AR-Cu) align directly on top of Cu atoms in the second layer, forming rows with oxygen atoms (AR-O) along the [001] direction. The green rectangle marks the unit cell of the (2×1) reconstruction and the blue dashed rectangle marks the Cu(110) surface unit cell. (b) STM overview image of the partly oxidized Cu(110) surface. Dark, striped regions represent the copper oxide domains on Cu(110). Single, dark points are individual CO molecules adsorbed on the bare Cu(110) surface. Imaging parameters: sample bias  $V_b = -100$  mV, tunneling current setpoint  $\langle I \rangle = -100$  pA. Inset: Zoom into the area marked by the gray square. Figure adapted from Ref. [169].

an electrochemically-etched tungsten tip, showing a resonance frequency of  $f_0 = 46\,597$  Hz, a stiffness of  $k = 1800$  Nm $^{-1}$ , and a quality factor of  $Q = 482\,321$ . The CuOx tips presented in this chapter have been prepared on a partly oxidized copper surface following the procedure described by Mönig *et al.* [38]. Upon low oxygen coverages, Cu(110) undergoes a (2×1)-O added-row (AR) reconstruction forming striped copper oxide domains along the [001] directions as shown in Fig. 6.1 [38, 187–190]. The copper oxide domains consist of additional copper atoms (AR-Cu) forming a (2×1) reconstruction on top of the regular Cu(110) surface with oxygen atoms (AR-O) between the AR-Cu atoms as sketched in Fig. 6.1(a). For comparison, the unit cell of the (2×1) reconstruction is marked by the green rectangle and the regular Cu(110) surface unit cell is marked by the blue dashed rectangle in Fig. 6.1(a).

For sample preparation, first, a clean Cu(110) surface is prepared using standard sputtering and annealing cycles as described in section 3.3. After the last annealing step the sample temperature is regulated between 200 °C and 250 °C using the boron-nitride heater at the manipulator in the preparation chamber. Then, molecular oxygen is dosed to the chamber to a pressure of about  $3 \times 10^{-8}$  mbar for 30 seconds via the gas line system followed by an additional annealing cycle at a temperature

of about 410°C. This results in the formation of the Cu(110)-(2 × 1)O-AR reconstruction. The lateral size of the copper oxide domains, i.e. the average number of rows that form one copper oxide stripe, can be regulated by changing the oxygen dosage pressure and time. In order to characterize the tips using the COFI method, carbon-monoxide has been dosed to the analysis chamber after the sample was cooled to 4.4 K at the microscope stage to cover the surface with approximately 0.005 ML of CO. It is noteworthy that the COFI method exploits the vertical on-top adsorption configuration of individual CO molecules on Cu(111) with the O atom pointing away from the surface. Here, the COFI method is used on Cu(110) where CO also adsorbs in this vertical on-top configuration as determined by photo-electron diffraction [191]. Figure 6.1(b) shows an STM feedback image recorded with a metal tip of the sample as it is used for tip preparation. Although topographically higher, the striped copper oxide domains are imaged as darker regions in the STM image. The single dark spots in Fig. 6.1(b) correspond to CO molecules adsorbed on the surface.

As stated above, CuOx tips are prepared by repeated indentations of the tip into the copper oxide domains following the procedure described in Ref. [38]. The following paragraph briefly summarizes the tip preparation protocol. First, a reasonably sharp tip needs to be prepared by poking into the bare Cu surface as explained in section 3.3 for the Cu(111) surface. Experiments showed that the poking parameters can be directly transferred to the Cu(110) surface to generate a sharp metal tip apex. The macroscopic sharpness of the tips can be judged from the frequency shift signal in STM feedback [38]. In the experiments it turned out that if the frequency shift is greater (more positive) than a threshold value of  $\Delta f = -12$  Hz for a bias voltage of  $V_b = -100$  mV and a tunneling current setpoint of  $\langle I \rangle = -100$  pA, the tip can be assumed to be sufficiently sharp to continue the preparation. The tip is then poked into the copper oxide domains with poking depths between 400 pm and 900 pm from the above-mentioned STM setpoint settings and bias voltages during the poking below 1 V. This process is repeated until a notable enhancement in corrugation within the copper oxide domains is observed in STM images. Figure 6.2(a) shows an STM image recorded of the copper oxide domain with a bare metal tip and the corresponding line profile extracted along the green line in the image shows only a slight corrugation of less than 10 pm within the Cu(110)-(2 × 1)O-AR reconstruction. On the contrary, STM images recorded of copper oxide domains after successfully functionalizing the tip apex with oxygen show an enhanced corrugation of up to 30 pm as shown in Fig. 6.2(b). The contrast enhancement is an indication of a change in the chemical species of the tip terminating atom [186].

This concept of repeated collisions between tip and sample in order to functionalize

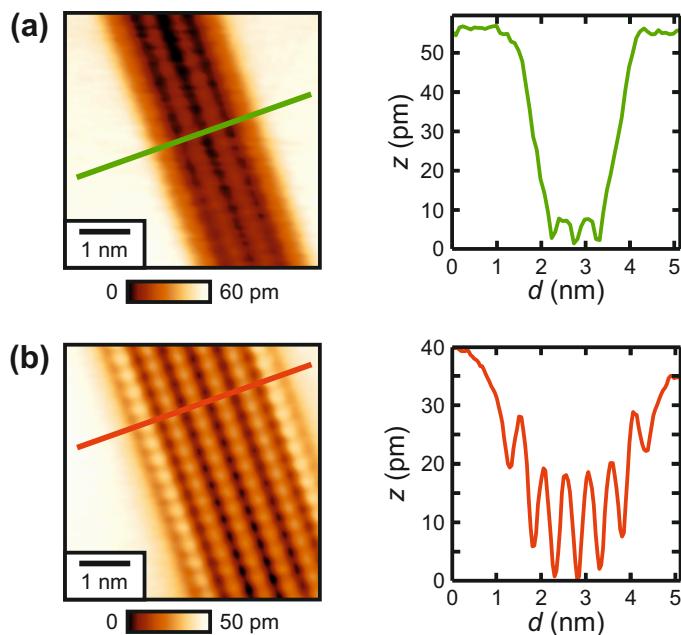


**Figure 6.2.: Contrast enhancement on the copper oxide domain upon tip apex oxidation.** (a) STM feedback image of the Cu(110)-(2 × 1)O-AR reconstruction recorded with a bare metal tip. The line profile extracted along the green line in the image shows that the corrugation in the image is less than 10 pm within the copper oxide domain. (b) STM feedback image of the Cu(110)-(2 × 1)O-AR reconstruction recorded with a CuOx tip. The corrugation within the copper oxide domain is up to 30 pm in the STM image, as shown in the corresponding line profile. Note that the images show two different oxide domains with different lateral size [4 added rows in (a) versus 6 rows in (b)]. Figure adapted from Ref. [169].

the tip with oxygen is a random process involving many tip and surface atoms. As a result, the exact atomic structure and chemical species of the atoms composing the tip apex after the collision are unknown. Knowledge of the chemical and structural identities of the tip is of crucial importance especially when experiments are accompanied by calculations involving the tip structure and its chemical composition. Hence, these properties should be well-characterized in the experiment. In existing literature, the chemical species of the tip-terminating atom is determined by using the imaging contrast of oxidized copper surfaces as a *tip fingerprint* by comparing the contrast in experimental STM and AFM images to DFT-based calculations [38, 180, 183–186]. This comparison is, however, generally based on idealized tip structures and hence, only the chemical species of the tip apex atom can be determined but not the exact tip apex structure. A complete description of the tip apex would therefore require a large tip model database, which is obtained only after extensive and time-consuming simulations. As a consequence, a precise determination of the structural composition

is not always possible [186] and the tip apex can be characterized only after the experimental data has been acquired by comparison to the simulations. In the next section, the COFI method is established as an efficient method to *in-situ* characterize the tip apex of O-terminated Cu tips during the experimental tip preparation procedure.

### 6.2. COFI characterization of O-terminated Cu tips

As explained in section 6.1, in order to functionalize the tip with oxygen it is repeatedly poked into the copper oxide domains until a change in the STM contrast within the Cu(110)-(2 × 1)O-AR reconstruction is noticed, which indicates a change of the chemical species of the tip-terminating atom. This section describes the subsequent characterization of the tip apex by a combination of COFI and force spectroscopy on the Cu(110) surface.

As illustrated in Fig. 6.3(a) and explained in section 3.3, in COFI the tip is scanned at a constant height above a CO molecule adsorbed on a copper surface. The CO acts as a probe and the resulting images reveal the atomic configuration of the tip apex [30–32]. Additionally, the chemical species of atoms can be distinguished by force spectroscopy. Sugimoto *et al.* showed that the chemical species of different surface atoms can be determined by analyzing the minimum in short-range force versus distance  $F_{\text{SR}}(z)$  spectra measured above individual surface atoms [192]. This discrimination is possible if it can be ensured that all  $F_{\text{SR}}(z)$  spectra have been measured with the same tip apex. From the analysis of the relative shift of the short-range force minima different chemical species of surface atoms could be distinguished. By knowing the chemical species on the surface this concept can be transferred to determine the chemical species of the tip apex atom. Hofmann *et al.* distinguished between the chemical species of the front-most atom of different single-atom metal tips using force spectroscopy above the same chemical species on the surface, i.e. a single CO molecule adsorbed on Cu(111) [29]. Depending on the metal atom that terminates the tip apex different short-range force minima are measured by force spectroscopy, which allows to distinguish between different chemical species.

The interaction of a CuOx tip with a CO molecule adsorbed on the Cu(110) surface is comparable to the findings of Sun *et al.*, who investigated the interaction of a CO tip with CO/Cu(111) both experimentally and theoretically [16]. Figure 6.3(c) shows frequency shift versus distance  $\Delta f(z)$  spectra recorded with a CuOx tip above the CO molecule (blue curve) and above the bare Cu(110) surface (black curve), respectively. The zero point of the experimental  $z$  axis defines the closest tip-sample approach in the measurements with this tip. Approaching the surface from  $z = 1$  nm,

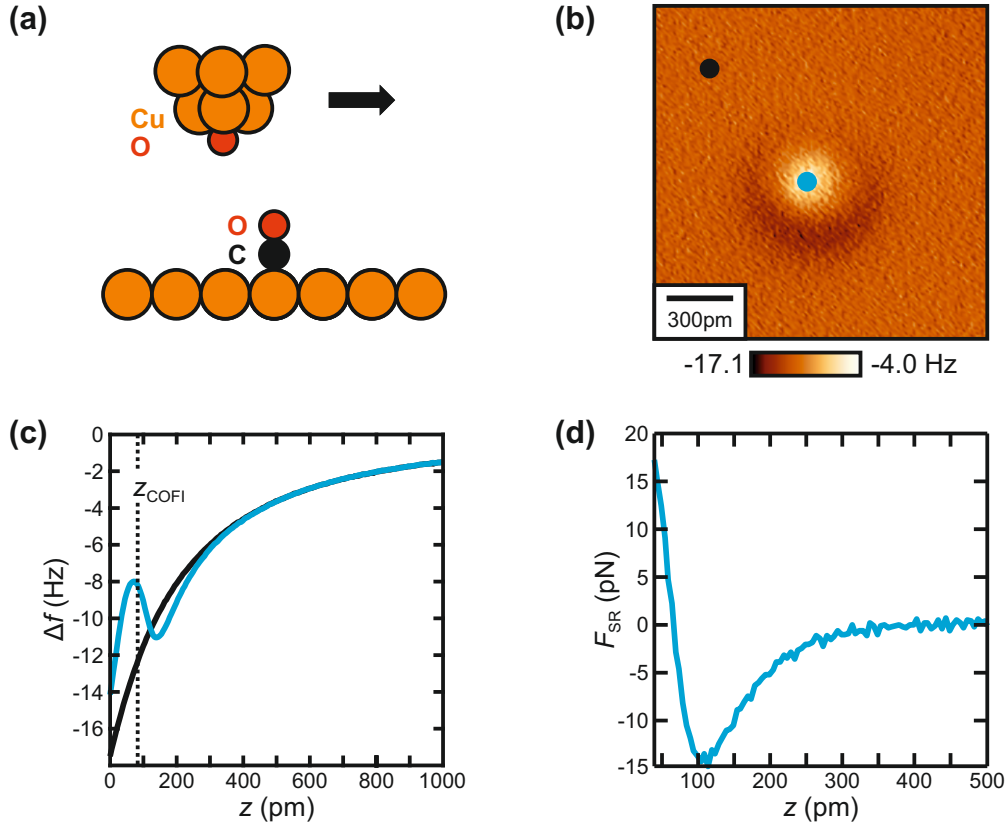


**Figure 6.3.: COFI characterization of O-terminated Cu tips.** (a) Schematic of the COFI method: an AFM tip, in this case a CuOx tip, is scanned at relatively close distance at constant height above a CO molecule adsorbed on the Cu(110) surface. (b) COFI image of a CuOx tip as sketched in (a). (c)  $\Delta f(z)$  spectra recorded above the CO molecule (blue curve) and the bare Cu surface (black curve), positions marked in (b). The zero point of the  $z$  axis defines the closest approach, in the measurement.  $z = 100$  pm corresponds to the STM setpoint  $V_b = -100$  mV,  $\langle I \rangle = -100$  pA above the bare Cu surface. The COFI image shown in (b) has been recorded at  $z_{\text{COFI}}$ . (d) Short-range force versus distance  $F_{\text{SR}}(z)$  spectrum obtained by subtracting the  $\Delta f(z)$  spectrum acquired above the Cu(110) surface [black in (c)] from the spectrum acquired in the center of the CO molecule [blue in (c)] and subsequent force deconvolution [78]. Figure adapted from Ref. [169].

the  $\Delta f$  values are initially less above the CO molecule compared to the bare Cu surface, which can be attributed to van der Waals attraction between the tip and the CO molecule [16]. Upon further approach, the spectrum above the CO reaches a minimum and starts to increase, which can be assigned to stronger contribution of short-range Pauli repulsion between the tip and the CO molecule [16]. If the tip-sample distance is further reduced, the curve recorded above the CO reaches a maximum and starts to decrease again. This can be attributed to the lateral deflection of the CO on the surface, which leads to an increase in the nominal distance between

the tip apex and the adsorbate's oxygen atom resulting in a decreased contribution of Pauli repulsion [16]. A constant-height  $\Delta f$  image (a COFI image) recorded of the CuOx tip at the tip-sample distance, where the spectrum recorded above the CO molecule reaches a maximum,  $z_{\text{COFI}}$ , is shown in Fig. 6.3(b). The tip apex is resolved as a single bright, circularly-symmetric feature with a dark ring around it. In analogy to the  $\Delta f(z)$  spectra, the bright feature in the center of the COFI image is a result of Pauli repulsion between the tip and the CO, which leads to a shift of the  $\Delta f$  signal to larger values. The dark ring stems from the contribution of van der Waals attraction that dominates the interaction at slightly larger separations between the tip apex and the CO. The positions at which the two  $\Delta f(z)$  spectra shown in Fig. 6.3(c) have been recorded are marked by the colored dots in Fig. 6.3(b).

Figure 6.4 shows COFI images of this CuOx tip as a function of tip-sample distance  $z$  to further illustrate the AFM contrast evolution. Far from the surface the contrast is initially governed by long-range van der Waals attraction between the tip and the CO molecule, which results in lower  $\Delta f$  values above the CO, as can be seen in Fig. 6.4(a)–(c). The contrast in the COFI images inverts upon approach due to the onset of short-range Pauli repulsion between the CO molecule and the O atom at the tip apex, which leads to larger  $\Delta f$  values above the CO [Fig. 6.4(d)–(f)]. At close distances [Fig. 6.4(g),(h)], the above-mentioned CO bending leads to artifacts in the center of the images.

To isolate the interaction between the tip and the CO molecule, the short-range component needs to be extracted from the total tip-sample interaction. For a single adsorbate like CO/Cu(110), the short-range interaction component can be obtained by performing the “on - off” subtraction method [16, 17, 29]. If the AFM contrast measured above the bare surface shows no atomic corrugation, as it is the case for the COFI images shown in Fig. 6.4, one can assume that the tip-surface interaction on the bare surface is purely long-range. Hence, by subtracting a spectrum recorded above the bare Cu(110) surface,  $\Delta f_{\text{off}}(z)$ , from a spectrum recorded above the CO molecule,  $\Delta f_{\text{on}}(z)$ , one obtains the short-range interaction between the tip and the molecule  $\Delta f_{\text{SR}}(z) = \Delta f_{\text{on}}(z) - \Delta f_{\text{off}}(z)$ . The short-range force  $F_{\text{SR}}(z)$  can then be calculated from  $\Delta f_{\text{SR}}(z)$  via the Sader-Jarvis force deconvolution method [78]. Figure 6.3(d) shows the short-range force obtained after subtracting the spectrum recorded above the Cu(110) surface [black curve in Fig. 6.3(c)] from the spectrum recorded above the CO molecule [blue curve in Fig. 6.3(c)] and subsequent force deconvolution. The force deconvolution has been explicitly checked for well-posed behavior in the displayed  $z$  range using the inflection point test developed in Refs. [80, 81] (see section 2.2.3). For smaller tip-sample distances, the lateral deflection of the CO adsorbate leads

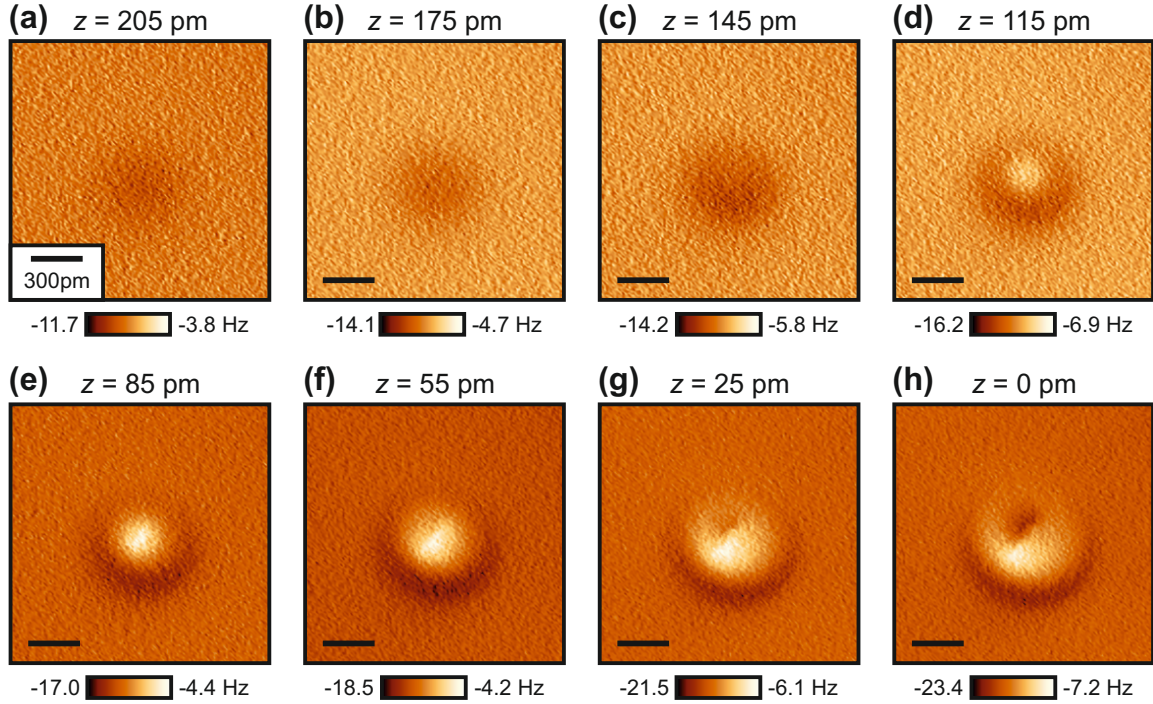


**Figure 6.4.: Height-dependent COFI images of a CuOx tip.** COFI images of the CuOx tip shown in Fig. 6.3 as a function of tip-sample distance  $z$ , which is defined according to Fig. 6.3(c).  $z = 0$  pm defines the closest approach in the measurement with this CuOx tip, which is 100 pm closer from the STM setpoint above the bare Cu surface ( $V_b = -100$  mV,  $\langle I \rangle = -100$  pA). The images have been recorded with zero bias voltage. All scale bars are 300 pm long. Figure adapted from Ref. [169].

to the occurrence of multiple inflection points and the force deconvolution turns ill-posed, which leads to unreliable force values. Hence, Fig. 6.3(d) shows  $F_{\text{SR}}(z)$  only in the well-posed tip-sample distance regime. The short-range force curve exhibits a minimum of about  $F_{\text{SR},\text{min}} = -15$  pN. Figure 6.5 presents short-range force versus distance curves  $F_{\text{SR}}(z)$  measured for twelve different CuOx tips on CO/Cu(110) that all presented similar COFI portraits, all exhibiting short-range force minima between  $F_{\text{SR},\text{min}} = -15$  pN and  $F_{\text{SR},\text{min}} = -30$  pN. In order to align the curves with respect to the tip-sample distance  $z$  the zero point of the  $z$  axis in Fig. 6.5 is set to the short-range force minimum.

A possible explanation for the spread in the short-range force minima could be attributed to different configurations of the tip background, i.e. the atomic configuration behind the O atom at the tip apex. Whereas CO-terminated tips are prepared by first shaping a metal tip to end in a single atom which is followed by the controlled pick-up of a single CO molecule from the surface, CuOx tips are prepared by repeated indentations of the tip into copper oxide domains as described in section 6.1. Hence, the macroscopic shape of the tip close to the apex cannot be controlled in the ex-

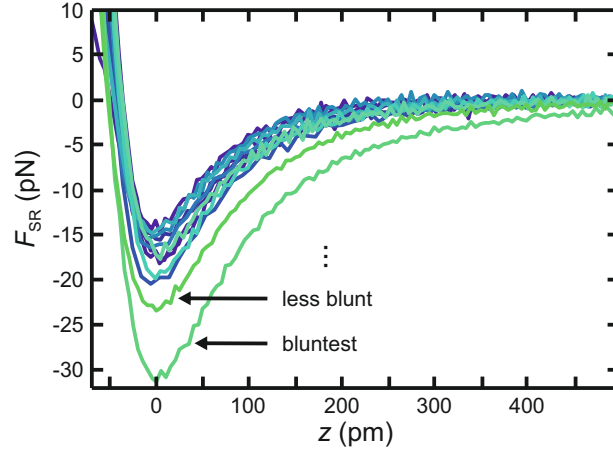


**Figure 6.5.: Short-range force versus distance curves for different CuOx tips.** Short-range force versus distance  $F_{\text{SR}}(z)$  curves for twelve different CuOx tips recorded above a CO molecule adsorbed on a Cu(110) surface. The spectra have been aligned by setting the short-range force minimum to  $z = 0$  pm. Figure adapted from Ref. [169].

periment and, according to eq. (2.10), blunter tips yield an increased van der Waals attraction between the tip and the CO adsorbate compared to sharper tips. A second factor could be tiny offsets in the lateral tip position above the CO molecule for the individual spectra. The tip is positioned laterally at the point of maximum attraction above the CO molecule for the  $\Delta f_{\text{on}}(z)$  spectrum. If the tip position is slightly shifted laterally from that point, this will reduce the attractive interaction and hence also the short-range force minimum. This should, however, only slightly affect the  $F_{\text{SR},\text{min}}$  values and cannot explain the factor of two difference as it is the case for the data shown in Fig. 6.5. Therefore, uncertainties arising from the lateral tip positioning can be ruled out as the main reason for the spread of the  $F_{\text{SR},\text{min}}$  values.

### 6.2.1. Comparison to COFI data of CO-terminated tips

As stated above, the interaction of CuOx tips with a CO molecule adsorbed on Cu(110) is comparable to the findings of Sun *et al.* for the interaction of a CO tip with a CO molecule adsorbed on Cu(111) [16]. For comparison, this section presents AFM measurements with a CO tip on CO/Cu(110). The experiments with the CO tip have been performed by Dr. Florian Pielmeier in the group of the author on the same low-temperature microscope in 2013 and were analyzed by the author for publication in Ref. [169]. The data has been recorded with a qPlus sensor (type qPlus S1.0d [54]) with a stiffness of  $k = 1800 \text{ Nm}^{-1}$ , a resonance frequency of  $f_0 = 27.846 \text{ kHz}$  and a quality factor of  $Q = 39\,034$  that was operated at a constant amplitude of  $A = 50 \text{ pm}$

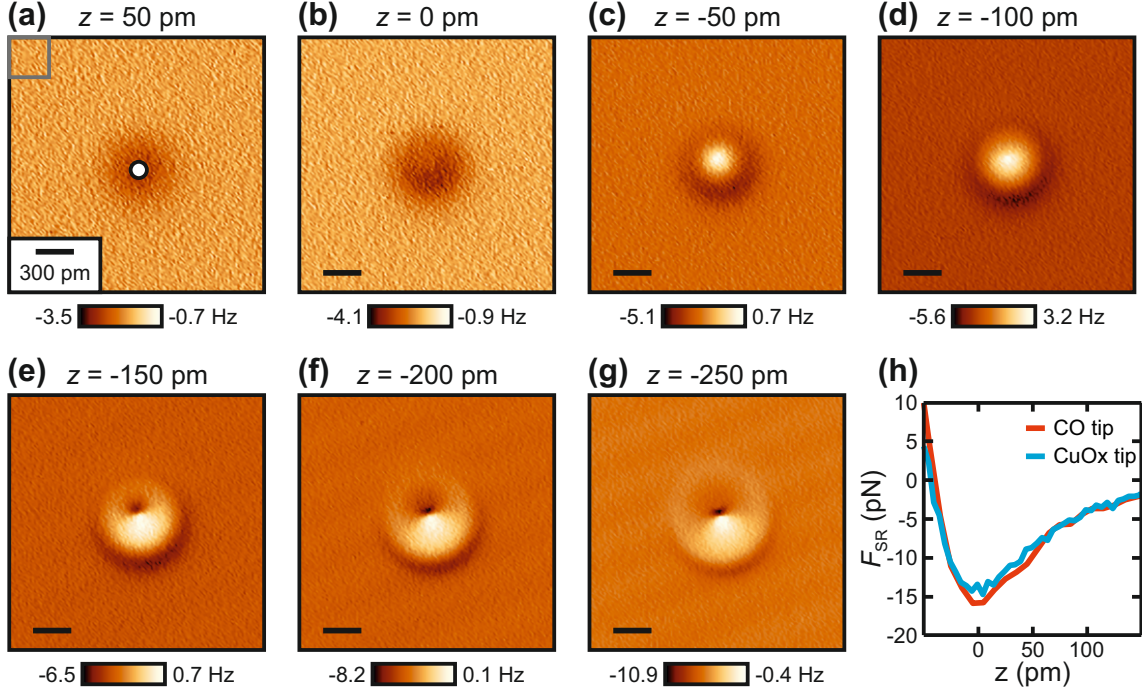


**Figure 6.6.:** COFI data of a CO tip on Cu(110). (a)–(g) COFI images as a function of tip-sample distance  $z$  recorded with a CO-terminated tip on Cu(110). (h) Short-range force versus distance curves  $F_{\text{SR}}(z)$  recorded above a CO molecule with the CO tip shown in (a)–(g) (red curve) and a CuOx tip (blue curve). The spectra have been aligned by setting the short-range force minimum to  $z = 0$  pm. The positions at which the  $\Delta f_{\text{on}}(z)$  and  $\Delta f_{\text{off}}(z)$  spectra have been extracted for the short-range force determination are marked in (a). All scale bars are 300 pm long. Figure partly adapted from Ref. [169].

in the FM-AFM mode.

Figure 6.6(a)–(g) shows COFI images of a CO tip recorded on a Cu(110) surface as a function of tip-sample distance  $z$ . Analogous to Fig. 6.5, the zero point of the  $z$  axis has been aligned with the position of the short-range force minimum as shown in Fig. 6.6(h). The CO-CO interaction measured on Cu(110) shows a similar tip-sample distance dependence to the CO-CO interaction on Cu(111) [16] and the interaction of a CuOx tip with CO/Cu(110) that is presented in the previous section. Initially [Fig. 6.6(a),(b)] the interaction of the CO tip with the CO adsorbate is governed by van der Waals attraction according to Ref. [16], which leads to a more negative  $\Delta f$  signal above the molecule. When the tip approaches the surface short-range Pauli repulsion starts to dominate the tip-molecule interaction, which leads to an increase of the  $\Delta f$  values above the adsorbate as shown in Fig. 6.6(c),(d). At smaller tip-sample distances, both the molecule adsorbed on the surface as well as the CO on the tip apex start to deflect laterally, which leads to artifacts in the images seen as regions

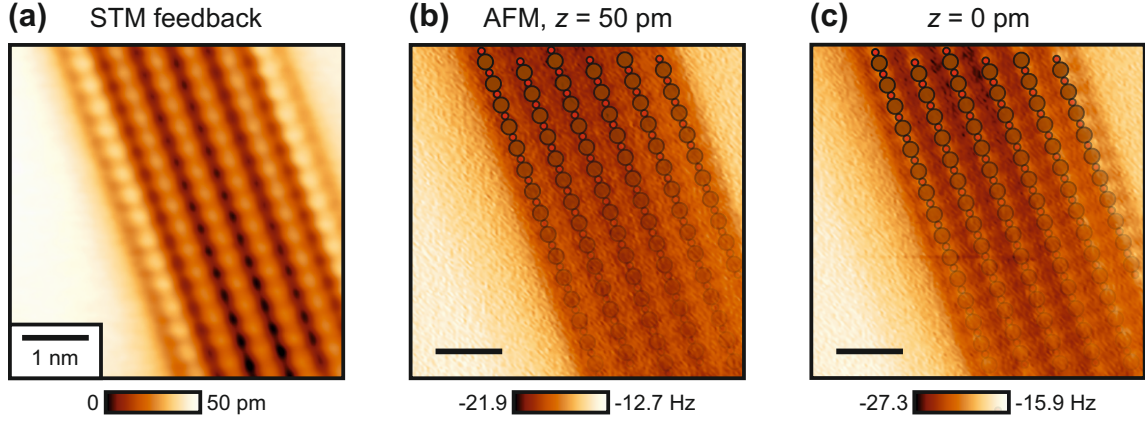
of more negative  $\Delta f$  in the center of the repulsive feature [dark in Fig. 6.6(e)–(g)]. In the image at smallest tip-sample distance  $z$ , Fig. 6.6(g), the atomic rows of the Cu(110) lattice can be already recognized as lines in the constant-height  $\Delta f$  image. The overall frequency shift values in the COFI images of the CO tip are higher than those recorded of the CuOx tip shown in Fig. 6.4. This can be attributed to a decrease of the van der Waals attraction between tip and sample in case of the CO tip: the molecule adsorbed on the tip apex acts as a spacer between the background metal tip and the surface. Hence, the interaction of the bulk tip with the surface is reduced in case of a CO tip as compared to a CuOx tip.

Figure 6.6(h) shows a short-range force versus distance curve  $F_{\text{SR}}(z)$  determined with the “on - off” subtraction method for the CO-CO interaction on Cu(110) (red curve) in a similar way as for the spectra determined for CuOx tips in Figs. 6.3(d) and 6.5. In this case, the  $\Delta f_{\text{on}}(z)$  spectrum has been extracted in the center of the CO molecule from the three-dimensional data set of COFI images as marked by the white dot in Fig. 6.6(a). The background  $\Delta f_{\text{off}}(z)$  spectrum has been determined by averaging the  $\Delta f$  values in the Cu(110) surface area marked by the gray square in Fig. 6.6(a) for each COFI image. The  $F_{\text{SR}}(z)$  spectrum exhibits a minimum of  $F_{\text{SR},\text{min}} = -16$  pN, which is in the same range as for the curves recorded with CuOx tips shown in Fig. 6.5. For direct comparison, an additional  $F_{\text{SR}}(z)$  spectrum recorded with a CuOx tip is shown Fig. 6.6(h) (blue curve). The values obtained for both the CuOx and CO tips are close to the value obtained by Sun *et al.* with a CO tip on Cu(111) [16] and show that oxidizing the tip apex effectively reduces the chemical reactivity of the tip apex [38, 184, 186]: short-range force minima of single-atom metal tips on CO/Cu(111) are typically lower than  $F_{\text{SR},\text{min}} = -130$  pN [29], which is almost a factor of ten difference as compared to CO and CuOx tips.

### 6.2.2. Comparison to tip fingerprinting

In the next step the Cu(110)–(2 × 1)O reconstruction was imaged with CuOx tips after characterizing them with COFI and force spectroscopy. The copper oxide domains were imaged in previous studies to obtain a tip fingerprint, which was used to determine the chemical species of the tip-terminating atom by comparing the experimental images to DFT-based calculations [38, 180] as explained in section 6.1. While the atomic contrast in AFM images recorded at larger tip-sample distances is equal for all CuOx tips, two different types of atomic-scale contrast were observed in AFM images at closest tip-sample distances with different CuOx tips.

Figure 6.7 shows STM and AFM images of a copper oxide domain recorded with



**Figure 6.7.: STM and AFM images recorded of a copper oxide domain with a CuOx tip.** (a) STM image recorded of a Cu(110)-(2 × 1)O domain with a CuOx tip that has been characterized with COFI and force spectroscopy, see Fig. 6.3 and Fig. 6.4. Imaging parameters:  $V_b = -100$  mV,  $\langle I \rangle = -100$  pA. The image has been processed with a  $2 \times 2$  Gaussian low-pass filter [155]. (b) and (c) Constant-height  $\Delta f$  images of the same area as in (a), recorded 50 pm (b) and 100 pm (c) closer than the STM image in (a), corresponding to a distance  $z = 50$  pm (b) and  $z = 0$  pm (c), respectively. Far away (b), the AR-Cu atoms are imaged dark, and at closer distance (c), AR-O atoms are imaged bright. The overlaid structure marks positions of AR-Cu and AR-O atoms. All scale bars are 1 nm long. Figure adapted from Ref. [169].

the CuOx tip, whose COFI and force spectroscopy data is shown in Fig. 6.3 and Fig. 6.4. In the STM topography image shown in Fig. 6.7(a), the maxima within the oxide domain coincide with the AR positions in good agreement with Ref. [180]. Interestingly, the maxima in STM images were found between the added rows in Ref. [38]. This discrepancy can be possibly attributed to different STM imaging heights, which has been found to drastically affect STM images recorded with CuOx tips [186]. While the STM images reported in Ref. [180] and the data reported here were recorded at similar STM setpoints ( $V_b = 100$  mV,  $\langle I \rangle = 50$  pA in Ref. [180] and  $V_b = -100$  mV,  $\langle I \rangle = -100$  pA in this work), the images reported in Ref. [38] were recorded at ten times larger conductance, implying that the tip-sample distance is approximately 100 pm smaller. Additionally, not only the tip apex atom but the atomic configuration near the tip apex can influence the appearance of surface features in STM images with CuOx tips [186]. As the second layer of tip atoms cannot be easily accessed experimentally, an influence of second layer atoms cannot be ruled out.

To obtain significant contrast in constant-height AFM images the tip was then approached to the sample from the STM imaging height. The atomic features that are resolved first are depressions [Fig. 6.7(b)], which can be attributed to the AR-Cu atoms in excellent agreement with previously reported AFM images of the Cu(110)-

$(2 \times 1)\text{O}$  reconstruction with CuOx tips [38, 180]. Further approaching the surface leads to the emergence of increasing  $\Delta f$  [bright features in Fig. 6.7(c)] above the AR-O atomic sites, which dominate the image contrast within the copper oxide domain. The increasing  $\Delta f$  values above the AR-O atoms can be expected from short-range Pauli repulsion between the tip and the surface oxygen atoms as evident from calculated force versus distance curves shown in Ref. [38]. In a recent study by Yesilpinar *et al.* with CuOx tips at liquid nitrogen temperatures ( $T \approx 78\text{ K}$ ) [182] the tip was approached to the Cu(110)- $(2 \times 1)\text{O}$  surface until repulsive features were observed also at AR-Cu sites. Here, it was not possible to further approach the tip to tip-sample distances where a comparable AFM contrast could be observed without risking the occurrence of tip instabilities indicated by an increased dissipation signal. Additionally, the AFM image shown in Fig. 6.7 differs from the images shown in the work of Yesilpinar *et al.* While the shape of atomic-scale features is not altered upon approaching the tip to the surface in Ref. [182], the contrast deviates strongly between the constant-height  $\Delta f$  images shown in Fig. 6.7(b) and (c). A possible explanation for this discrepancy could be a weaker bond between the oxygen atom at the tip apex and the second layer tip atoms in the present work as compared to Ref. [182]. This would result in a decreased lateral stiffness of the tip apex and, hence, could cause similar imaging artifacts as previously observed in case of CO-terminated tips (compare chapter 5).

Interestingly, some CuOx tips showed different atomic-scale contrast in constant-height AFM images at smallest tip-sample distances than it is the case in Fig. 6.7(c). Figure 6.8(a) shows a COFI image of one of these CuOx tips, exhibiting the expected COFI portrait of an O-terminated Cu tip as shown e.g. in Fig. 6.4. To determine the chemical species of the tip-terminating atom a  $F_{\text{SR}}(z)$  spectrum has been measured in the center of a CO molecule adsorbed on Cu(110) as shown in Fig. 6.8(b). The  $F_{\text{SR}}(z)$  spectrum exhibits a minimum of  $F_{\text{SR},\text{min}} = -29\text{ pN}$ , which is slightly lower than the spectrum shown in Fig. 6.3(d).

This tip was again used to record STM and AFM data of a copper oxide domain in order to compare the imaging contrast to previous tip fingerprinting work [38, 180, 182]. Figure 6.8(c) shows an STM image recorded of the Cu(110)- $(2 \times 1)\text{O}$  reconstruction with the CuOx tip at an STM setpoint of  $V_b = -100\text{ mV}$ ,  $\langle I \rangle = -100\text{ pA}$ , which corresponds to  $z = 120\text{ pm}$  above the bare Cu(110) surface. The image presents the same pattern as the STM image recorded with the first CuOx tip [Fig. 6.7(a)] as can be seen by the similarities between Fig. 6.7(a) and Fig. 6.8(c), shown in more detail with line profiles in appendix A.6. To obtain significant contrast in constant-height AFM images the tip was again approached to the sample from the STM imaging

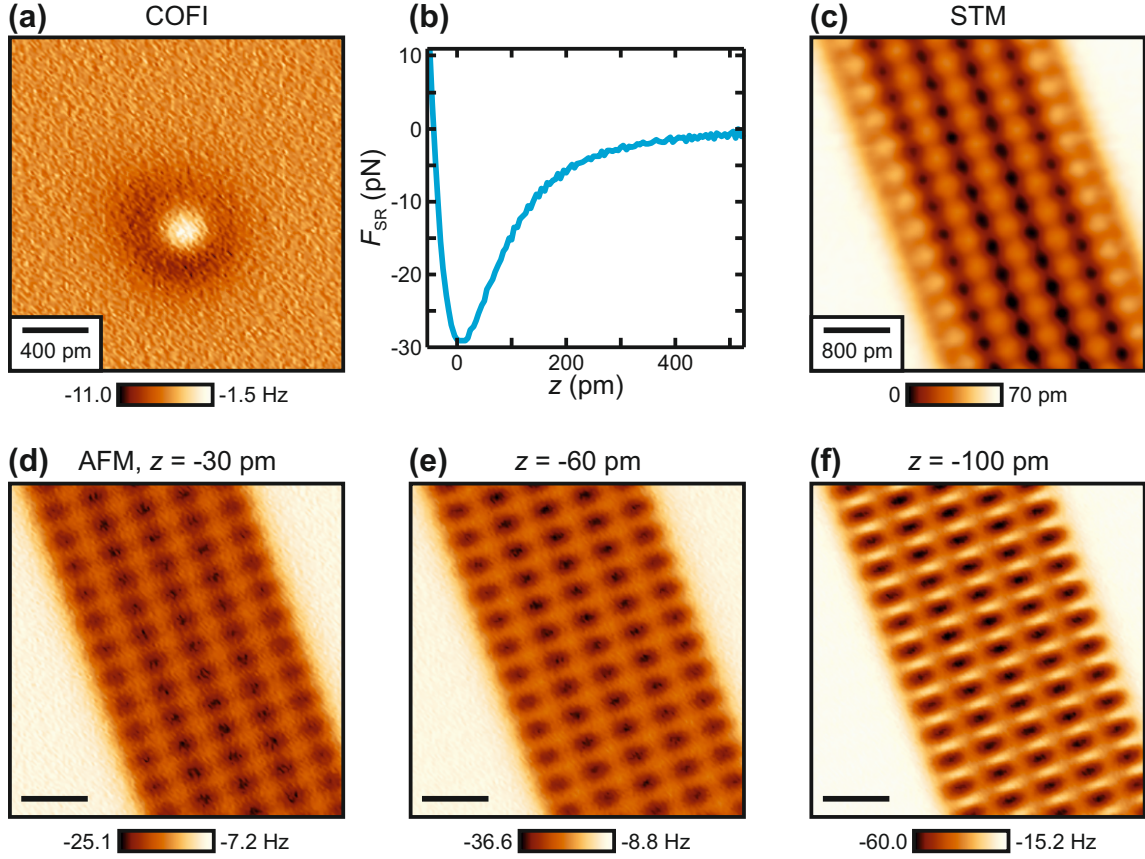


**Figure 6.8.:** STM and AFM data recorded on Cu(110) with a different CuOx tip. (a) COFI image recorded with the CuOx tip on Cu(110), 120 pm closer from the STM setpoint height ( $V_b = -100$  mV,  $\langle I \rangle = -100$  pA) on the bare Cu(110) surface, corresponding to  $z = 0$  pm in (b). (b) Short-range force versus distance spectrum  $F_{SR}(z)$  recorded above the center of a CO molecule. (c) STM image recorded of a Cu(110)-(2 × 1)O domain with this CuOx tip. Imaging parameters:  $V_b = -100$  mV,  $\langle I \rangle = -100$  pA. The image has been processed with a 2 × 2 Gaussian low-pass filter [155]. (d)–(f) Constant-height  $\Delta f$  images of the same area as in (c), recorded at tip-sample distances of  $z = -30$  pm (d),  $z = -60$  pm (e) and  $z = -100$  pm (f), respectively. Scale bars in (d)–(f) are 800 pm long.

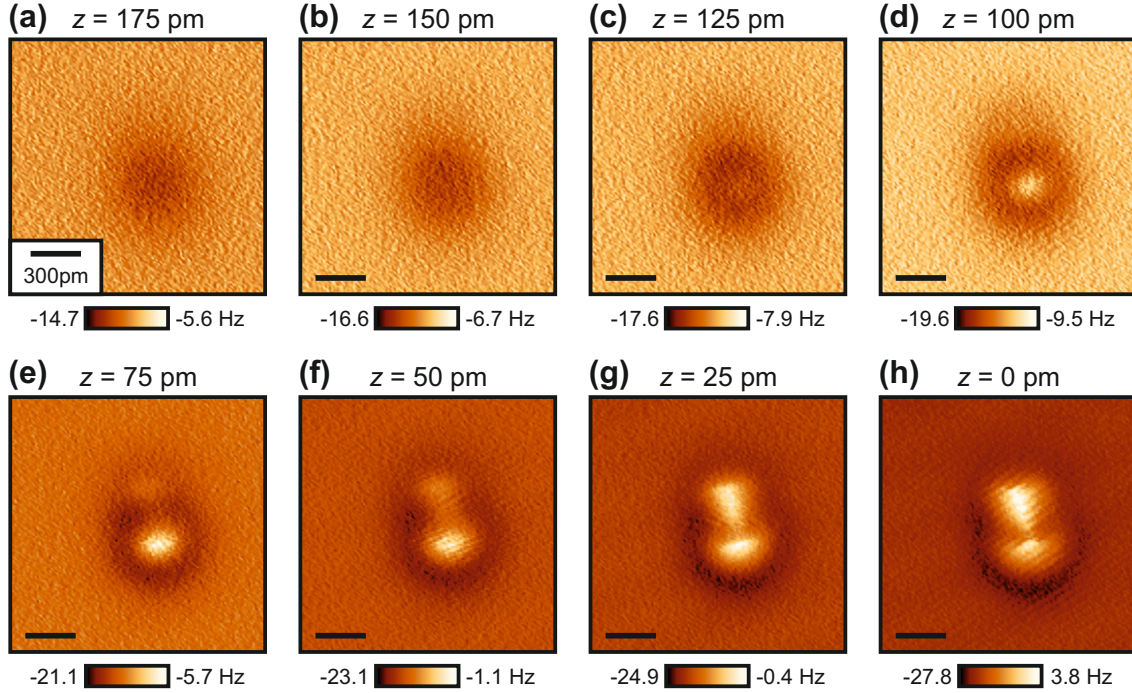
height. Figure 6.8(d)–(f) shows constant-height images of the same surface area as the STM image in Fig. 6.8(c) at different tip-sample distances. At distances where atomic resolution is first observed in the AFM data [Fig. 6.8(d)], the constant-height images are comparable to the data recorded with the first CuOx tip presented in Fig. 6.7(b) and the images shown in Ref. [38, 180, 182], and the contrast increases upon approach [Fig. 6.8(e)]. In this regime, the atomic features that are resolved as depressions (dark) correspond to the AR-Cu atoms [38]. When the tip-sample distance is further reduced, short-range Pauli repulsion between the tip apex and AR-O sites leads to the emergence of increased  $\Delta f$  (bright) at the AR-O positions, analogous to the data recorded with the first CuOx tip, Fig. 6.7(c). The constant-height

image recorded with both tips present, however, drastically different contrast patterns within the oxide domain. While the AR-O atoms appear round in Fig. 6.7(c), superimposing the contributions of AR-Cu atoms, the appearance of the AR-Cu atoms is not altered due to the more localized, repulsive interaction between the tip apex and the AR-O atoms in Fig. 6.8(f). Hence, no signatures of a flexible tip apex like e.g. distortions of the image contrast or a sharpening of features can be identified in the data set recorded with the second CuOx tip. The constant-height image shown in Fig. 6.8(f) closely resembles the images shown in Ref. [182]. On the contrary, it was not possible to further approach the tip to tip-sample distances where a repulsive interaction above the AR-Cu atoms was observed [182].

We conclude that some CuOx tips have a lower lateral stiffness compared to others. This is an unexpected result as O-terminated Cu tips have been generally assumed to be very rigid [38, 180]. A possible explanation for the strong differences in the imaging mechanisms of different CuOx tips could be the atomic composition of the tip apex. While CO-terminated tips are engineered by preparing a single-atom metal tip and controlled pick-up of a CO molecule from a Cu surface (see section 3.3), O-terminated Cu tips (section 6.1) are prepared by poking into copper oxide domains, which leaves the exact geometric and chemical composition unknown. This could result in different bonding strengths and, hence, different lateral stiffnesses between the oxygen atom at the tip apex and the second layer tip atoms. As a consequence, the lateral stiffness of a CuOx tip apex cannot be directly obtained by characterizing the tip apex with COFI and force spectroscopy but needs to be determined by additional tip fingerprinting measurements on copper oxide domains at small tip-sample distances.

### 6.3. Geometric structure of CuOx tip apices with multiple oxygen atoms

The previous section (section 6.2) showcases the direct experimental determination of the geometric structure of O-terminated Cu tips with COFI and force spectroscopy. In previous works that utilized the tip fingerprinting protocol the accompanying calculations of AFM images focused on ideal tip apex structures, where the first atomic layer consists only of single O or Cu atoms [38, 183–186]. Hence, knowledge of tip fingerprinting signatures with CuOx tips with apices consisting of more than one oxygen atom is lacking. This section describes the structural characterization of CuOx tips with multiple O atoms at the tip apex on the example of a two-O-atom tip apex (“dimer” CuOx tip) and its implications for the image contrast in tip fingerprinting



**Figure 6.9.: Height-dependent COFI images of a CuOx tip with multiple oxygen atoms at the tip apex.** COFI images of a CuOx tip with two oxygen atoms at the tip apex as a function of tip-sample distance  $z$ .  $z = 0$  pm defines the distance  $z$  at which the closest approach in the COFI measurement with this tip, which is 150 pm closer from the STM setpoint above the bare Cu(110) surface ( $V_b = -100$  mV,  $\langle I \rangle = -100$  pA). The images have been recorded with zero bias voltage. All scale bars are 300 pm long. Figure adapted from Ref. [169].

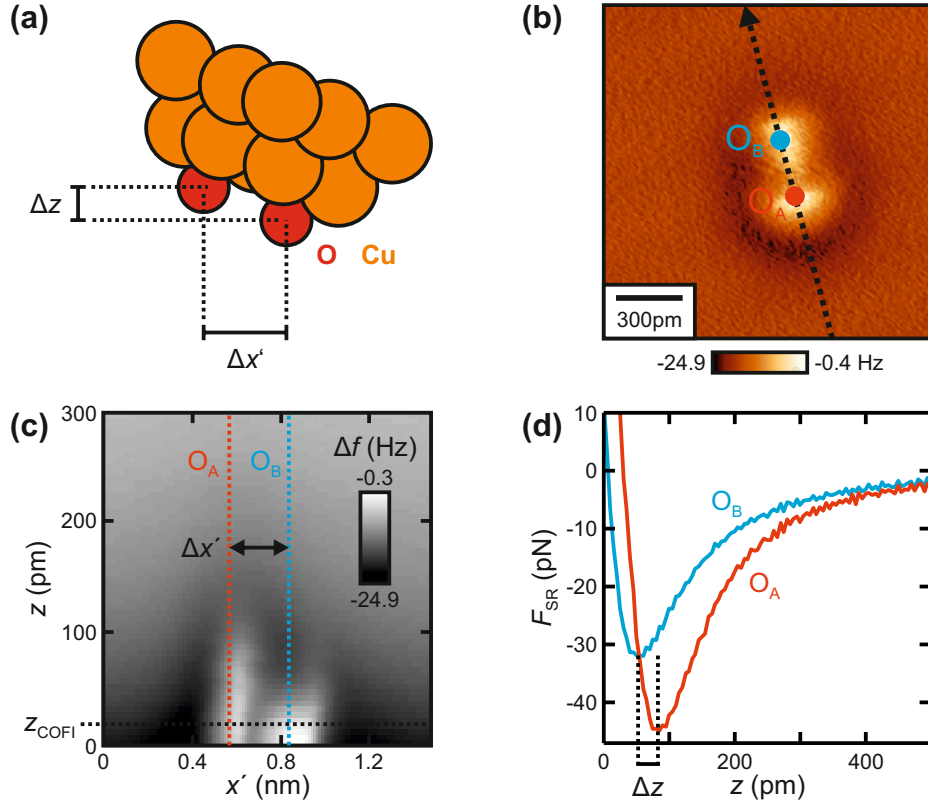
experiments on copper oxide domains.

Figure 6.9 shows COFI images as a function of tip-sample distance  $z$  of the “dimer” CuOx tip. The height  $z = 0$  pm defines the height at which the closest COFI image has been recorded, which is 150 pm closer from the STM setpoint above the bare Cu(110) surface ( $V_b = -100$  mV,  $\langle I \rangle = -100$  pA). Analogous to the COFI images recorded of CuOx tips that have a single O atom at the tip apex, far away from the surface the contrast is governed by long-range van der Waals interaction between the tip and the surface CO molecule, leading to a more negative  $\Delta f$  as seen in Fig. 6.9(a),(b). Upon approach, short-range Pauli repulsion between the CO molecule and each O atom at the tip apex leads to more positive  $\Delta f$  values at the positions of the tip apex atoms resulting in a contrast inversion of the COFI images [Fig. 6.9(c)–(f)]. The COFI images show two bright, repulsive features, which can be interpreted as two individual oxygen atoms at the tip apex. Since the repulsion starts first above the lower O atom, this apex atom is closer to the surface than the upper O atom, which leads to an associated tilt asymmetry of the COFI images. At close distances,

the CO molecule on the surface bends away, which results in mushroom-like COFI images of the “dimer” CuOx tip, as seen in Fig. 6.9(g),(h). Note that the attractive van der Waals background is increased in case of the blunter “dimer” CuOx tip apex: the COFI images in Fig. 6.4(d) and Fig. 6.9(d) show a similar contrast, but the  $\Delta f$  values are more negative in the case of the blunter “dimer” CuOx tip as compared to the CuOx tip that has a single O atom at the tip apex.

In the following, COFI and force spectroscopy data will be used to determine the geometric structure of the “dimer” CuOx tip apex, i.e. the lateral  $\Delta x'$  and vertical  $\Delta z$  offsets between the tip apex oxygen atoms as sketched in Fig. 6.10(a). As shown in the COFI image in Fig. 6.10(b) the lower oxygen atom is defined as  $O_A$  and the upper atom is defined as  $O_B$ . Figure 6.10(c) displays a vertical cut  $\Delta f(x', z)$  extracted along the dashed line in Fig. 6.10(b) from a three-dimensional set of COFI images recorded with this tip. From this vertical cut the lateral distance between the two O atoms at the tip apex has been determined to be  $\Delta x' \approx 250$  pm. However, since the lateral deflection of the CO molecule leads to an increased lateral size of atomic features in AFM images [18], the value of  $\Delta x'$  determined here defines an upper boundary for the lateral offset between the two tip apex oxygen atoms.

Figure 6.10(d) shows  $F_{SR}(z)$  spectra recorded above the two O atoms, respectively. The short-range force was obtained by subtracting a background  $\Delta f(z)$  curve recorded above the bare Cu(110) surface from the spectra recorded above the two tip apex atoms and subsequent force deconvolution [78]. From the two spectra short-range force minima of  $F_{SR,\min} = -45$  pN (atom  $O_A$ ) and  $F_{SR,\min} = -32$  pN (atom  $O_B$ ) were obtained. These values are lower compared to the values for CuOx tips that have a single O atom at the tip apex (Fig. 6.5), which can be attributed to the combined interaction of the two apex atoms with the CO molecule that cannot be separated using the “on - off” subtraction method. To estimate the vertical offset between the two tip apex oxygen atoms the relative  $z$  positions of the short-range force minima  $F_{SR,\min}$  can be compared. A similar concept was previously used by Schuler *et al.* in Ref. [82] to determine the adsorption geometry of organic molecules on Cu(111). It is assumed that the interaction of the tip with different adsorbate atoms shows a similar distance dependence. Hence, a two-dimensional map of the relative adsorption height can be determined by extracting for different lateral positions  $(x, y)$  the height  $z^*(x, y)$  where the short-range frequency shift  $\Delta f_{SR}(x, y, z)$  is minimal ( $z^*$  method, see section 2.2.3) [82]. Based on this method, the vertical offset between the two oxygen atoms was extracted from the  $F_{SR}(z)$  spectra in Fig. 6.10(d) to be  $\Delta z = 35$  pm. From the values obtained for  $\Delta x'$  and  $\Delta z$  the distance between the two O atoms is found to be  $d = 252$  pm, which is close to the nearest-neighbor



**Figure 6.10.: Atomic structure determination of the “dimer” CuOx tip apex.** (a) Schematic of the “dimer” CuOx tip apex with definitions of lateral  $\Delta x'$  and vertical offsets  $\Delta z$  between the two oxygen atoms at the tip apex. (b) COFI image of the “dimer” CuOx tip, recorded at a tip-sample distance of  $z = 25$  pm. (c)  $\Delta f(x', z)$  extracted along the dashed line in (b) from a three-dimensional data set of COFI images of the “dimer” CuOx tip. Vertical, dashed lines mark the positions of the two O atoms ( $O_A$  and  $O_B$ ) at the tip apex. The COFI image in (a) has been recorded at  $z_{\text{COFI}}$ . (d) Short-range force vs. distance  $F_{\text{SR}}(z)$  spectra recorded above the two O atoms, positions marked in (b) and (c), respectively. Figure partly adapted from Ref. [169].

distance of Cu,  $d_{\text{nm}} = 255$  pm [107].

After the tip was characterized with COFI and force spectroscopy, STM and AFM images of the Cu(110)-(2 × 1)O added-row reconstruction were recorded for tip fingerprinting as done in Ref. [38]. The STM feedback image shown in Fig. 6.11(a) is similar to images recorded with CuOx tips that have a single O atom at the tip apex as shown e.g. in Fig. 6.2(b). Interestingly, the features in the STM image recorded with the “dimer” CuOx tip appear with a slightly lower corrugation of about 20 pm compared to the corrugation of 30 pm in the STM image recorded with the single-atom CuOx tip [Fig. 6.2(b)], which could be possibly caused by the blunter apex of the “dimer” CuOx tip. To obtain significant AFM contrast the tip was again approached towards the surface from the STM imaging height. Note that the tip had to be moved closer

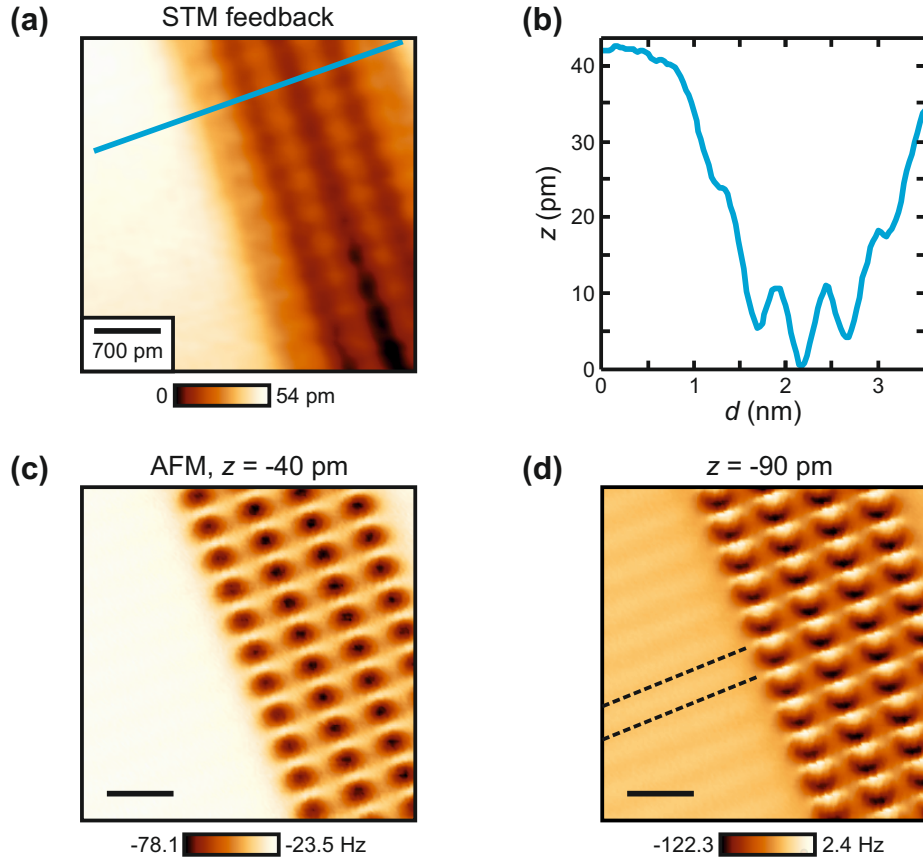


**Figure 6.11.: STM and AFM images recorded of a copper oxide domain with the “dimer” CuOx tip.** (a) STM image recorded of a Cu(110)-(2 × 1)O domain with the “dimer” CuOx tip that has been characterized with COFI and force spectroscopy, see Fig. 6.9 and Fig. 6.10. Imaging parameters:  $V_b = -100$  mV,  $\langle I \rangle = -100$  pA. The image has been processed with a  $2 \times 2$  Gaussian low-pass filter and  $z$ -drift corrected [155]. (b) Line profile extracted along the blue line in (a). (c) and (d) Constant-height  $\Delta f$  images of the same area as in (a), recorded 190 pm (c) and 240 pm (d) closer than the STM image in (a), corresponding to a distance  $z = -40$  pm (c) and  $z = -90$  pm (d), respectively. Dashed lines in (f) mark atomic rows of the Cu(110) surface lattice. All scale bars are 700 pm long. Figure adapted from Ref. [169].

to the surface than the single O atom tip. This can be attributed to the additional tunneling current contribution from the second O atom at the tip apex, which leads to a greater tip-sample distance at the same STM feedback settings [93, 184, 186].

Interestingly, the atomic features that are resolved first are emerging depressions within the copper oxide domain as shown in Fig. 6.11(c), which can be attributed to attractive interaction between the tip and the AR-Cu atoms [38]. This appearance of the Cu(110)-(2 × 1)O added-row reconstruction is very similar to images that were recorded with tips that had a single O atom at the apex shown e.g. in Fig. 6.8(d),(e). Only when the tip further approaches the sample, Fig. 6.11(d), the images exhibit

an asymmetry due to the multi-atom tip apex that is clearly distinct from images recorded with single-atom CuOx tips. As compared to Fig. 6.8(f) the bright features that arise from Pauli repulsion between the tip and the AR-O atoms show a clear asymmetry. Analogously, a similar asymmetry was recently reproduced also by Yesilpinar *et al.* in Ref. [182] on the same sample system at tip-sample distances, where Pauli repulsion dominates the tip-sample interaction. However, the determination of the exact tip structure based on the tip fingerprinting images of the copper oxide domain would require theoretical modeling of such a “dimer” CuOx tip, which has so far not been pursued. Note that in Fig. 6.11(d) the atomic rows of the Cu(110) surface, highlighted by the dashed lines, are already resolved as dark lines meeting the copper oxide domain at the AR-O sites [38].

## 6.4. Discussion

The above findings illustrate possible complications in tip characterization with images of the copper oxide domains which show atomic resolution: simply because individual atoms of the oxide can be resolved does not mean that the tip apex can be accurately determined even when compared to simulated data. One attribute of the COFI method is to acquire data at a tip-sample distance at which there is significant repulsive interaction between the tip and the adsorbate. This results in a very detailed and complete picture of the apex atoms responsible for AFM imaging. Of course, the effect of multiple atoms at the tip apex will also be seen on the oxide domain when acquiring data at smaller tip-sample distances [182]. However, it is more straightforward to directly determine the geometric positions of the apex atoms with an image of a point-like feature (in this case, a single CO molecule) versus that of a lattice. This is especially true for instances in which the spacing between apex atoms on the tip is comparable to that of the lattice as in the example of the “dimer” CuOx tip discussed in section 6.3.

This chapter presented an efficient *in-situ* characterization of CuOx tips via the COFI technique and force spectroscopy. COFI images of CuOx tips terminating in a single O atom exhibit a circularly-symmetric repulsive feature very similar to images of CO-terminated tips on Cu(111) [16] and Cu(110). Via force spectroscopy curves recorded with these single-atom CuOx tips on CO/Cu(110) short-range force minima ranging from  $-15$  pN to  $-30$  pN were measured. These are similar to data obtained for CO tips, which illustrates the decreased reactivity of these tips as compared to bare metal tips [16, 29]. While AFM images of the Cu(110)-(2 × 1)O added-row reconstruction recorded with a tip terminating in two O atoms at tip-sample

## **6 *In-situ* characterization of O-terminated Cu tips based on the COFI method**

distances at which atomic resolution appears first in constant-height images showed similar features as tips terminating in only one O atom, the COFI image directly resolved the two-atom tip apex.

Although tip characterization with COFI and force spectroscopy provides detailed information about the geometric configuration and chemical species of the tip apex atoms, this approach does not allow determination of the lateral stiffness of the tip apex. In existing literature it is assumed that CuOx tips present a much stiffer tip apex than CO-terminated tips [38, 180]. As shown in section 6.2.2 signatures of a flexible tip apex have been identified in tip fingerprinting images recorded with certain single-atom CuOx tips at tip-sample distances, where Pauli repulsion between the AR-O atoms and the tip apex dominates the AFM contrast. The image features recorded with these tips are clearly different from images recorded with potentially stiffer CuOx tips, which allows qualitative determination of the lateral stiffness of single-atom CuOx tips. A quantitative determination of the lateral stiffness of CuOx tip apices would require additional extensive simulations of the imaging contrast on copper oxide domains with varying lateral stiffnesses of the tip apex, which is possible with mechanical models to simulate AFM images such as the probe particle method introduced in chapter 5. In context of this observation, CuOx tips should be characterized by a combination of COFI, force spectroscopy and tip fingerprinting experiments to unambiguously determine the chemical and structural composition as well as the lateral stiffness of the tip apex. Knowledge of these properties is of crucial importance especially if the tips are used for experiments that are accompanied by theory. In conclusion, the approach suggested here provides an efficient way of CuOx tip characterization.

## 7. Summary and outlook

This thesis presents high-precision atomic force microscopy experiments with different types of atomically-characterized tips. The atomic interaction mechanisms that are relevant for the AFM contrast in measurements with each tip apex termination have been analyzed in detail as a function of the tip-sample distance.

In chapter 4, experiments with a single-atom metal tip on the ionic  $\text{CaF}_2(111)$  surface were presented. Previous AFM experiments were conducted at tip-sample separations where the tip interacts strongly with the surface with poorly-characterized tips, leading to strong sample perturbations [14, 15, 19, 20, 24]. Non-invasive imaging of a surface requires data acquisition in a weak tip-sample interaction regime, or in other words detection of piconewton and sub-piconewton forces. We chose the ionic  $\text{CaF}_2(111)$  surface as a reference system as it is a well-known sample that lacks charge inversion symmetry, making it ideal to study the electrostatic tip-sample interaction. Additionally, by characterizing the atomic configuration of single-atom metal tips with the COFI method, the tip apex termination can be determined and controlled at the atomic scale. This has clear advantages when imaging in a regime where electrostatic interaction dominates, as single-atom metal tips present a well-defined electric field configuration. Due to the Smoluchovski effect [138], a metal tip presents an electric dipole with its positive pole pointing towards the surface. This tip-sample system has allowed for successful benchmarking of high-precision AFM measurements at sub-piconewton force contrasts in a deep non-contact regime.

Following the considerations of Lennard-Jones and Dent [149], the distance dependence of the electric field outside an ionic crystal was derived. The electric field decays exponentially with distance, where the decay length depends only on the crystal lattice constant. In case of the  $\text{CaF}_2(111)$  surface this results in a decay length of  $\lambda = 53.2 \text{ pm}$ . A calculation to simulate the electrostatic tip-sample interaction between the single-atom metal tip and the  $\text{CaF}_2(111)$  surface was developed. The sample atoms were represented by single, fixed point charges and the tip apex was represented by a single, positive point charge.

The calculation was compared to atomically-resolved experimental data of  $\text{CaF}_2(111)$

## 7 Summary and outlook

---

recorded with the single-atom metal tip. In this way, atomic species could be assigned to high-symmetry sites in the experimental images based on the electrostatic interaction of the charged tip apex and the surface ions. The atoms of the surface  $F^-$  layer appear most attractive and the  $Ca^{2+}$  atoms appear least attractive in the constant-height images. The atoms of the lower  $F^-$  layer correspond to the sites of intermediate contrast. The agreement between the electrostatic calculation and the experimental data was quantified via the relative quadratic deviation over one surface period between the measured and calculated line profiles. This method has yielded an accuracy of 98.1 %, which demonstrates that the short-range interaction of a single-atom metal tip with the  $CaF_2(111)$  is determined almost entirely by the electrostatic tip-sample interaction. Moreover, the atomic AFM contrast was found to decay exponentially with distance with a decay length  $\lambda_{\text{exp}} = (53 \pm 3) \text{ pm}$ , in good agreement to the predicted decay length of the electric field of  $\lambda = 53.2 \text{ pm}$ .

For tip-sample distances larger than  $z = 500 \text{ pm}$  atomic contrasts in the mHz regime, corresponding to fN electrostatic force contrasts, were observed in the experimental data. This atomic contrast could not be observed in unprocessed constant-height  $\Delta f$  images. A precise calculation of the experimental noise contributions identified the detector noise as the dominant contribution in the measurements. The detector noise can be effectively diminished by a reduction of the acquisition bandwidth or by low-pass filtering in real space after data acquisition. In this way, mHz atomic contrast, corresponding to sub-piconewton force contrasts, could be made visible also in the experimental constant-height images.

Furthermore, due to the high precision in the  $\Delta f$  measurement small but measurable asymmetries could be identified in the experimental constant-height images. These asymmetries were reproduced by the electrostatic calculation when considering second layer tip atoms. The relative magnitude of the additional contributions and their lateral shifts were directly obtained from the experimental COFI image. In this way, the theoretical description of the tip apex was optimized and the agreement between the electrostatic calculation and the experimental data improved to 99.5 %.

With increased sensitivity to sub-piconewton forces, further effects such as a polarization of the tip apex in the electric field of the sample or tip-induced relaxations of sample atoms could eventually affect the measured signal. The additional force on the metal tip due to a polarization of the front atom has been found to be negligible compared to the electrostatic force. Furthermore, the relaxation of a surface  $F^-$  ion due to the attractive force caused by the charged tip apex has been calculated as a function of tip-sample distance. At the closest tip-sample approach the relaxation was found to be the very small magnitude of 1.5 pm.

---

Due to their chemical reactivity single-atom metal tips cannot be approached to a tip-sample distance regime where the tip interacts with the sample via short-range Pauli repulsion. In chapter 5, measurements on the  $\text{CaF}_2(111)$  sample performed with a CO-terminated tip were presented. It was previously found that the tip-sample interaction of a CO tip with a NaCl surface is dominated by the electrostatic interaction for distances larger than 500 pm and Pauli repulsion at closer separations [35]. Indeed, when probing the  $\text{CaF}_2(111)$  surface as a function of tip-sample distance, strong variations in the AFM contrast patterns were observed. At large tip-sample distances the images present three high-symmetry sites analogously to the constant-height images recorded with the single-atom metal tip that are presented in chapter 4. When approaching to the surface, the contrast changes drastically. First, a sharpening of features can be observed, which is followed by a complete change of the contrast. At closest tip-sample distance the surface appears as a hexagonal arrangement of bright spheres.

In order to obtain a quantitative understanding of the tip-sample interactions that result in the rich contrast features observed experimentally, simulations with the probe particle model were performed. The PPM is a mechanical model to calculate AFM images with functionalized tips, which considers the lateral deflection of the tip apex in the tip-sample force field [22]. A modified version of the PPM was introduced, where the contribution of Pauli repulsion is obtained by calculating the overlap of the electron densities of tip and sample as obtained from DFT. Additionally, the electrostatic interaction is obtained by a convolution between the electrostatic sample potential and the tip's electron density that were obtained independently from DFT calculations. The images calculated with this model could reproduce the experimentally observed contrast patterns at all accessed tip-sample distances.

Moreover, to deduce which tip-sample interaction dominates the AFM contrast the individual contributions to the total tip-sample force were decomposed from the PPM data. It was found that the contrast can be explained almost entirely by the electrostatic interaction for tip-sample distances larger than  $z = 400$  pm. In this distance regime, van der Waals attraction and Pauli repulsion effectively cancel out each other. Additionally, these two contributions decay faster than the electrostatic interaction, which leaves the latter as the dominant contribution. If the tip-sample distance is reduced, Pauli repulsion eventually becomes the dominant tip-sample interaction. Furthermore, the increased lateral component in the tip-sample force results in sizable CO bending effects, which results in the above-mentioned strong variations in the AFM contrast patterns. For comparison, the modified PPM calculation was com-

## 7 Summary and outlook

---

pared to the standard PPM approach that is based on Lennard-Jones potentials [22]. This calculation yielded similar results but reproduced the experimental contrast with less precision.

Furthermore, the electrostatic imaging regime was analyzed in more detail. The experimental data obtained with the CO tip was compared to the electrostatic calculation that was developed in context of chapter 4. The calculation reproduces the experimental contrast with an accuracy of 99.6% in this regime. This agreement illustrates that the electric field of CO tips can be approximated with a single negative point charge when the electrostatic interaction between a CO tip and a defect-free ionic lattice is considered. Additionally, when comparing the data recorded with the positively-terminated metal tip presented in chapter 4 to the data collected with the negatively-terminated CO tip, one finds a contrast inversion due to the opposite effective apex charges of the two tip terminations.

In chapter 6, the characterization of O-terminated Cu tips based on the COFI method and force spectroscopy was presented. These CuOx tips show comparable spatial resolution to CO tips, but have a much higher lateral stiffness of the tip apex. The interaction of CuOx tips with individual CO molecules adsorbed on Cu(110) during COFI analysis was discussed in detail. Approaching the surface, the tip interacts with the CO adsorbate mainly via van der Waals attraction. If the tip-sample distance is reduced, the contrast inverts due to Pauli repulsion between the tip and the CO molecule. At closest approach, the lateral deflection of the CO molecule leads to artifacts expressed as discontinuities in the center of the COFI images. The tip-CO interaction was further characterized by analyzing the short-range force minima measured above the CO adsorbate [29]. Short-range force minima ranging from  $-15$  pN to  $-30$  pN were observed, which illustrates the reduced reactivity as compared to single-atom metal tips that generally show force minima lower than  $-130$  pN. Furthermore, the interaction of CuOx tips was compared to the interaction of CO tips with CO/Cu(110). It was found that both types of tip terminations show a comparable interaction with the CO adsorbates.

Next, the CuOx tips were used to image the Cu(110)-(2 × 1)O reconstruction. The imaging contrast on these copper oxide domains was used as a tip fingerprint in existing literature [38]. All tips have shown comparable AFM contrast at tip-sample distances where the short-range interaction is purely attractive. Interestingly, it was found that some tips show signatures of a flexible tip apex at close tip-sample distances, where the tip interacts via Pauli repulsion with the surface oxygen atoms. This information is not accessible directly from the COFI characterization.

---

Finally, the characterization of a CuOx tip with two oxygen atoms at the tip apex was reported. The two atoms were observed as two bright features in COFI images of this “dimer” CuOx tip at close tip-sample distances. The structural composition of the tip apex was determined from the COFI and force spectroscopy data. A lateral offset of  $\Delta x' = 250$  pm and a vertical offset of  $\Delta z = 35$  pm between the two O atoms was determined. To characterize the imaging properties with this tip the Cu(110)–(2 × 1)O reconstruction was imaged for tip fingerprinting. When approaching the surface it was found that the surface is imaged with a symmetric AFM contrast pattern, very similar to images recorded with CuOx tips that have a single O apex atom. Only when approaching the surface to a distance where the tip interacts with the surface O atoms via Pauli repulsion was the inherent tip apex asymmetry visible in the AFM images. Based on the experimental observations presented within chapter 6 it was proposed that the CuOx tips should be characterized by a combination of COFI, force spectroscopy and tip fingerprinting measurements.

Recapitulating the findings within this thesis it can be clearly stated that the precision of AFM experiments strongly benefits from the use of atomically-characterized tips. On the one hand, these tips are a prerequisite for conducting high-precision experiments in a well-controlled manner, which eventually allows for atomic resolution in a deep non-contact regime with sub-piconewton force contrasts. Specifically, experimentally characterizing the tip apex has opened the possibility to atomically resolve the electrostatic signature of a metal tip apex. In future studies, this concept could be potentially transferred to probe the electrostatic properties of metal clusters or nanoparticles with atomic precision [127]. For example, these properties have been shown to affect the toxicity of gold nanoparticles [193], as well as the delivery efficiency of mRNA-based vaccines in case of lipid nanoparticles [3, 194].

On the other hand, usage of atomically-characterized and functionalized tips ensures repeatability and significantly facilitates a quantitative theoretical description of physical mechanisms observed in AFM experiments. The AFM’s capability of sensing a single electric charge [195–201] was recently applied in studies of previously inaccessible nanoscale processes like the measurement of charge transfer between two molecules [202], determination of the reorganization energy upon charging [203] and imaging of molecular orbitals with sub-molecular resolution on a bulk insulator surface [204, 205]. Furthermore, the sub-molecular imaging capabilities of AFM using functionalized tips were lately combined with the ability to control the charge state of an isolated molecular adsorbate on an insulator surface [206]. In this context, the determination of adsorption geometries of molecules on insulator surfaces by AFM using

## 7 Summary and outlook

---

functionalized tips requires a thorough characterization of the atomic-scale imaging mechanisms of these tips on bulk insulators [139]. In particular the  $\text{CaF}_2(111)$  surface, which was studied in detail within this thesis, is a promising substrate candidate for room-temperature molecular anchoring required for future applications of nano-electronic devices [207–209].

# A. Appendix

## A.1. MATLAB code of the electrostatic simulation introduced in chapter 4

This section shows the MATLAB code of the electrostatic model employed for the calculation of the electrostatic tip-sample interaction on  $\text{CaF}_2(111)$ . As the calculation of the electrostatic potential of the model crystal is computational-intensive, the model is split into two parts. The first part calculates the electrostatic potential  $V(\mathbf{r})$  as defined in eq. (4.11), which can then be saved for later re-use in order to save computing time. In the second part, the force acting on a charged tip apex and the resulting frequency shift values are calculated from the potential obtained in part 1.

### A.1.1. Calculation part 1

```
1 % Simulation of the Electrostatic interaction between a tip
2 % and the CaF2(111) surface:
3 %
4 % define the CaF2 lattice:
5 %
6 % lattice constant:
7 a0 = 0.5463e-9;
8 % net charges of the surface atoms:
9 qCa = 1.73;
10 qF = -0.865;
11 % basis vectors in the standard system:
12 BCa = [0; 0; 0];
13 BF1 = [a0/4; a0/4; a0/4];
14 BF2 = -BF1;
15 % surface unit cell vectors in the standard coordinate system:
16 A1 = [a0/2; a0/2; 0];
17 A2 = [0; a0/2; a0/2];
```

## A Appendix

```
18 % displacement to the next layer in standard system:
19 A3 = [a0/2; 0; a0/2];
20 % unit cell vectors in standard system:
21 e1 = [1; 0; 0];
22 e2 = [0; 1; 0];
23 e3 = [0; 0; 1];
24 % matrices for rotating the coordinate system:
25 RotZ = [cos(pi/4) -sin(pi/4) 0; sin(pi/4) cos(pi/4) 0; 0 0 1];
26 alpha = pi / 2 - atan(1 / sqrt(2));
27 RotXnew = [(0.5 * (1 - cos(alpha)) + cos(alpha)) (0.5 * (1 - cos(alpha))) (1/
           sqrt(2) * sin(alpha));
28             (0.5 * (1 - cos(alpha))) (0.5 * (1 - cos(alpha)) + cos(alpha))
           (-1/sqrt(2) * sin(alpha));
29             (-1/sqrt(2) * sin(alpha)) (1/sqrt(2) * sin(alpha)) cos(alpha)];
30 % total rotation:
31 Rot111 = RotXnew * RotZ;
32 % new unit cell vectors:
33 E1 = Rot111 * e1;
34 E2 = Rot111 * e2;
35 E3 = Rot111 * e3;
36 % matrix for coordinate transformation:
37 Mtrans = [E1(1) E1(2) E1(3); E2(1) E2(2) E2(3); E3(1) E3(2) E3(3)];
38 % surface unit cell vectors in the new coordinate system:
39 a1 = Mtrans * A1;
40 a2 = Mtrans * A2;
41 a3 = Mtrans * A3;
42 % basis vectors in the rotated coordinate system:
43 bCa = Mtrans * BCa;
44 bF1 = Mtrans * BF1;
45 bF2 = Mtrans * BF2;
46 % In order to obtain a finite crystal that shows the full symmetry of the
47 % lattice, we use a different basis than the original three atomic basis.
48 % We now use 1 Ca atom surrounded by 6 F atoms. The F atoms are shared by
49 % three unit cells. Therefore they have only 1/3 of their original charge
50 % (see the factor when the potential is calculated). In this way we end up
51 % again with a charge-neutral CaF2 "molecule" that also has the full
52 % symmetry of the lattice.
53 bF3 = bF1;
54 bF3(1) = -bF3(1);
```

## A.1 MATLAB code of the electrostatic simulation introduced in chapter 4

```
55 bF4 = -bF3;
56 bF5 = 1/3 .* (a1 - 2 .* a2);
57 bF5(3) = bF1(3);
58 bF6 = -bF5;
59 %
60 % calculate the electrostatic potential:
61 %
62 % number of unit cells:
63 % choose mod(Ncells-1, 3) = 0 to have a Ca in the middle of the crystal.
64 Ncells = 511;
65 % number of layers:
66 NL = 1;
67 % define the positions of the surface atoms:
68 positionCa = zeros(NL * (Ncells * Ncells + Ncells) / 2, 3);
69 positionF1 = zeros(NL * (Ncells * Ncells + Ncells) / 2, 3);
70 positionF2 = zeros(NL * (Ncells * Ncells + Ncells) / 2, 3);
71 positionF3 = zeros(NL * (Ncells * Ncells + Ncells) / 2, 3);
72 positionF4 = zeros(NL * (Ncells * Ncells + Ncells) / 2, 3);
73 positionF5 = zeros(NL * (Ncells * Ncells + Ncells) / 2, 3);
74 positionF6 = zeros(NL * (Ncells * Ncells + Ncells) / 2, 3);
75 % counter to fill the position vectors:
76 count = 1;
77 % calculate the atomic positions for a triangular crystal, which has the
78 % same symmetry as the crystal:
79 for lay = 1 : NL
80     for L = 1 : Ncells
81         for m = 1 : (Ncells - L) + 1
82             for K = 1 : 3
83                 positionCa(count, K) = bCa(K) + (L-1) * a1(K) + (m-1) * a2(K)
84                     - (lay-1) * a3(K);
85                 positionF1(count, K) = bF1(K) + (L-1) * a1(K) + (m-1) * a2(K)
86                     - (lay-1) * a3(K);
87                 positionF2(count, K) = bF2(K) + (L-1) * a1(K) + (m-1) * a2(K)
88                     - (lay-1) * a3(K);
89                 positionF3(count, K) = bF3(K) + (L-1) * a1(K) + (m-1) * a2(K)
90                     - (lay-1) * a3(K);
91                 positionF4(count, K) = bF4(K) + (L-1) * a1(K) + (m-1) * a2(K)
92                     - (lay-1) * a3(K);
```

## A Appendix

```
88         positionF5(count, K) = bF5(K) + (L-1) * a1(K) + (m-1) * a2(K)
89         - (lay-1) * a3(K);
90         positionF6(count, K) = bF6(K) + (L-1) * a1(K) + (m-1) * a2(K)
91         - (lay-1) * a3(K);
92     end
93     count = count + 1;
94 end
95 clear count L lay
96 % We want a circular crystal. For this we calculate the radius of the inner
97 % circle of a triangle with equal side lengths. This is the maximum radius
98 % of our circular crystal 'Rmax'. We set our potential cube around the
99 % center of the model crystal 'Center'.
100 % the maximum threshold distance is the radius of the inner circle of the
101 % triangle with side length Ncells * a1:
102 Rmax = sqrt(3)/6 * Ncells * a1(1);
103 % The center of the crystal is defined by:
104 Center = ((Ncells - 1) / 3 .* (a1 + a2))';
105 % Calculate a Matrix 'distanceCa' in which each row contains the distance
106 % vector between the center and each Ca atom:
107 % https://stackoverflow.com/questions/5342857/how-to-subtract-a-vector-from-
108     each-row-of-a-matrix
109 distanceCa = zeros(size(positionCa));
110 distanceCa(:, 1) = positionCa(:, 1) - Center(1);
111 distanceCa(:, 2) = positionCa(:, 2) - Center(2);
112 distanceCa(:, 3) = positionCa(:, 3) - Center(3);
113 % Calculate the square of the distance, i.e. the square of the norm of each
114 % row of 'distanceCa':
115 % https://stackoverflow.com/questions/7209521/vector-norm-of-an-array-of-
116     vectors-in-matlab
117 distSquare = sum(distanceCa.^2, 2);
118 % Delete the position of every corresponding basis atom, if distSquare is
119 % larger than the square of the threshold 'Rmax'. Use logical indexing to
120 % access the correct rows of the matrix:
121 % https://de.mathworks.com/matlabcentral/answers/105768-how-can-i-delete-
122     certain-rows-of-a-matrix-based-on-specific-column-values
123 RmaxSquare = Rmax^2;
124 Condition = distSquare - RmaxSquare > 0;
```

## A.1 MATLAB code of the electrostatic simulation introduced in chapter 4

```
122 positionCa(Condition, :) = [];  
123 positionF1(Condition, :) = [];  
124 positionF2(Condition, :) = [];  
125 positionF3(Condition, :) = [];  
126 positionF4(Condition, :) = [];  
127 positionF5(Condition, :) = [];  
128 positionF6(Condition, :) = [];  
129 clear RmaxSquare distSquare distanceCa Condition  
130 % calculate the Coulomb potential in a certain area defined by Nx, Ny, Nz and  
    'stepsize':  
131 Nx = 200;  
132 Ny = Nx;  
133 Nz = 200;  
134 Vc = zeros(Nx, Ny, Nz);  
135 % set the stepsize for calculation:  
136 stepsize = 5E-12;  
137 qe = 1.6022e-19;  
138 epsilon0 = 8.85e-12;  
139 % Calculate the offset vector 'rOff' to center the frame on the model crystal  
    :  
140 % The center of a triangular crystal is given as:  
141 rOff = (Ncells - 1) / 3 .* (a1 + a2);  
142 % set the zero-point of the calculation to the top F- layer, which is 79pm  
    above the Ca layer:  
143 rOff(3) = bF1(3);  
144 % We calculate the potential in a (Nx*stepsize) x (Ny*stepsize) frame  
    centered on the crystal.  
145 % Therefore we need to subtract half of the length of the frame in x and y  
146 % direction respectively:  
147 rOff(1) = rOff(1) - (Nx * stepsize / 2);  
148 rOff(2) = rOff(2) - (Ny * stepsize / 2);  
149 % Calculation of the Coulomb potential 'Vc':  
150 for K = 1 : Nx + 1  
151     for l = 1 : Ny + 1  
152         for m = 1 : Nz + 1  
153             % calculate the position vector r around the center of the model  
                crystal surface:  
154                 r = stepsize * [K-1 l-1 m-1] + rOff';  
155             % calculate the distance between r and each atom and from that
```

## A Appendix

```
156     % the electrostatic potential:
157     RCa = sqrt( (positionCa(:, 1) - r(1)).^2 + (positionCa(:, 2) - r
158             (2)).^2 + (positionCa(:, 3) - r(3)).^2 );
159     RF1 = sqrt( (positionF1(:, 1) - r(1)).^2 + (positionF1(:, 2) - r
160             (2)).^2 + (positionF1(:, 3) - r(3)).^2 );
161     RF2 = sqrt( (positionF2(:, 1) - r(1)).^2 + (positionF2(:, 2) - r
162             (2)).^2 + (positionF2(:, 3) - r(3)).^2 );
163     RF3 = sqrt( (positionF3(:, 1) - r(1)).^2 + (positionF3(:, 2) - r
164             (2)).^2 + (positionF3(:, 3) - r(3)).^2 );
165     RF4 = sqrt( (positionF4(:, 1) - r(1)).^2 + (positionF4(:, 2) - r
166             (2)).^2 + (positionF4(:, 3) - r(3)).^2 );
167     RF5 = sqrt( (positionF5(:, 1) - r(1)).^2 + (positionF5(:, 2) - r
168             (2)).^2 + (positionF5(:, 3) - r(3)).^2 );
169     RF6 = sqrt( (positionF6(:, 1) - r(1)).^2 + (positionF6(:, 2) - r
170             (2)).^2 + (positionF6(:, 3) - r(3)).^2 );
171     Vvec = (qe / (4 * pi * epsilon0)) .* ((qCa ./ RCa) + 1/3 .* ((qF
172             ./ RF1) + (qF ./ RF2) + (qF ./ RF3) + (qF ./ RF4) + (qF ./ RF5
173             ) + (qF ./ RF6)));
174     Vc(K, l, m) = sum(Vvec);
175     end
176     end
177     dummy = K
178 end
179 clear dummy Vvec RCa RF1 RF2 r K l m
180 clear RF3 RF4 RF5 RF6
181 SimZpotential = stepsize * (0 : Nz);
182 SimZpotential = SimZpotential';
183 % constant height slice of the Coulomb potential:
184 figure;
185 imagesc(Vc(:, :, 100));
186 axis equal tight xy; colorbar
```

### A.1.2. Calculation part 2

```

1 %
2 %
3 %
4 %%%%%%%%%% part II of the simulation, taking into account the
   oscillation amplitude:
5 %
6 %
7 %
8 %%%% calculate the force and frequency shift of the tips in the electric
9 %%%% field of the sample crystal:
10 %
11 %
12 %
13 % calculate the electric field:
14 Efield = (-1) .* diff(Vc, 1, 3) / stepsize;
15 % define the coordinates of the three atomic positions of the top triple
16 % layer. Attention: When plotting the image with the command 'axis equal
17 % tight xy', the coordinates are switched! I.e. the
18 % coordinates (X,Y) in the image that are found with the data cursor need
19 % to be switched!
20 xF1 = 140;
21 yF1 = 124;
22 xCa = 101;
23 yCa = 101;
24 xF2 = 101;
25 yF2 = 147;
26 %
27 %
28 %
29 %%%%%%%%%% for the Cu tip:
30 %
31 %
32 %
33 % sensor parameters:
34 f0Cu = 55051.4;
35 k = 1800;
36 A = 50e-12;
37 % define the charge of the Cu tip:

```

## A Appendix

```
38 qCu = 0.13 * qe;
39 % calculate the force:
40 FelCu = qCu .* Efield;
41 % save force spectra on the three atomic sites:
42 SimCuFR = squeeze(FelCu(xCa, yCa, :));
43 SimCuFA = squeeze(FelCu(xF1, yF1, :));
44 SimCuFI = squeeze(FelCu(xF2, yF2, :));
45 % The z-axis of the force data is calculated. Due to the fact that one
46 % starts at 0, the stepsize needs to be subtracted and due to the
47 % differentiation, half of the stepsize needs to be added to the vector
48 % again, resulting in a subtraction of half the stepsize:
49 SimZForce = 1 : size(FelCu, 3);
50 SimZForce = SimZForce' .* stepsize - stepsize/2;
51 % calculate df data with amplitude weight:
52 %
53 % the df values are calculated in 5 pm steps around dz, therefore a vector
54 % to access the data in this range needs to be defined from the oscillation
55 % amplitude:
56 lambdaA = round(-A / stepsize : A / stepsize);
57 % the data point of maximal displacement from dz is defined by dA:
58 dA = round(A / stepsize);
59 sqrt(A^2 - (lambdaA*stepsize).^2)
60 % the prefactor of the integral:
61 prefactorCu = f0Cu ./ (2 * k) .* 2 ./ (pi * A.^2);
62 % calculate the force gradient:
63 kTSCu = (-1) .* diff(FelCu, 1, 3) / stepsize;
64 % preallocate the data matrix for the df data:
65 dfCu = zeros(size(FelCu, 1), size(FelCu, 2), size(FelCu, 3) - 2 * dA - 1);
66 % calculate the df data for every (x,y):
67 for dx = 1 : size(FelCu, 1)
68     for dy = 1 : size(FelCu, 2)
69         % the df data is averaged around dz, depending on A, therefore
70         % points need to be cut away:
71         for dz = (1 + dA) : (size(kTSCu, 3) - dA )
72             % for dz = 104
73                 kTSdummy = squeeze(kTSCu(dx, dy, dz + lambdaA));
74                 integrand = prefactorCu .* kTSdummy' .* sqrt(A^2 - (lambdaA*
75                 stepsize).^2);
76             % integrate the data along the range reached by the oscillation,
```

## A.1 MATLAB code of the electrostatic simulation introduced in chapter 4

```
76 %         defined by lamdaA * stepsize:
77         dfCu(dx, dy, dz - dA) = trapz(lambdaA * stepsize, integrand); %
           just the index is set to 1 instead of 11, A is not subtracted
78         %%%%%%%%%IMPORTANT:
79         % df is calculated at the base point of the oscillation!
80     end
81 end
82     dummyCu = dx
83 end
84 % The z-axis of the simulated df data needs to be saved at the correct
85 % positions. A needs to be cut away at the beginning and at the end of the
86 % z vector. Due to the differentiation in order to get kTS, half the
87 % stepsize needs to be added to the new z-axis:
88 SimZ = SimZForce((1 + dA) : (size(kTSCu, 3) - dA )) + stepsize/2;
89 %%%%%%%%%%%%%%%%%%%%%%%%%%%%%%%%%%%%%%%%%%%%%%%%%%%%%%%%%%%%%%%%%%%%%%%%%
90 %
91 %
92 %
93 %%%%%%%%%%%%%%%%%%%%%%%%%%%%%%%%% for the C0 tip:
94 %
95 %
96 %
97 % sensor parameters:
98 f0C0 = 55.0514065E+3;
99 % define the charge of the C0 tip:
100 qC0 = -0.03 * qe;
101 % calculate the force:
102 FelC0 = qC0 .* Efield;
103 % save force spectra on the three atomic positions:
104 SimCOFA = squeeze(FelC0(xCa, yCa, :));
105 SimCOFR = squeeze(FelC0(xF1, yF1, :));
106 SimCOFI = squeeze(FelC0(xF2, yF2, :));
107 % constant-height slice:
108 figure;
109 imagesc(FelC0(:, :, 83))
110 axis equal tight xy; colorbar
111 %
112 % calculate df data:
113 %
```

## A Appendix

---

```
114 % explanation see calculation for Cu above.
115 prefactorC0 = f0C0 ./ (2 * k) .* 2 ./ (pi * A.^2);
116 kTSC0 = (-1) .* diff(FelC0, 1, 3) / stepsize;
117 dfC0 = zeros(size(FelC0, 1), size(FelC0, 2), size(FelC0, 3) - 2 * dA - 1);
118 for dx = 1 : size(FelC0, 1)
119     for dy = 1 : size(FelC0, 2)
120         for dz = (1 + dA) : (size(kTSC0, 3) - dA )
121             kTSdummy = squeeze(kTSC0(dx, dy, dz + lambdaA));
122             integrand = prefactorC0 .* kTSdummy' .* sqrt(A^2 - (lambdaA*
123                 stepsize).^2);
124             %%%%%%%%%%IMPORTANT:
125             % df is calculated at the base point of oscillation! %
126         end
127     end
128     dummy = dx
129 end
130 clear kTSdummy
131 clear integrand
132 clear dummyCu
133 clear dummy
134 clear lambdaA dA prefactorCu prefactorC0
```

## A.2. Line profiles used to calculate the accuracy values given in table 4.3

Figure A.1 shows the experimental and simulated line profiles used to calculate the accuracy of the model incorporating second tip layer atoms shown in table 4.3.

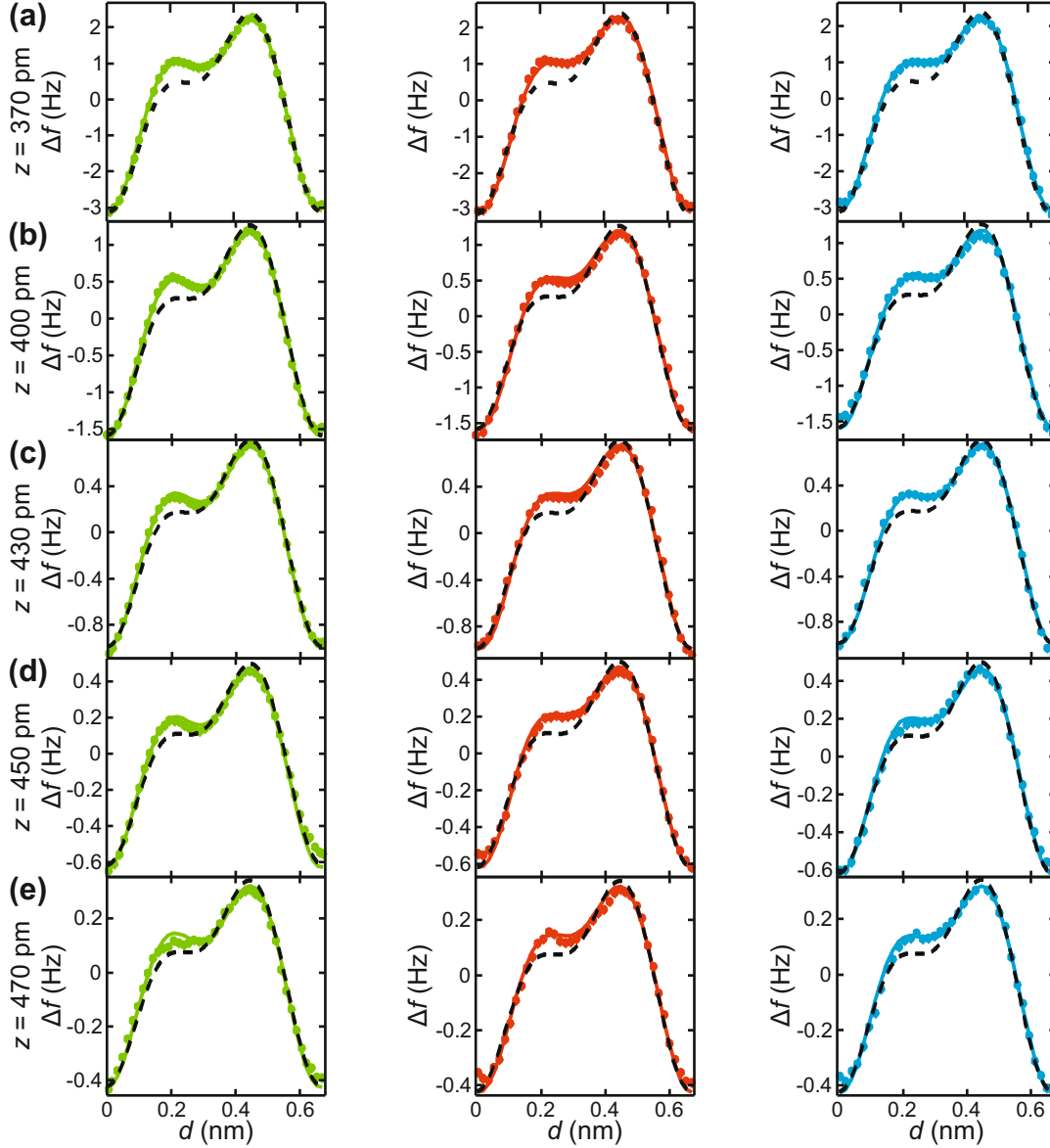


**Figure A.1.:** Line profiles along high-symmetry directions at different tip-sample separations. Experimental and calculated line profiles extracted along the three high-symmetry directions of the  $\text{CaF}_2(111)$  surface at different tip-sample distances. The calculation incorporating second layer tip atoms (solid) better reproduces the experimental data (dotted) than the calculation incorporating only a single point charge (dashed). The accuracy is given as a function of tip-sample distance in table 4.3 in chapter 4. Figure adapted from Ref. [132].

### A.3. Experimental and calculated constant-height images of $\text{CaF}_2(111)$ obtained with the CO tip as a function of tip-sample distance

For better comparison, Fig. A.2 shows the experimental and calculated images of  $\text{CaF}_2(111)$  depicted in Fig. 5.3 and Fig. 5.5 as a single figure.

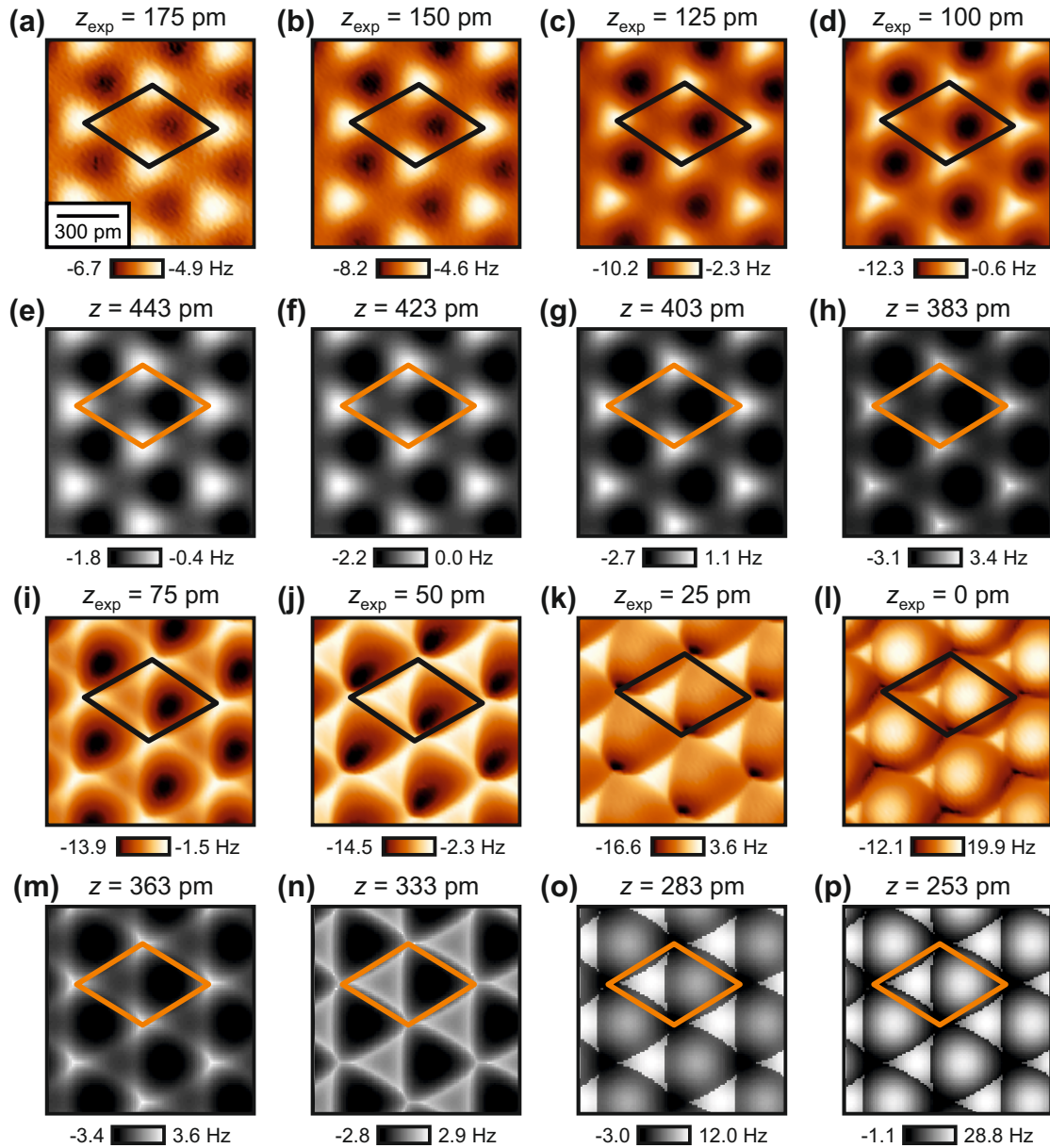


**Figure A.2.:** Comparison of experimental and calculated constant-height images of  $\text{CaF}_2(111)$  obtained with a CO tip. (a)–(d), (i)–(l) Experimental constant-height images, as shown in Fig. 5.3. (e)–(h), (m)–(p) Calculated constant-height images, as shown in Fig. 5.5. Figure adapted from Ref. [132].

## A.4. Additional images at smaller $z$ values calculated with the PPM using the electron density overlap method

Experimental constant-height images of  $\text{CaF}_2(111)$  recorded with a CO tip show a shrinking of the bright triangular features corresponding to the  $\text{F}_{\text{bot}}^-$  sites, located in the left halves of the unit cells in Fig. 5.3(j)–(l). The PPM using the overlap of the electron densities of tip and sample reproduces this shrinking only at smaller tip-sample distances. Figure A.3 shows additional calculated constant-height images at smaller tip-sample distances compared to the images shown in Fig. 5.5.

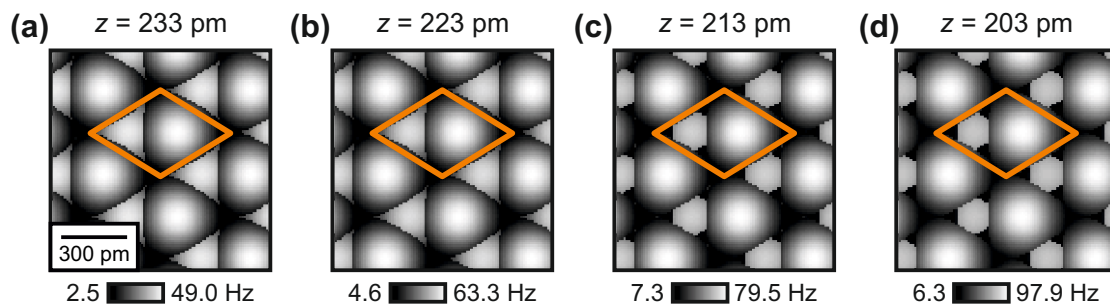


**Figure A.3.: Additional approach images created with the PPM at smaller distances.** The images have been calculated with the density overlap method employed for simulating the images in Fig. 5.5. Approaching closer to the surface, the bright triangular features in the left halves of the unit cells shrink, as seen in the experiment. Figure adapted from Ref. [139].

## A.5. Comparison of calculated constant-height images of $\text{CaF}_2(111)$ using both PPM methods

For better comparison, Fig. A.4 shows the calculated constant-height images of the  $\text{CaF}_2(111)$  surface that have been created with the two different versions of the PPM. The images are already shown in Fig. 5.5 and Fig. 5.8, respectively.

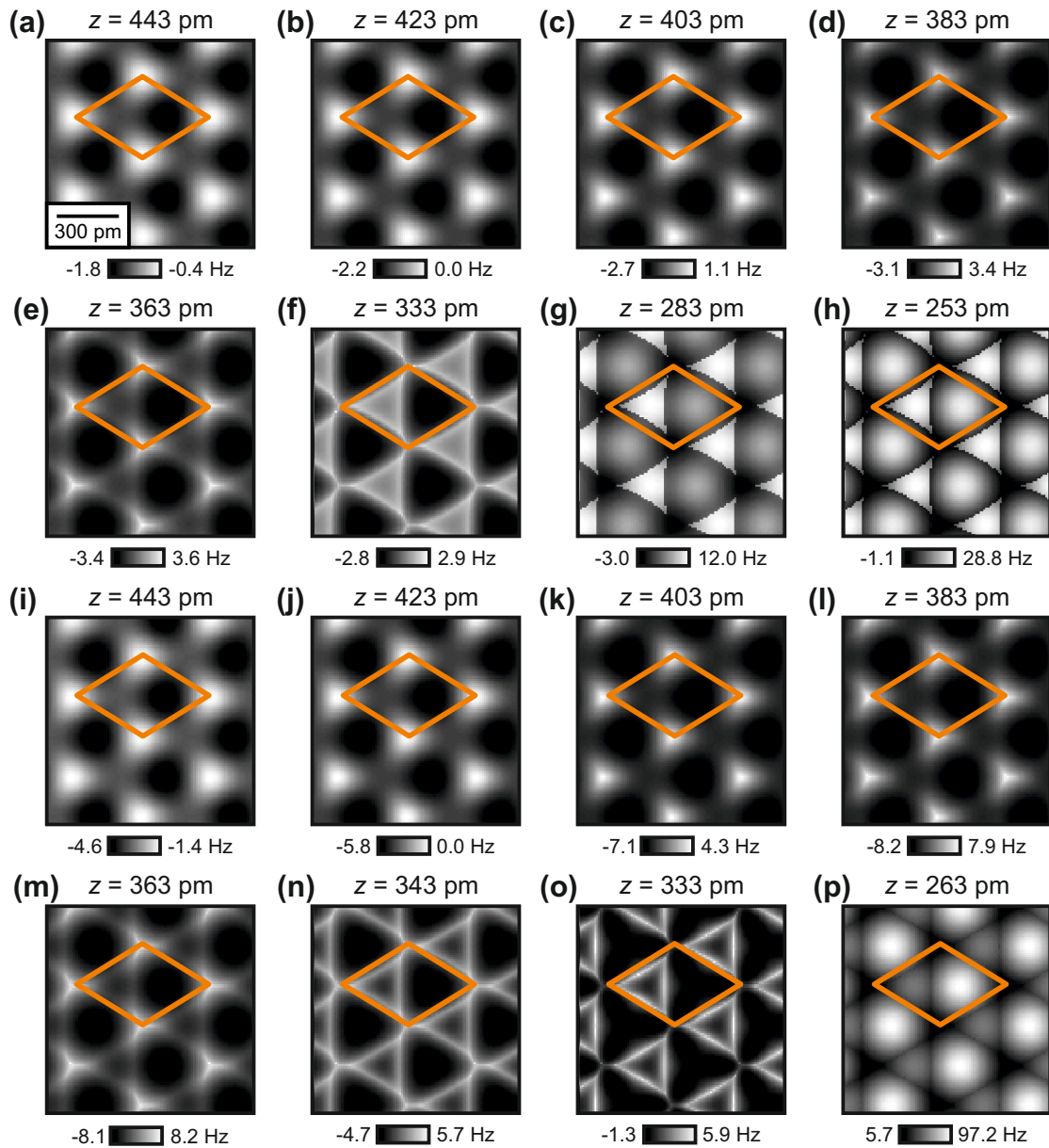


**Figure A.4.:** Comparison of constant-height images created with the two different versions of the probe particle model. (a)–(h) Images created with the modified density overlap version of the PPM, as shown in Fig. 5.5. (i)–(p) Images created with the standard model using Lennard-Jones potentials to calculate the contribution of Pauli repulsion, as shown in Fig. 5.8. Figure adapted from Ref. [132].

## A.6. Line profiles extracted from STM images of the Cu(110)-(2 × 1)O AR reconstruction with different CuOx tips

In chapter 6, experimental data recorded with two different CuOx tips with a single oxygen atom at the tip apex is discussed. For direct comparison, the STM images of the Cu(110)-(2 × 1)O AR reconstruction recorded with the two single-atom CuOx tips are shown in Fig. A.5 together with line profiles across the copper oxide domain.

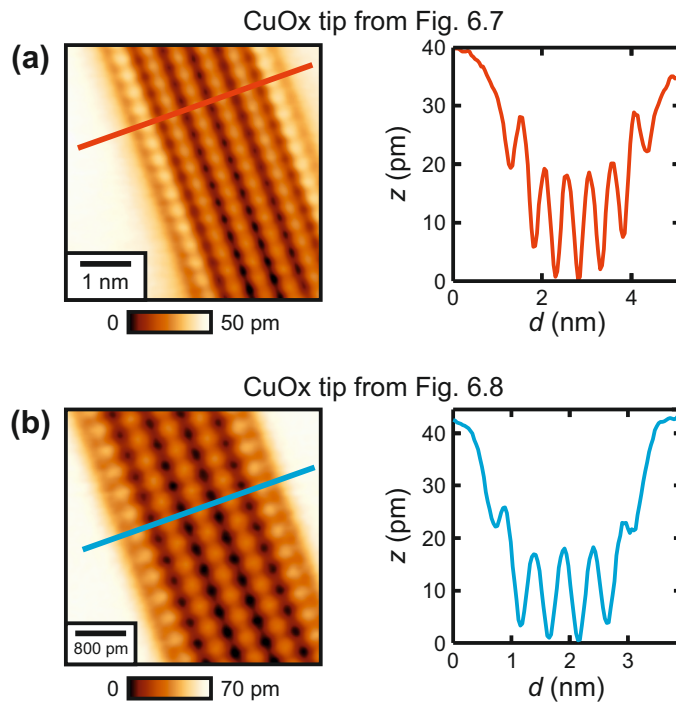


**Figure A.5.:** STM images and corresponding line profiles of the Cu(110)-(2 × 1)O added-row reconstruction. Both data sets were recorded with single-atom CuOx tips. (a) Corresponding data from Fig 6.7. (b) Corresponding data from Fig 6.8. Figure partly adapted from Ref. [169].



# List of Publications

The following list shows all publications that were authored or co-authored by the author of this thesis.

- A. Liebig and F. J. Giessibl, *In-situ characterization of O-terminated Cu tips for high-resolution atomic force microscopy*, Appl. Phys. Lett. **114**, 143103 (2019).
- A. Liebig, A. Peronio, D. Meuer, A. J. Weymouth and F. J. Giessibl, *High-precision atomic force microscopy with atomically-characterized tips*, New J. Phys. **22**, 063040 (2020).
- A. Liebig, P. Hapala, A. J. Weymouth and F. J. Giessibl, *Quantifying the evolution of atomic interaction of a complex surface with a functionalized atomic force microscopy tip*, Sci. Rep. **10**, 14104 (2020).



# Bibliography

- [1] S. M. Lindsay, *Introduction to Nanoscience* (Oxford University Press, New York, 2010).
- [2] Z. J. Deng, S. W. Morton, E. Ben-Akiva, E. C. Dreaden, K. E. Shopsowitz, and P. T. Hammond, *Layer-by-layer nanoparticles for systemic codelivery of an anticancer drug and siRNA for potential triple-negative breast cancer treatment*, *ACS Nano* **7**, 9571 (2013).
- [3] Editorial, *Nanomedicine and the COVID-19 vaccines*, *Nat. Nanotechnol.* **15**, 963 (2020).
- [4] F. Arute, K. Arya, R. Babbush, D. Bacon, J. C. Bardin, R. Barends, R. Biswas, S. Boixo, F. G. Brandao, D. A. Buell, B. Burkett, Y. Chen, Z. Chen, B. Chiaro, R. Collins, W. Courtney, A. Dunsworth, E. Farhi, B. Foxen, A. Fowler, C. Gidney, M. Giustina, R. Graff, K. Guerin, S. Habegger, M. P. Harrigan, M. J. Hartmann, A. Ho, M. Hoffmann, T. Huang, T. S. Humble, S. V. Isakov, E. Jeffrey, Z. Jiang, D. Kafri, K. Kechedzhi, J. Kelly, P. V. Klimov, S. Knysh, A. Korotkov, F. Kostritsa, D. Landhuis, M. Lindmark, E. Lucero, D. Lyakh, S. Mandrà, J. R. McClean, M. McEwen, A. Megrant, X. Mi, K. Michielsen, M. Mohseni, J. Mutus, O. Naaman, M. Neeley, C. Neill, M. Y. Niu, E. Ostby, A. Petukhov, J. C. Platt, C. Quintana, E. G. Rieffel, P. Roushan, N. C. Rubin, D. Sank, K. J. Satzinger, V. Smelyanskiy, K. J. Sung, M. D. Trevithick, A. Vainsencher, B. Villalonga, T. White, Z. J. Yao, P. Yeh, A. Zalcman, H. Neven, and J. M. Martinis, *Quantum supremacy using a programmable superconducting processor*, *Nature* **574**, 505 (2019).
- [5] S. Loth, M. Etzkorn, C. P. Lutz, D. M. Eigler, and A. J. Heinrich, *Measurement of fast electron spin relaxation times with atomic resolution*, *Science* **329**, 1628 (2010).
- [6] A. A. Khajetoorians, B. Baxevanis, C. Hübner, T. Schlenk, S. Krause, T. O. Wehling, S. Lounis, A. Lichtenstein, D. Pfannkuche, J. Wiebe, and R. Wiesen-

- danger, *Current-Driven Spin Dynamics of Artificially Constructed Quantum Magnets*, Science **339**, 55 (2013).
- [7] F. Donati, S. Rusponi, S. Stepanow, C. Wäckerlin, A. Singha, L. Persichetti, R. Baltic, K. Diller, F. Patthey, E. Fernandes, J. Dreiser, Ž. Šljivančanin, K. Kummer, C. Nistor, P. Gambardella, and H. Brune, *Magnetic remanence in single atoms*, Science **352**, 318 (2016).
- [8] Y. Bae, K. Yang, P. Willke, T. Choi, A. J. Heinrich, and C. P. Lutz, *Enhanced quantum coherence in exchange coupled spins via singlet-triplet transitions*, Sci. Adv. **4**, eaau4159 (2018).
- [9] G. Binnig, C. F. Quate, and C. Gerber, *Atomic Force Microscope*, Phys. Rev. Lett. **56**, 930 (1986).
- [10] T. R. Albrecht, P. Grütter, D. Horne, and D. Rugar, *Frequency modulation detection using high-Q cantilevers for enhanced force microscope sensitivity*, J. Appl. Phys. **69**, 668 (1991).
- [11] D. M. Eigler and E. K. Schweizer, *Positioning single atoms with a scanning tunneling microscope*, Nature **344**, 524 (1990).
- [12] F. J. Giessibl, *Atomic Resolution of the Silicon (111)-(7x7) Surface by Atomic Force Microscopy*, Science **267**, 68 (1995).
- [13] S.-I. Kitamura and M. Iwatsuki, *Observation of 7x7 Reconstructed Structure on the Silicon (111) Surface Using Ultrahigh Vacuum Noncontact Atomic Force Microscopy*, Jpn. J. Appl. Phys. **34**, L145 (1995).
- [14] A. S. Foster, C. Barth, A. L. Shluger, R. M. Nieminen, and M. Reichling, *Role of tip structure and surface relaxation in atomic resolution dynamic force microscopy: CaF<sub>2</sub>(111) as a reference surface*, Phys. Rev. B **66**, 235417 (2002).
- [15] R. Hoffmann, C. Barth, A. S. Foster, A. L. Shluger, H. J. Hug, H. J. Güntherodt, R. M. Nieminen, and M. Reichling, *Measuring site-specific cluster-surface bond formation*, J. Am. Chem. Soc. **127**, 17863 (2005).
- [16] Z. Sun, M. P. Boneschanscher, I. Swart, D. Vanmaekelbergh, and P. Liljeroth, *Quantitative atomic force microscopy with carbon monoxide terminated tips*, Phys. Rev. Lett. **106**, 046104 (2011).

- [17] M. Ternes, C. González, C. P. Lutz, P. Hapala, F. J. Giessibl, P. Jelínek, and A. J. Heinrich, *Interplay of conductance, force, and structural change in metallic point contacts*, Phys. Rev. Lett. **106**, 016802 (2011).
- [18] L. Gross, F. Mohn, N. Moll, B. Schuler, A. Criado, E. Guitián, D. Peña, A. Gourdon, and G. Meyer, *Bond-order discrimination by atomic force microscopy*, Science **337**, 1326 (2012).
- [19] M. Ondráček, C. González, and P. Jelínek, *Reversal of atomic contrast in scanning probe microscopy on (111) metal surfaces*, J. Phys. Condens. Matter **24**, 084003 (2012).
- [20] B. Such, T. Glatzel, S. Kawai, E. Meyer, R. Turanský, J. Brndiar, and I. Štich, *Interplay of the tip-sample junction stability and image contrast reversal on a Cu(111) surface revealed by the 3D force field*, Nanotechnology **23**, 045705 (2012).
- [21] A. J. Weymouth, T. Hofmann, and F. J. Giessibl, *Quantifying molecular stiffness and interaction with lateral force microscopy.*, Science **343**, 1120 (2014).
- [22] P. Hapala, G. Kichin, C. Wagner, F. S. Tautz, R. Temirov, and P. Jelínek, *Mechanism of high-resolution STM/AFM imaging with functionalized tips*, Phys. Rev. B **90**, 085421 (2014).
- [23] N. Moll, B. Schuler, S. Kawai, F. Xu, L. Peng, A. Orita, J. Otera, A. Curioni, M. Neu, J. Repp, G. Meyer, and L. Gross, *Image distortions of a partially fluorinated hydrocarbon molecule in atomic force microscopy with carbon monoxide terminated tips*, Nano Lett. **14**, 6127 (2014).
- [24] W. A. Hofer, A. J. Fisher, R. A. Wolkow, and P. Grütter, *Surface relaxations, current enhancements, and absolute distances in high resolution scanning tunneling microscopy*, Phys. Rev. Lett. **87**, 236104 (2001).
- [25] F. Huber, J. Berwanger, S. Polesya, S. Mankovsky, H. Ebert, and F. J. Giessibl, *Chemical bond formation showing a transition from physisorption to chemisorption*, Science **366**, 235 (2019).
- [26] R. Schmidt, A. Schwarz, and R. Wiesendanger, *Magnetization switching utilizing the magnetic exchange interaction*, Phys. Rev. B **86**, 174402 (2012).
- [27] F. Pielmeier and F. J. Giessibl, *Spin resolution and evidence for superexchange on NiO(001) observed by force microscopy*, Phys. Rev. Lett. **110**, 266101 (2013).

- [28] I. Shapir, A. Hamo, S. Pecker, C. P. Moca, Ö. Legeza, G. Zarand, and S. Ilani, *Imaging the electronic Wigner crystal in one dimension*, *Science* **364**, 870 (2019).
- [29] T. Hofmann, F. Pielmeier, and F. J. Giessibl, *Chemical and crystallographic characterization of the tip apex in scanning probe microscopy*, *Phys. Rev. Lett.* **112**, 066101 (2014).
- [30] J. Welker and F. J. Giessibl, *Revealing the Angular Symmetry of Chemical Bonds by Atomic Force Microscopy*, *Science* **336**, 444 (2012).
- [31] J. Welker, A. J. Weymouth, and F. J. Giessibl, *The Influence of Chemical Bonding Configuration on Atomic Identification by Force Spectroscopy*, *ACS Nano* **7**, 7377 (2013).
- [32] M. Emmrich, M. Schneiderbauer, F. Huber, A. J. Weymouth, N. Okabayashi, and F. J. Giessibl, *Force Field Analysis Suggests a Lowering of Diffusion Barriers in Atomic Manipulation Due to Presence of STM Tip*, *Phys. Rev. Lett.* **114**, 146101 (2015).
- [33] L. Gross, F. Mohn, N. Moll, P. Liljeroth, and G. Meyer, *The Chemical Structure of a Molecule Resolved by Atomic Force Microscopy*, *Science* **325**, 1110 (2009).
- [34] N. Moll, L. Gross, F. Mohn, A. Curioni, and G. Meyer, *The mechanisms underlying the enhanced resolution of atomic force microscopy with functionalized tips*, *New J. Phys.* **12**, 125020 (2010).
- [35] M. Ellner, N. Pavliček, P. Pou, B. Schuler, N. Moll, G. Meyer, L. Gross, and R. Pérez, *The electric field of CO tips and its relevance for atomic force microscopy*, *Nano Lett.* **16**, 1974 (2016).
- [36] F. Schulz, J. Ritala, O. Krejčí, A. P. Seitsonen, A. S. Foster, and P. Liljeroth, *Elemental Identification by Combining Atomic Force Microscopy and Kelvin Probe Force Microscopy*, *ACS Nano* **12**, 5274 (2018).
- [37] F. J. Giessibl, *High-speed force sensor for force microscopy and profilometry utilizing a quartz tuning fork*, *Appl. Phys. Lett.* **73**, 3956 (1998).
- [38] H. Mönig, D. R. Hermoso, O. Díaz Arado, M. Todorović, A. Timmer, S. Schüer, G. Langewisch, R. Pérez, and H. Fuchs, *Submolecular Imaging by Noncontact Atomic Force Microscopy with an Oxygen Atom Rigidly Connected to a Metallic Probe*, *ACS Nano* **10**, 1201 (2016).

- 
- [39] G. Binnig, H. Rohrer, C. Gerber, and E. Weibel, *Surface studies by scanning tunneling microscopy*, Phys. Rev. Lett. **49**, 57 (1982).
- [40] G. Binnig, H. Rohrer, C. Gerber, and E. Weibel, *7 x 7 Reconstruction on Si(111) Resolved in Real Space*, Phys. Rev. Lett. **50**, 120 (1983).
- [41] C. J. Chen, *Introduction to Scanning Tunneling Microscopy* (Oxford University Press, New York, 1993).
- [42] G. Binnig, H. Rohrer, C. Gerber, and E. Weibel, *Tunneling through a controllable vacuum gap*, Appl. Phys. Lett. **40**, 178 (1982).
- [43] H. B. Michaelson, *The work function of the elements and its periodicity*, J. Appl. Phys. **48**, 4729 (1977).
- [44] J. Bardeen, *Tunneling from a many particle point of view*, Phys. Rev. Lett. **6**, 57 (1961).
- [45] J. Tersoff and D. R. Hamann, *Theory and Application for the Scanning Tunneling Microscope*, Phys. Rev. Lett. **50**, 1998 (1983).
- [46] J. Tersoff and D. R. Hamann, *Theory of the scanning tunneling microscope*, Phys. Rev. B **31**, 805 (1985).
- [47] U. Diebold, J. F. Anderson, K. O. Ng, and D. Vanderbilt, *Evidence for the tunneling site on transition-metal oxides: TiO<sub>2</sub>(110)*, Phys. Rev. Lett. **77**, 1322 (1996).
- [48] U. Dürig, J. K. Gimzewski, and D. W. Pohl, *Experimental observation of forces acting during scanning tunneling microscopy*, Phys. Rev. Lett. **57**, 2403 (1986).
- [49] R. García and R. Pérez, *Dynamic atomic force microscopy methods*, Surf. Sci. Rep. **47**, 197 (2002).
- [50] F. J. Giessibl, *Advances in atomic force microscopy*, Rev. Mod. Phys. **75**, 949 (2003).
- [51] S. Morita, R. Wiesendanger, and E. Meyer, *Noncontact Atomic Force Microscopy* (Springer-Verlag Berlin Heidelberg, 2002).
- [52] S. Morita, F. J. Giessibl, and R. Wiesendanger, *Noncontact Atomic Force Microscopy, Volume 2* (Springer-Verlag Berlin Heidelberg, 2009).

## Bibliography

---

- [53] S. Morita, F. J. Giessibl, E. Meyer, and R. Wiesendanger, *Noncontact Atomic Force Microscopy, Volume 3* (Springer-Verlag Berlin Heidelberg, 2015).
- [54] F. J. Giessibl, *The qPlus sensor, a powerful core for the atomic force microscope*, Rev. Sci. Instrum. **90**, 011101 (2019).
- [55] Y. Martin, C. C. Williams, and H. K. Wickramasinghe, *Atomic force microscope-force mapping and profiling on a sub 100-Å scale*, J. Appl. Phys. **61**, 4723 (1987).
- [56] T. Ando, T. Uchihashi, N. Kodera, D. Yamamoto, A. Miyagi, M. Taniguchi, and H. Yamashita, *High-speed AFM and nano-visualization of biomolecular processes*, Pflugers Arch. Eur. J. Physiol. **456**, 211 (2008).
- [57] M. Lee and W. Jhe, *General theory of amplitude-modulation atomic force microscopy*, Phys. Rev. Lett. **97**, 036104 (2006).
- [58] F. J. Giessibl, *A direct method to calculate tip-sample forces from frequency shifts in frequency-modulation atomic force microscopy*, Appl. Phys. Lett. **78**, 123 (2001).
- [59] F. J. Giessibl, *Forces and frequency shifts in atomic-resolution dynamic-force microscopy*, Phys. Rev. B **56**, 16010 (1997).
- [60] J. N. Israelachvili, *Intermolecular and Surface Forces* (Elsevier Academic Press, Cambridge, 2011).
- [61] B. R. Holstein, *The van der Waals interaction*, Am. J. Phys. **69**, 441 (2001).
- [62] T. Gould and T. Bučko,  *$C_6$  Coefficients and Dipole Polarizabilities for All Atoms and Many Ions in Rows 1-6 of the Periodic Table*, J. Chem. Theory Comput. **12**, 3603 (2016).
- [63] H. Hamaker, *The London—van der Waals attraction between spherical particles*, Physica **4**, 1058 (1937).
- [64] M. Nonnenmacher, M. P. O’Boyle, and H. K. Wickramasinghe, *Kelvin probe force microscopy*, Appl. Phys. Lett. **58**, 2921 (1991).
- [65] B. Law and F. Rieutord, *Electrostatic forces in atomic force microscopy*, Phys. Rev. B **66**, 035402 (2002).

- 
- [66] G. Teobaldi, K. Lämmle, T. Trevethan, M. Watkins, A. Schwarz, R. Wiesendanger, and A. L. Shluger, *Chemical resolution at ionic crystal surfaces using dynamic atomic force microscopy with metallic tips*, Phys. Rev. Lett. **106**, 216102 (2011).
- [67] H. Söngen, P. Rahe, J. L. Neff, R. Bechstein, J. Ritala, A. S. Foster, and A. Kühnle, *The weight function for charges—A rigorous theoretical concept for Kelvin probe force microscopy*, J. Appl. Phys. **119**, 025304 (2016).
- [68] W. Pauli, *Über den Zusammenhang des Abschlusses der Elektronengruppen im Atom mit der Komplexstruktur der Spektren*, Zeitschrift für Phys. **31**, 765 (1925).
- [69] J. E. Lennard-Jones, *Processes of adsorption and diffusion on solid surfaces*, Trans. Faraday Soc. **28**, 333 (1932).
- [70] T. Fauster, L. Hammer, K. Heinz, and M. A. Schneider, *Oberflächenphysik* (Oldenbourg Verlag München, 2013).
- [71] K. Oura, V. G. Lifshits, A. A. Saranin, A. V. Zotov, and M. Katayama, *Surface Science: An Introduction* (Springer-Verlag Berlin Heidelberg New York, 2003).
- [72] N. Moll, L. Gross, F. Mohn, A. Curioni, and G. Meyer, *A simple model of molecular imaging with noncontact atomic force microscopy*, New J. Phys. **14**, 083023 (2012).
- [73] P. Hapala, R. Temirov, F. S. Tautz, and P. Jelínek, *Origin of high-resolution IETS-STM images of organic molecules with functionalized tips*, Phys. Rev. Lett. **113**, 226101 (2014).
- [74] F. J. Giessibl, *Theory for an electrostatic imaging mechanism allowing atomic resolution of ionic crystals by atomic force microscopy*, Phys. Rev. B **45**, 13815 (1992).
- [75] F. J. Giessibl, H. Bielefeldt, S. Hembacher, and J. Mannhart, *Calculation of the optimal imaging parameters for frequency modulation atomic force microscopy*, Appl. Surf. Sci. **140**, 352 (1999).
- [76] F. J. Giessibl, F. Pielmeier, T. Eguchi, T. An, and Y. Hasegawa, *Comparison of force sensors for atomic force microscopy based on quartz tuning forks and length-extensional resonators*, Phys. Rev. B **84**, 125409 (2011).

- [77] M. Ternes, C. P. Lutz, C. F. Hirjibehedin, F. J. Giessibl, and A. J. Heinrich, *The Force Needed to Move an Atom on a Surface*, *Science* **319**, 1066 (2008).
- [78] J. E. Sader and S. P. Jarvis, *Accurate formulas for interaction force and energy in frequency modulation force spectroscopy*, *Appl. Phys. Lett.* **84**, 1801 (2004).
- [79] J. Welker, E. Illek, and F. J. Giessibl, *Analysis of force-deconvolution methods in frequency-modulation atomic force microscopy*, *Beilstein J. Nanotechnol.* **3**, 238 (2012).
- [80] J. E. Sader, B. D. Hughes, F. Huber, and F. J. Giessibl, *Interatomic force laws that evade dynamic measurement*, *Nat. Nanotechnol.* **13**, 1088 (2018).
- [81] F. Huber and F. J. Giessibl, *Experimental use of the inflection point test for force deconvolution in frequency-modulation atomic force microscopy to turn an ill-posed situation into a well-posed one by proper choice of amplitude*, *J. Appl. Phys.* **127**, 184301 (2020).
- [82] B. Schuler, W. Liu, A. Tkatchenko, N. Moll, G. Meyer, A. Mistry, D. Fox, and L. Gross, *Adsorption Geometry Determination of Single Molecules by Atomic Force Microscopy*, *Phys. Rev. Lett.* **111**, 106103 (2013).
- [83] J. Licha, *Implementierung einer Driftkorrektur für subatomar aufgelöste 3D-Rastersondenspektroskopie* (Bachelor thesis, University of Regensburg, 2013).
- [84] J. Welker, *Höchstauflösende Kraftmikroskopie mit subatomar definierten Bindungszuständen* (PhD thesis, University of Regensburg, 2012).
- [85] A. Liebig, *High-precision AFM investigation on  $\text{CaF}_2(111)$  with atomically characterized tips* (Master thesis, University of Regensburg, 2016).
- [86] T. Hofmann, *Hochauflösende Rasterkraftmikroskopie auf Graphen und Kohlenmonoxid* (PhD thesis, University of Regensburg, 2014).
- [87] E. W. Müller, *Das Feldionenmikroskop*, *Zeitschrift für Phys.* **131**, 136 (1951).
- [88] F. Pielmeier, G. Landolt, B. Slomski, S. Muff, J. Berwanger, A. Eich, A. A. Khajetoorians, J. Wiebe, Z. S. Aliev, M. B. Babanly, R. Wiesendanger, J. Osterwalder, E. V. Chulkov, F. J. Giessibl, and J. H. Dil, *Response of the topological surface state to surface disorder in  $\text{TlBiSe}_2$* , *New J. Phys.* **17**, 023067 (2015).

- [89] C. Zaum, K. M. Meyer-Auf-Der-Heide, M. Mehlhorn, S. McDonough, W. F. Schneider, and K. Morgenstern, *Differences between thermal and laser-induced diffusion*, Phys. Rev. Lett. **114**, 146104 (2015).
- [90] M. Assig, M. Etzkorn, A. Enders, W. Stiepany, C. R. Ast, and K. Kern, *A 10 mK scanning tunneling microscope operating in ultra high vacuum and high magnetic fields*, Rev. Sci. Instrum. **84**, 033903 (2013).
- [91] A. Peronio, N. Okabayashi, F. Griesbeck, and F. Giessibl, *Radio frequency filter for an enhanced resolution of inelastic electron tunneling spectroscopy in a combined scanning tunneling- and atomic force microscope*, Rev. Sci. Instrum. **90**, 123104 (2019).
- [92] A. Peronio and F. J. Giessibl, *Attempts to test an alternative electrodynamic theory of superconductors by low-temperature scanning tunneling and atomic force microscopy*, Phys. Rev. B **94**, 094503 (2016).
- [93] N. Okabayashi, A. Gustafsson, A. Peronio, M. Paulsson, and F. J. Giessibl, *Influence of atomic tip structure on the intensity of inelastic tunneling spectroscopy data analyzed by combined scanning tunneling spectroscopy, force microscopy and density functional theory*, Phys. Rev. B **93**, 165415 (2016).
- [94] N. Okabayashi, A. Peronio, M. Paulsson, T. Arai, and F. J. Giessibl, *Vibrations of a molecule in an external force field*, Proc. Natl. Acad. Sci. **115**, 4571 (2018).
- [95] F. J. Giessibl, *Sensor und Verfahren zum berührungslosen Abtasten einer Oberfläche*, Patent DE 10 2010 052 037.3, Deutsches Patent- und Markenamt (18 April 2013).
- [96] F. Pielmeier, D. Meuer, D. Schmid, C. Strunk, and F. J. Giessibl, *Impact of thermal frequency drift on highest precision force microscopy using quartz-based force sensors at low temperatures*, Beilstein J. Nanotechnol. **5**, 407 (2014).
- [97] F. Huber and F. J. Giessibl, *Low noise current preamplifier for qPlus sensor deflection signal detection in atomic force microscopy at room and low temperatures*, Rev. Sci. Instrum. **88**, 073702 (2017).
- [98] K. Pürckhauer, A. J. Weymouth, K. Pfeffer, L. Kullmann, E. Mulvihill, M. P. Krahn, D. J. Müller, and F. J. Giessibl, *Imaging in Biologically-Relevant Environments with AFM Using Stiff qPlus Sensors*, Sci. Rep. **8**, 9330 (2018).

- [99] F. J. Giessibl, S. Hembacher, M. Herz, C. Schiller, and J. Mannhart, *Stability considerations and implementation of cantilevers allowing dynamic force microscopy with optimal resolution: the qPlus sensor*, Nanotechnology **15**, S79 (2004).
- [100] D. S. Wastl, A. J. Weymouth, and F. J. Giessibl, *Optimizing atomic resolution of force microscopy in ambient conditions*, Phys. Rev. B **87**, 245415 (2013).
- [101] F. J. Giessibl, *Atomic resolution on Si(111)-(7×7) by noncontact atomic force microscopy with a force sensor based on a quartz tuning fork*, Appl. Phys. Lett. **76**, 1470 (2000).
- [102] J. Welker, F. de Faria Elsner, and F. J. Giessibl, *Application of the equipartition theorem to the thermal excitation of quartz tuning forks*, Appl. Phys. Lett. **99**, 084102 (2011).
- [103] G. H. Simon, M. Heyde, and H. P. Rust, *Recipes for cantilever parameter determination in dynamic force spectroscopy: Spring constant and amplitude*, Nanotechnology **18**, 255503 (2007).
- [104] R. G. Musket, W. McLean, C. A. Colmenares, D. M. Makowiecki, and W. J. Siekhaus, *Preparation of atomically clean surfaces of selected elements: A review*, Appl. Surf. Sci. **10**, 143 (1982).
- [105] W. L. Chan and E. Chason, *Making waves: Kinetic processes controlling surface evolution during low energy ion sputtering*, J. Appl. Phys. **101**, 121301 (2007).
- [106] M. E. Straumanis and L. S. Yu, *Lattice parameters, densities, expansion coefficients and perfection of structure of Cu and of Cu–In  $\alpha$  phase*, Acta Crystallogr. Sect. A **25**, 676 (1969).
- [107] W. L. Bragg, *XLII. The crystalline structure of copper*, London, Edinburgh, Dublin Philos. Mag. J. Sci. **28**, 355 (1914).
- [108] R. K. Tiwari, D. M. Otálvaro, C. Joachim, and M. Saeys, *Origin of the contrast inversion in the STM image of CO on Cu(111)*, Surf. Sci. **603**, 3286 (2009).
- [109] K. K. Gomes, W. Mar, W. Ko, F. Guinea, and H. C. Manoharan, *Designer Dirac fermions and topological phases in molecular graphene*, Nature **483**, 306 (2012).

- 
- [110] O. Gretz, A. J. Weymouth, and F. J. Giessibl, *Identifying the atomic configuration of the tip apex using STM and frequency-modulation AFM with CO on Pt(111)*, Phys. Rev. Res. **2**, 033094 (2020).
- [111] J. Friedel, *Metallic alloys*, Nuovo Cim. **7**, 287 (1958).
- [112] M. F. Crommie, C. P. Lutz, and D. M. Eigler, *Imaging standing waves in a two-dimensional electron gas*, Nature **363**, 524 (1993).
- [113] L. Bartels, G. Meyer, and K.-H. Rieder, *Controlled vertical manipulation of single CO molecules with the scanning tunneling microscope: A route to chemical contrast*, Appl. Phys. Lett. **71**, 213 (1997).
- [114] S.-i. Ishi, Y. Ohno, and B. Viswanathan, *An overview on the electronic and vibrational properties of adsorbed CO*, Surf. Sci. **161**, 349 (1985).
- [115] G. Schull, T. Frederiksen, A. Arnau, D. Sánchez-Portal, and R. Berndt, *Atomic-scale engineering of electrodes for single-molecule contacts*, Nat. Nanotechnol. **6**, 23 (2011).
- [116] F. Mohn, B. Schuler, L. Gross, and G. Meyer, *Different tips for high-resolution atomic force microscopy and scanning tunneling microscopy of single molecules*, Appl. Phys. Lett. **102**, 073109 (2013).
- [117] S. W. Hla, K. F. Braun, V. Iancu, and A. Deshpande, *Single-atom extraction by scanning tunneling microscope tip crash and nanoscale surface engineering*, Nano Lett. **4**, 1997 (2004).
- [118] D. M. Eigler, C. P. Lutz, and W. E. Rudge, *An atomic switch realized with the scanning tunnelling microscope*, Nature **352**, 600 (1991).
- [119] G. Kichin, C. Weiss, C. Wagner, F. S. Tautz, and R. Temirov, *Single molecule and single atom sensors for atomic resolution imaging of chemically complex surfaces*, J. Am. Chem. Soc. **133**, 16847 (2011).
- [120] L. Bartels, G. Meyer, K.-H. Rieder, D. Velic, E. Knoesel, A. Hotzel, M. Wolf, and G. Ertl, *Dynamics of Electron-Induced Manipulation of Individual CO Molecules on Cu(111)*, Phys. Rev. Lett. **80**, 2004 (1998).
- [121] P. Jelínek, *High resolution SPM imaging of organic molecules with functionalized tips*, J. Phys. Condens. Matter **29**, 343002 (2017).

- [122] N. Pavliček and L. Gross, *Generation, manipulation and characterization of molecules by atomic force microscopy*, Nat. Rev. Chem. **1**, 0005 (2017).
- [123] M. P. Boneschanscher, J. van der Lit, Z. Sun, I. Swart, P. Liljeroth, and D. Vanmaekelbergh, *Quantitative Atomic Resolution Force Imaging on Epitaxial Graphene with Reactive and Nonreactive AFM Probes*, ACS Nano **6**, 10216 (2012).
- [124] M. P. Boneschanscher, S. K. Hämäläinen, P. Liljeroth, and I. Swart, *Sample corrugation affects the apparent bond lengths in atomic force microscopy*, ACS Nano **8**, 3006 (2014).
- [125] J. Peng, D. Cao, Z. He, J. Guo, P. Hapala, R. Ma, B. Cheng, J. Chen, W. J. Xie, X.-Z. Li, P. Jelínek, L.-M. Xu, Y. Q. Gao, E.-G. Wang, and Y. Jiang, *The effect of hydration number on the interfacial transport of sodium ions*, Nature **557**, 701 (2018).
- [126] J. Berwanger, F. Huber, F. Stilp, and F. J. Giessibl, *Lateral manipulation of single iron adatoms by means of combined atomic force and scanning tunneling microscopy using CO-terminated tips*, Phys. Rev. B **98**, 195409 (2018).
- [127] J. Berwanger, S. Polesya, S. Mankovsky, H. Ebert, and F. J. Giessibl, *Atomically Resolved Chemical Reactivity of Small Fe Clusters*, Phys. Rev. Lett. **124**, 096001 (2020).
- [128] P. Hollins and J. Pritchard, *Interactions of CO molecules adsorbed on Cu(111)*, Surf. Sci. **89**, 486 (1979).
- [129] H. Sang, S. P. Jarvis, Z. Zhou, P. Sharp, P. Moriarty, J. Wang, Y. Wang, and L. Kantorovich, *Identifying tips for intramolecular NC-AFM imaging via in situ fingerprinting.*, Sci. Rep. **4**, 6678 (2014).
- [130] D. Z. Gao, J. Grenz, M. B. Watkins, F. Federici Canova, A. Schwarz, R. Wiesendanger, and A. L. Shluger, *Using metallic noncontact atomic force microscope tips for imaging insulators and polar molecules: Tip characterization and imaging mechanisms*, ACS Nano **8**, 5339 (2014).
- [131] A. Schwarz, A. Köhler, J. Grenz, and R. Wiesendanger, *Detecting the dipole moment of a single carbon monoxide molecule*, Appl. Phys. Lett. **105**, 011606 (2014).

- 
- [132] A. Liebig, A. Peronio, D. Meuer, A. J. Weymouth, and F. J. Giessibl, *High-precision atomic force microscopy with atomically-characterized tips*, New J. Phys. **22**, 063040 (2020).
- [133] K. Ruschmeier, A. Schirmeisen, and R. Hoffmann, *Atomic-scale force-vector fields*, Phys. Rev. Lett. **101**, 156102 (2008).
- [134] R. Hoffmann, D. Weiner, A. Schirmeisen, and A. S. Foster, *Sublattice identification in noncontact atomic force microscopy of the NaCl(001) surface*, Phys. Rev. B **80**, 115426 (2009).
- [135] K. Lämmle, T. Trevethan, A. Schwarz, M. Watkins, A. Shluger, and R. Wiesendanger, *Unambiguous determination of the adsorption geometry of a metal-organic complex on a bulk insulator*, Nano Lett. **10**, 2965 (2010).
- [136] L. Gross, B. Schuler, F. Mohn, N. Moll, N. Pavliček, W. Steurer, I. Scivetti, K. Kotsis, M. Persson, and G. Meyer, *Investigating atomic contrast in atomic force microscopy and Kelvin probe force microscopy on ionic systems using functionalized tips*, Phys. Rev. B **90**, 155455 (2014).
- [137] M. Schneiderbauer, M. Emmrich, A. J. Weymouth, and F. J. Giessibl, *CO Tip Functionalization Inverts Atomic Force Microscopy Contrast via Short-Range Electrostatic Forces*, Phys. Rev. Lett. **112**, 166102 (2014).
- [138] R. Smoluchowski, *Anisotropy of the electronic work function of metals*, Phys. Rev. **60**, 661 (1941).
- [139] A. Liebig, P. Hapala, A. J. Weymouth, and F. J. Giessibl, *Quantifying the evolution of atomic interaction of a complex surface with a functionalized atomic force microscopy tip*, Sci. Rep. **10**, 14104 (2020).
- [140] C. Barth, A. S. Foster, M. Reichling, and A. L. Shluger, *Contrast formation in atomic resolution scanning force microscopy on CaF<sub>2</sub>(111): experiment and theory*, J. Phys. Condens. Matter **13**, 2061 (2001).
- [141] A. S. Foster, C. Barth, A. L. Shluger, and M. Reichling, *Unambiguous Interpretation of Atomically Resolved Force Microscopy Images of an Insulator*, Phys. Rev. Lett. **86**, 2373 (2001).
- [142] T. Arai, S. Gritschneider, L. Tröger, and M. Reichling, *Atomic resolution force microscopy imaging on a strongly ionic surface with differently functionalized tips*, J. Vac. Sci. Technol. B **28**, 1279 (2010).

## Bibliography

---

- [143] F. J. Giessibl and M. Reichling, *Investigating atomic details of the  $\text{CaF}_2(111)$  surface with a *qPlus* sensor*, *Nanotechnology* **16**, S118 (2005).
- [144] P. W. Tasker, *The stability of ionic crystal surfaces*, *J. Phys. C Solid State Phys.* **12**, 4977 (1979).
- [145] M. Luna, F. Rieutord, N. A. Melman, Q. Dai, and M. Salmeron, *Adsorption of water on alkali halide surfaces studied by scanning polarization force microscopy*, *J. Phys. Chem. A* **102**, 6793 (1998).
- [146] J. Engelhardt, H. Dabringhaus, and K. Wandelt, *Atomic force microscopy study of the  $\text{CaF}_2(111)$  surface: from cleavage via island to evaporation topographies*, *Surf. Sci.* **448**, 187 (2000).
- [147] M. Bammerlin, R. Lüthi, E. Meyer, A. Baratoff, J. Lü, M. Guggisberg, C. Lop-pacher, C. Gerber, and H.-J. Güntherodt, *Dynamic SFM with true atomic res-olution on alkali halide surfaces*, *Appl. Phys. A* **66**, S293 (1998).
- [148] H. H. Pieper, C. Barth, and M. Reichling, *Characterization of atomic step struc-tures on  $\text{CaF}_2(111)$  by their electric potential*, *Appl. Phys. Lett.* **101**, 051601 (2012).
- [149] J. E. Lennard-Jones and B. M. Dent, *Cohesion at a crystal surface*, *Trans. Faraday Soc.* **24**, 92 (1928).
- [150] N. W. Ashcroft and N. D. Mermin, *Solid State Physics* (College ed., Brooks/-Cole Thomson Learning, 2005).
- [151] D. E. Parry, *The electrostatic potential in the surface region of an ionic crystal*, *Surf. Sci.* **49**, 433 (1975).
- [152] R. P. Feynman, R. B. Leighton, and M. Sands, *The Feynman Lectures on Physics, Volume II — Mainly Electromagnetism and Matter* (Basic Books, New York, 2010).
- [153] E. V. Kholopov, *Convergence problems of Coulomb and multipole sums in crys-tals*, *Physics-Uspekhi* **47**, 965 (2004).
- [154] H. Shi, R. I. Eglitis, and G. Borstel, *Ab initio calculations of the  $\text{CaF}_2$  electronic structure and *F* centers*, *Phys. Rev. B* **72**, 045109 (2005).

- [155] I. Horcas, R. Fernández, J. M. Gómez-Rodríguez, J. Colchero, J. Gómez-Herrero, and A. M. Baro, *WSXM: A software for scanning probe microscopy and a tool for nanotechnology*, Rev. Sci. Instrum. **78**, 013705 (2007).
- [156] R. Bennewitz, M. Reichling, and E. Matthias, *Force microscopy of cleaved and electron-irradiated  $\text{CaF}_2(111)$  surfaces in ultra-high vacuum*, Surf. Sci. **387**, 69 (1997).
- [157] D. Nečas and P. Klapetek, *Gwyddion: an open-source software for SPM data analysis*, Cent. Eur. J. Phys. **10**, 181 (2012).
- [158] M. A. Van Hove, W. Moritz, H. Over, P. J. Rous, A. Wander, A. Barbieri, N. Materer, U. Starke, and G. A. Somorjai, *Automated determination of complex surface structures by LEED*, Surf. Sci. Rep. **19**, 191 (1993).
- [159] R. Hoffmann, L. N. Kantorovich, A. Baratoff, H. J. Hug, and H.-J. Güntherodt, *Sublattice identification in scanning force microscopy on alkali halide surfaces*, Phys. Rev. Lett. **92**, 146103 (2004).
- [160] U. Dürig, H. R. Steinauer, and N. Blanc, *Dynamic force microscopy by means of the phase-controlled oscillator method*, J. Appl. Phys. **82**, 3641 (1997).
- [161] K. Kobayashi, H. Yamada, and K. Matsushige, *Frequency noise in frequency modulation atomic force microscopy*, Rev. Sci. Instrum. **80**, 043708 (2009).
- [162] J. K. Nagle, *Atomic Polarizability and Electronegativity*, J. Am. Chem. Soc. **112**, 4741 (1990).
- [163] S. Hunklinger, *Festkörperphysik* (Oldenbourg Wissenschaftsverlag GmbH, München, 2014).
- [164] Y. Cheng, C. E. Hu, Z. Y. Zeng, M. Gong, and Q. Q. Gou, *Phonon dispersion and thermodynamics properties of  $\text{CaF}_2$  via shell model molecular dynamics simulations*, Commun. Theor. Phys. **51**, 904 (2009).
- [165] D. G. de Oteyza, P. Gorman, Y.-C. Chen, S. Wickenburg, A. Riss, D. J. Mowbray, G. Etkin, Z. Pedramrazi, H.-Z. Tsai, A. Rubio, M. F. Crommie, and F. R. Fischer, *Direct Imaging of Covalent Bond Structure in Single-Molecule Chemical Reactions*, Science **340**, 1434 (2013).
- [166] S. K. Hämäläinen, N. van der Heijden, J. van der Lit, S. den Hartog, P. Liljeroth, and I. Swart, *Intermolecular contrast in atomic force microscopy images without intermolecular bonds*, Phys. Rev. Lett. **113**, 186102 (2014).

- [167] J. Peng, J. Guo, P. Hapala, D. Cao, R. Ma, B. Cheng, L. Xu, M. Ondráček, P. Jelínek, E. Wang, and Y. Jiang, *Weakly perturbative imaging of interfacial water with submolecular resolution by atomic force microscopy*, Nat. Commun. **9**, 122 (2018).
- [168] M. Neu, N. Moll, L. Gross, G. Meyer, F. J. Giessibl, and J. Repp, *Image correction for atomic force microscopy images with functionalized tips*, Phys. Rev. B **89**, 205407 (2014).
- [169] A. Liebzig and F. J. Giessibl, *In-situ characterization of O-terminated Cu tips for high-resolution atomic force microscopy*, Appl. Phys. Lett. **114**, 143103 (2019).
- [170] J. G. Hartnett, A. C. Fowler, M. E. Tobar, and J. Krupka, *The microwave characterization of single crystal lithium and calcium fluoride at cryogenic temperatures*, IEEE Trans. Ultrason. Ferroelectr. Freq. Control **51**, 380 (2004).
- [171] C. Wen and M. Lanza, *Calcium fluoride as high-k dielectric for 2D electronics*, Appl. Phys. Rev. **8**, 021307 (2021).
- [172] J. van der Lit, F. Di Cicco, P. Hapala, P. Jelinek, and I. Swart, *Submolecular Resolution Imaging of Molecules by Atomic Force Microscopy: The Influence of the Electrostatic Force*, Phys. Rev. Lett. **116**, 096102 (2016).
- [173] A. J. Weymouth, E. Riegel, O. Gretz, and F. J. Giessibl, *Strumming a Single Chemical Bond*, Phys. Rev. Lett. **124**, 196101 (2020).
- [174] G. Kresse and J. Furthmüller, *Efficient iterative schemes for ab initio total-energy calculations using a plane-wave basis set*, Phys. Rev. B **54**, 11169 (1996).
- [175] G. Kresse and D. Joubert, *From ultrasoft pseudopotentials to the projector augmented-wave method*, Phys. Rev. B **59**, 1758 (1999).
- [176] S. S. Batsanov, *Van der Waals radii of elements*, Inorg. Mater. **37**, 871 (2001).
- [177] C. A. Gough, S. E. DeBolt, and P. A. Kollman, *Derivation of fluorine and hydrogen atom parameters using liquid simulations*, J. Comput. Chem. **13**, 963 (1992).
- [178] M. Ellner, P. Pou, and R. Pérez, *Molecular Identification, Bond Order Discrimination, and Apparent Intermolecular Features in Atomic Force Microscopy Studied with a Charge Density Based Method*, ACS Nano **13**, 786 (2019).

- [179] D. A. Case, T. E. Cheatham, T. Darden, H. Gohlke, R. Luo, K. M. Merz, A. Onufriev, C. Simmerling, B. Wang, and R. J. Woods, *The Amber biomolecular simulation programs*, J. Comput. Chem. **26**, 1668 (2005).
- [180] H. Mönig, S. Amirjalayer, A. Timmer, Z. Hu, L. Liu, O. Díaz Arado, M. Cnudde, C. A. Strassert, W. Ji, M. Rohlfing, and H. Fuchs, *Quantitative assessment of intermolecular interactions by atomic force microscopy imaging using copper oxide tips*, Nat. Nanotechnol. **13**, 371 (2018).
- [181] O. E. Dagdeviren, *Limit of Temporal Resolution in Atomic Force Microscopy: Speed of Imaging with Atomically Engineered Tips While Preserving Picometer-Range Spatial*, Phys. Rev. Appl. **11**, 024068 (2019).
- [182] D. Yesilpinar, B. Schulze Lammers, A. Timmer, S. Amirjalayer, H. Fuchs, and H. Mönig, *High Resolution Noncontact Atomic Force Microscopy Imaging with Oxygen-Terminated Copper Tips at 78 K*, Nanoscale **12**, 2961 (2020).
- [183] J. Bamidele, Y. Kinoshita, R. Turanský, S. H. Lee, Y. Naitoh, Y. J. Li, Y. Sugawara, I. Štich, and L. Kantorovich, *Chemical tip fingerprinting in scanning probe microscopy of an oxidized Cu(110) surface*, Phys. Rev. B **86**, 155422 (2012).
- [184] M. Z. Baykara, M. Todorović, H. Mönig, T. C. Schwendemann, Ö. Ünverdi, L. Rodrigo, E. I. Altman, R. Pérez, and U. D. Schwarz, *Atom-specific forces and defect identification on surface-oxidized Cu(100) with combined 3D-AFM and STM measurements*, Phys. Rev. B **87**, 155414 (2013).
- [185] J. Bamidele, Y. Kinoshita, R. Turanský, S. H. Lee, Y. Naitoh, Y. J. Li, Y. Sugawara, I. Štich, and L. Kantorovich, *Image formation and contrast inversion in noncontact atomic force microscopy imaging of oxidized Cu(110) surfaces*, Phys. Rev. B **90**, 035410 (2014).
- [186] H. Mönig, M. Todorović, M. Z. Baykara, T. C. Schwendemann, L. Rodrigo, E. I. Altman, R. Pérez, and U. D. Schwarz, *Understanding Scanning Tunneling Microscopy Contrast Mechanisms on Metal Oxides: A Case Study*, ACS Nano **7**, 10233 (2013).
- [187] D. J. Coulman, J. Wintterlin, R. J. Behm, and G. Ertl, *Novel Mechanism for the Formation of Chemisorption Phases: The (2x1)O-Cu(110) "Added-Row" Reconstruction*, Phys. Rev. Lett. **64**, 1761 (1990).

## Bibliography

---

- [188] K. Kern, H. Niehus, A. Schatz, P. Zeppenfeld, J. Goerge, and G. Comsa, *Long-Range Spatial Self-Organization in the Adsorbate-Induced Restructuring of Surfaces: Cu{110}-(2 x 1)O*, Phys. Rev. Lett. **67**, 855 (1991).
- [189] J. Harl and G. Kresse, *Density functional theory studies on stress stabilization of the Cu(110) striped phase*, Surf. Sci. **600**, 4633 (2006).
- [190] S. Kishimoto, M. Kageshima, Y. Naitoh, Y. J. Li, and Y. Sugawara, *Study of oxidized Cu(110) surface using noncontact atomic force microscopy*, Surf. Sci. **602**, 2175 (2008).
- [191] P. Hofmann, K. Schindler, S. Bao, V. Fritzsche, A. M. Bradshaw, and D. Woodruff, *A photoelectron diffraction study of the structure of the Cu {110}(2 x 1)-CO system*, Surf. Sci. **337**, 169 (1995).
- [192] Y. Sugimoto, P. Pou, M. Abe, P. Jelinek, R. Pérez, S. Morita, and Ó. Custance, *Chemical identification of individual surface atoms by atomic force microscopy*, Nature **446**, 64 (2007).
- [193] N. M. Schaeublin, L. K. Braydich-Stolle, A. M. Schrand, J. M. Miller, J. Hutchison, J. J. Schlager, and S. M. Hussain, *Surface charge of gold nanoparticles mediates mechanism of toxicity*, Nanoscale **3**, 410 (2011).
- [194] N. Pardi, M. J. Hogan, F. W. Porter, and D. Weissman, *mRNA vaccines—a new era in vaccinology*, Nat. Rev. Drug Discov. **17**, 261 (2018).
- [195] L. J. Klein and C. C. Williams, *Single electron tunneling detected by electrostatic force*, Appl. Phys. Lett. **79**, 1828 (2001).
- [196] M. T. Woodside and P.L. McEuen, *Scanned probe imaging of single-electron charge states in nanotube quantum dots*, Science **296**, 1098 (2002).
- [197] R. Stomp, Y. Miyahara, S. Schaer, Q. Sun, H. Guo, P. Grutter, S. Studenikin, P. Poole, and A. Sachrajda, *Detection of single-electron charging in an individual InAs quantum dot by noncontact atomic-force microscopy*, Phys. Rev. Lett. **94**, 056802 (2005).
- [198] E. Bussmann and C. C. Williams, *Single-electron tunneling force spectroscopy of an individual electronic state in a nonconducting surface*, Appl. Phys. Lett. **88**, 263108 (2006).

- 
- [199] L. Gross, F. Mohn, P. Liljeroth, J. Repp, F. J. Giessibl, and G. Meyer, *Measuring the Charge State of an Adatom with Noncontact Atomic Force Microscopy*, *Science* **324**, 1428 (2009).
- [200] W. Steurer, J. Repp, L. Gross, I. Scivetti, M. Persson, and G. Meyer, *Manipulation of the charge state of single Au atoms on insulating multilayer films*, *Phys. Rev. Lett.* **114**, 036801 (2015).
- [201] P. Rahe, R. P. Steele, and C. C. Williams, *Consecutive Charging of a Molecule-on-Insulator Ensemble Using Single Electron Tunnelling Methods*, *Nano Lett.* **16**, 911 (2016).
- [202] W. Steurer, S. Fatayer, L. Gross, and G. Meyer, *Probe-based measurement of lateral single-electron transfer between individual molecules*, *Nat. Commun.* **6**, 8353 (2015).
- [203] S. Fatayer, B. Schuler, W. Steurer, I. Scivetti, J. Repp, L. Gross, M. Persson, and G. Meyer, *Reorganization energy upon charging a single molecule on an insulator measured by atomic force microscopy*, *Nat. Nanotechnol.* **13**, 376 (2018).
- [204] L. L. Patera, F. Queck, P. Scheuerer, and J. Repp, *Mapping orbital changes upon electron transfer with tunnelling microscopy on insulators*, *Nature* **566**, 245 (2019).
- [205] L. L. Patera, F. Queck, P. Scheuerer, N. Moll, and J. Repp, *Accessing a Charged Intermediate State Involved in the Excitation of Single Molecules*, *Phys. Rev. Lett.* **123**, 016001 (2019).
- [206] S. Fatayer, F. Albrecht, Y. Zhang, D. Urbonas, D. Peña, N. Moll, and L. Gross, *Molecular structure elucidation with charge-state control*, *Science* **365**, 142 (2019).
- [207] J. Schütte, R. Bechstein, M. Rohlfing, M. Reichling, and A. Kühnle, *Cooperative mechanism for anchoring highly polar molecules at an ionic surface*, *Phys. Rev. B* **80**, 205421 (2009).
- [208] Y. Y. Illarionov, A. G. Banskchikov, D. K. Polyushkin, S. Wachter, T. Knobloch, M. Thesberg, L. Mennel, M. Paur, M. Stöger-Pollach, A. Steiger-Thirsfeld, M. I. Vexler, M. Walzl, N. S. Sokolov, T. Mueller, and T. Grasser, *Ultrathin calcium fluoride insulators for two-dimensional field-effect transistors*, *Nat. Electron.* **2**, 230 (2019).

## Bibliography

---

- [209] L. Laflör, F. A. Schlage, L. Kantorovich, P. J. Moriarty, M. Reichling, and P. Rahe, *Quadruped Molecular Anchoring to an Insulator: Functionalized Ferrocene on  $\text{CaF}_2$  Bulk and Thin Film Surfaces*, J. Phys. Chem. C **124**, 9900 (2020).

# Acknowledgments

At this point I would like to express my thanks to everyone who helped in course of the creation of this work.

At first, I want to thank my supervisor Prof. Dr. Franz J. Gießibl for giving me the opportunity to work in his group and to start a PhD project. Moreover, I want to thank him for his ever present encouragement, creativity and determination, which I really admire and consider to be a key for all the fascinating fundamental research done in his group. I also want to explicitly mention our awesome skiing days at the conferences in Schladming and Obertraun. Furthermore, I want to thank him for the final proof-reading of this thesis.

I would like to thank Prof. Dr. Dominique Bougeard for the second assessment of this thesis and his collaboration in our current research project on topological insulators, which is not covered in this thesis.

Special thanks go to my former long-term office mates Dr. Angelo Peronio and Daniel Meuer for working with me already since my Bachelor and Master thesis projects. From both, I inherited significant scientific knowledge and learned how to operate the *LT 1* microscope. I very much appreciate also our private activities, especially playing music together with Dani as “The Isotopes” which resulted in many fun moments over the last years!

Furthermore, I want to thank Dr. Jay Weymouth for invaluable support during all these years with almost any problems that occurred in the lab, scientific writing or programming. I also want to thank him for the non-scientific conversations and personal advice, our Schafkopf games in the city and for proof-reading of this thesis.

Special gratitude goes to our international collaborators and visiting scientists. I want to explicitly acknowledge the work of Dr. Prokop Hapala, who conducted the probe particle model simulations for the CO tip on CaF<sub>2</sub>(111). These calculations

## A Acknowledgments

---

added a lot of value to our interpretations and the project. Moreover, I want to thank Prof. Dr. Norio Okabayashi for his numerous research stays here in Germany and working together with me on the *LT 1* and all our nice conversations. I admire his working attitude and endurance, which was very inspiring also for my own work.

Special thanks go to Dr. Ferdinand Huber, Dr. Julian Berwanger, Korbinian Pürckhauer, Dominik Kirpal, Oliver Gretz and the “next generation”, Adrian Weindl, Fabian Stilp, Marco Weiss and Chris Setescak for their ever present support, the valuable scientific and non-scientific discussions and all the fun moments we had at conferences, excursions and outside work so far, like our board game evenings. Furthermore, I want to thank Korbinian for proof-reading the first version of this thesis.

Additionally, I want to thank all other permanent and temporal colleagues in the group of Prof. Gießibl, especially the undergraduate students I supervised, for the pleasant atmosphere and working environment and their ever present curiosity to learn and explore new things in the labs. I want to explicitly thank Petra Wild, Anja Merkel and Florian Griesbeck for their immense administrative and technical support.

Finally, I also want to thank all my friends for their encouragement and all the good times they make possible. Furthermore, I am incredibly grateful to my whole family for their invaluable support during my education and especially my studies over the last ten years. Without you, this would not have been possible. At last, I want to thank my girlfriend Vroni for her ever present support, her great understanding in sometimes a little difficult moments and the beautiful time we have together.

